

**MECHANICAL AND STRUCTURAL EFFECTS OF HIV-1 PROTEINS  
AND HIGHLY ACTIVE ANTIRETROVIRAL THERAPY (HAART)  
DRUGS ON MURINE ARTERIES**

A Dissertation  
Presented to  
The Academic Faculty

by

Laura Hansen

In Partial Fulfillment  
of the Requirements for the Degree  
Doctor of Philosophy in Bioengineering

Georgia Institute of Technology

December 2012

**MECHANICAL AND STRUCTURAL EFFECTS OF HIV-1 PROTEINS  
AND HIGHLY ACTIVE ANTIRETROVIRAL THERAPY (HAART)  
DRUGS ON MURINE ARTERIES**

Approved by:

Dr. Rudolph L. Gleason, Jr., Advisor  
School of Mechanical Engineering  
School of Biomedical Engineering  
*Georgia Institute of Technology*

Dr. W. Robert Taylor  
School of Medicine  
*Emory University*

Dr. Robert Guldberg  
School of Mechanical Engineering  
*Georgia Institute of Technology*

Dr. Roy Sutliff  
School of Medicine  
*Emory University*

Dr. Manu Platt  
School of Biomedical Engineering  
*Georgia Institute of Technology*

Date Approved: 7/18/2012

## ACKNOWLEDGEMENTS

My research the past five years and this dissertation would not have been possible without the help and support of many people along the way. This project was truly a collaborative effort and I'd like to thank my committee because this work would not have been possible without each of them. First, I need to thank Dr. Bob Guldberg whose animal studies class my first year taught me many of the animal techniques used in the study as well as guided me through my first of many IACUC protocols to come. Throughout this work he also provided a source of knowledge and advice on the mechanical aspects. Dr. Taylor also played an integral role in the project providing insight into much of the mouse work and physiology and training students and post docs that provided advice and help along the way.

I owe a big thank you to Dr. Manu Platt and Dr. Roy Sutliff who both played huge roles in my work and have co-authored several abstracts and papers with me. It was Dr. Platt who first approached Rudy with idea to investigate HIV and cardiovascular disease, and luckily I was between projects and looking for ideas. I might not have found such an interesting and unique topic without Dr. Platt's request for help. He also opened up his lab to me to carry out all my "biology" work. Dr. Sutliff served as the experienced HIV researcher in our new endeavors and provided valuable guidance to me in an area I knew nothing about. Of course it goes without saying that without his lab providing all the HIV Tg mice in Aim 2, this work would not have been possible.

I also need to thank my advisor Dr. Rudy Gleason for all his instruction and guidance these past 5 years. I actually did not meet with Rudy on my visit to Tech, but I recognized his name on his office door and e-mailed him after the trip. Even from the first e-mail he was open, friendly, and eager for me to join the lab. The lab provided the perfect place for me to use my

interests and skills, and he was also supportive in my new ideas and attempts in studying more biology. Rudy has also provided a great example of someone who is able to successfully balance work and family. His Ethiopian adventure this year has left us working rather independently, but he taught us well and I feel confident in my ability to conduct my own research in the future.

My graduate school experience would also not be the same without my lab. They have provided assistance, suggestions, and helped me troubleshoot more times than I can count. Of course we also find time to relax and have fun between working- for example lab lunches where “the whole lab is going.” Specifically, I have to thank William for being the senior guy in lab, helping me get started, and teaching me all about my mouse work- surgeries, mechanical tests and imaging. Roy also has always been there as the go-to guy for help and advice. Julia and Alex deserve my thanks as part of the “HIV group” as we started a new area of research. Alex also deserves extra thanks for all of his help taking care of the mice with daily gavage. I need to also thank the other lab members past and present: Seth, Mike, Kelly, Daniel, Prem, and Yasaman.

Numerous other people from Tech, Emory, and VA have also made my work possible. Jing Ma in Dr. Sutliff’s lab has my extreme gratitude for raising all the HIV Tg mice for me and bringing them upstairs for me whenever I needed them. Dr. Platt’s lab welcomed me into their lab and answered all my questions; specifically, I need to thank Jerald and Ivana for teaching me how to do zymos. Ivana was also my partner in crime as we ventured to the VA to harvest tissues. I also owe a huge thanks to Monet Roberts, an undergraduate in the Platt lab, for all her help in running zymos for me this past spring and summer and helping me finish in time. Others that deserve thanks are Katie Maiellaro-Rafferty, for her help with excising aortas, Alicia Lyle and Chanwoo Kim for PCR advice, and Casey Holliday-Ankeny for all her help trouble shooting

PCR. Also thanks to the IBB core histology and microscopy managers Aqua Asberry and Andrew Shaw. Finally, I owe thanks to Dr. Laura O'Farrell, Kim Benjamin, and the entire PRL staff for helping take care of my mice.

Besides all those people who have provided technical help and advice, I also need to thank all my friends. I've had such a great support group of people both here in Atlanta and far away. These people have listened to me vent, cheered me on, helped me relax, made me laugh, kept me sane, and helped make the past few years a great experience. My friends are too numerous to count though my boyfriend Seth deserves special credit for supporting me these past two years in which I did the majority of this work. And last but certainly not least, I need to thank my family. Michelle and Neil, my little sister and brother, have not only always put up with all of my overachieving ways, but they've always been my fans and cheered me on even coming to my defense. My parents, John and Linda, are amazing. They always encouraged me (and all their children) as we have run off around the country pursuing our dreams. They've always believed in me even when I was discouraged and doubted and could always be counted on for some good advice and a sympathetic ear. Despite living so far away from them, I feel like they have been there every step of the way.

# TABLE OF CONTENTS

	Page
ACKNOWLEDGEMENTS	iii
LIST OF TABLES	xi
LIST OF FIGURES	xii
LIST OF ABBREVIATIONS	xiv
SUMMARY	xvii
CHAPTER 1: SPECIFIC AIMS	1
1.1 Introduction	1
1.2 Specific Aim 1	2
1.3 Specific Aim 2	3
1.4 Specific Aim 3	3
CHAPTER 2: BACKGROUND AND LITERATURE REVIEW	5
2.1 Arteries	5
2.2 Cardiovascular Disease and Atherosclerosis	6
2.3 Pathology of HIV-1	10
2.4 Antiretroviral Therapy	12
2.5 Non-AIDS Related Complications	14
2.6 HIV and Cardiovascular Disease	16
2.7 HAART and Cardiovascular Disease	19
2.8 Vascular Mechanics	22
2.9 Constitutive Models of Blood Vessels	23

CHAPTER 3: SPECIFIC AIM 1: DEVELOP A MICROSTRUCTURALLY	
BASED CONSTITUTIVE MODEL OF ARTERIES	27
3.1 Introduction	27
3.2 Methods	28
3.2.1 Theoretical Framework	28
3.2.2 Phenomenological Models	31
3.2.3 Microstructurally-motivated models: a discrete set of fibers	33
3.2.4 Microstructurally-motivated models: distributions of fibers	37
3.2.5 Parameter Estimation	41
3.2.6 Penalty Set	42
3.2.7 Statistical Analysis	43
3.3 Results	43
3.3.1 Chuong and Fung Model	43
3.3.2 Four Fiber-Family Model	46
3.3.3 Microstructurally-Motivated Models: A Discrete Set of Fibers	49
3.3.4 Rule of Mixtures Model: Distributed Fibers	55
3.4 Discussion	55
CHAPTER 4: SPECIFIC AIM 2: CHARACTERIZE THE MECHANICAL BEHAVIOR,	
MICROSTRUCTURE, PROTEASE ACTIVITY, AND ECM GENE EXPRESSION OF	
ARTERIES FROM AN HIV-1 TRANSGENIC MOUSE MODEL	60
4.1 Introduction	60
4.2 Methods	61
4.2.1 HIV-Transgenic Mouse Model	61

4.2.2 Common Carotid Artery and Aorta Preparation	62
4.2.3 Biomechanical Measurements: Cylindrical Biaxial Testing, Arterial Stiffness, and Opening Angle	62
4.2.4 Intima-Media Thickness Measurements	64
4.2.5 Other Microstructure Analysis	65
4.2.6 Collagen and Elastin Content Measurements	66
4.2.7 Cathepsin Expression and Activity Measurements	67
4.2.8 Statistical Analysis	68
4.2 Results	68
4.2.1 Mice expressing HIV proteins exhibit increased arterial stiffness and altered biomechanics	68
4.2.2 Mice expressing HIV proteins have increased carotid intima-media thickness	71
4.2.3 Collagen Fiber Angles are similar between groups	73
4.2.4 Elastin breaks	73
4.2.5 Aorta from mice expressing HIV proteins have lower elastin content	75
4.2.6 Aorta from mice over-expressing HIV proteins exhibit increased cathepsin K and S activity	75
4.4 Discussion	78
CHAPTER 5: SPECIFIC AIM 3: CHARACTERIZE THE MECHANICAL BEHAVIOR, MICROSTRUCTURE, PROTEASE ACTIVITY, AND ECM GENE EXPRESSION OF ARTERIES FROM WILD TYPE MICE GIVEN THE ANTIRETROVIRAL MEDICATION AZT	83

5.1 Introduction	83
5.2 Methods	85
5.2.1 Animal Model	85
5.2.2 Blood Pressure Measurements	85
5.2.3 Common Carotid Artery and Aorta Preparation	86
5.2.4 Lipid Studies	86
5.2.5 Biomechanical Measurements: Cylindrical Biaxial Testing, Arterial Stiffness, and Opening Angle	87
5.2.6 Intima-Media Thickness Measurements	88
5.2.7 Other Microstructure Analysis	88
5.2.8 Collagen and Elastin Content Measurements	89
5.2.9 Cathepsin Expression and Activity Measurements	89
5.2.11 Statistical Analysis	89
5.3 Results	90
5.3.1 Mice treated with AZT do not have increased blood pressure	90
5.3.2 Lipid profiles did not differ between treatment groups	90
5.3.3 Mice treated with AZT exhibit increased arterial stiffness and altered biomechanics	90
5.3.4 Mice treated with AZT have increased carotid intima-media thickness	95
5.3.5 Collagen fiber distributions are similar between groups	96
5.3.6 Elastin Breaks	98
5.3.7 Carotids from AZT treated mice have lower elastin content	98

5.2.8 Arteries from mice treated with AZT have differences in cathepsin activity	98
5.4 Discussion	101
CHAPTER 6: SUMMARY, LIMITATIONS, AND FUTURE CONSIDERATIONS	106
6.1 Summary	106
6.2 Limitations	109
6.3 Future Considerations	114
APPENDIX A: CHAPTER 4 ADDITIONAL FIGURES	119
APPENDIX B: CHAPTER 5 ADDITIONAL FIGURES	124
REFERENCES	125

## LIST OF TABLES

	Page
Table 3.1: Material parameters for the model of Chuong and Fung	45
Table 3.2: Material parameters for the model of the four-fiber family model	48
Table 3.3: Material parameters representative data for the various versions of the rule-of-mixtures constitutive model	51

## LIST OF FIGURES

	Page
Figure 3.1: The Chuong and Fung phenomenological model fits the data well	44
Figure 3.2: The Four Fiber-Family Model has a better fit than the Chuong and Fung Model	47
Figure 3.3: The rule-of-mixtures model captures the individual components' physiological contributions of the total stress	52
Figure 3.4: Requiring collagen fibers to have the same material properties in all orientations decreases the goodness of fit	54
Figure 4.1: HIV-1 protein expression increases arterial stiffness	69
Figure 4.2: HIV-1 protein expression results in increased opening angle and circumferential residual stress	70
Figure 4.3: Confocal images can be used to quantify thickness and collagen fiber distribution	72
Figure 4.4: HIV-1 protein expression increases intima-media thickness	72
Figure 4.5: Collagen fiber angles no major differences	74
Figure 4.6: HIV-1 protein expression decreases elastin content	76
Figure 4.7: Carotids from mice HIV Tg mice have increased cathepsin S and decreased cathepsin V activity	77
Figure 5.1: Blood pressure does not differ between groups	91
Figure 5.2: AZT treatment did not alter lipid profiles	91
Figure 5.3: AZT treatment increases arterial stiffness	93
Figure 5.4: AZT treatment decreases axial force during pressure-diameter tests	94
Figure 5.5: AZT treatment did not result in opening angle differences	95
Figure 5.6: AZT treatment increased intima-media thickness	96
Figure 5.7: Collagen fiber angles no significant differences	97
Figure 5.8: AZT treatment decreases elastin content	99

Figure 5.9: Arteries from mice treated with AZT have increased cathepsin L and decreased cathepsin V activity	100
Figure A.1 HIV-1 protein expression increases arterial stiffness in carotids at a subphysiological stretch	119
Figure A.2: HIV-1 protein expression increases modulus (stiffness) in carotids at subphysiological and superphysiological stretches	120
Figure A.3: HIV-1 protein expression increases modulus (stiffness) in aortas at subphysiological and superphysiological stretches	121
Figure A.4: Axial behavior at physiologically relevant load is not different between carotids from HIV Tg and wildtype mice.	122
Figure A.4: Aortas from mice HIV Tg mice have increased cathepsin S and K and decreased cathepsin V activity	123
Figure B.1: AZT treatment increases arterial stiffness in aortas at a subphysiological stretch.	124
Figure B.2: AZT treatment increases arterial stiffness in aortas at a subphysiological stretch.	124

## LIST OF ABBREVIATIONS

ADHP	10-acetyl-3,7—dihydroxyphenoxazine
AHA	American Heart Association
AIDS	Acquired Immune Deficiency Syndrome
ANOVA	Analysis of Variance
ART	Antiretroviral therapy
AZT	Azidothymidine
CAC	Coronary artery calcification
CVD	Cardiovascular disease
CT	Computed tomography
DMEM	Dulbecco's modified Eagles medium
ECM	Extracellular matrix
ELISA	Enzyme-linked immunosorbent assay
eNOS	Endothelial nitric oxide synthase
ET-1	Endothelin-1
FMD	Flow mediated dilation
HAART	Highly active antiretroviral therapy
HDL	High-density lipoprotein
H&E	Hematoxylin and eosin
HIV	Human immunodeficiency virus
ICAM-1	Intercellular cell adhesion molecule 1
IFN $\gamma$	Interferon gamma
IL-1	Interleukin-1

IMT	Carotid intima-media thickness
IRD	Immune restoration disease
IRIS	Immune reconstitution inflammatory syndrome
JCV	John Cunningham virus
KCL	Potassium chloride
LDL	Low-density lipoprotein
MCP-1	Monocyte chemotactic protein1
M-CSF	Macrophage colony stimulating factor
mmHg	Millimeters of mercury
mN	Millinewtons
NNRTI	Non-nucleoside reverse transcriptase inhibitor
NO	Nitric oxide
NOS	Nitric oxide synthase
NRTI	Nucleoside reverse transcriptase inhibitor
PBS	Phosphate buffered saline
PE	Phenylephrine
PI	Protease inhibitor
PDGF	Platelet derived growth factor
ROS	Reactive oxygen species
RT-PCR	Reverse transcription polymerase chain reaction
SEM	Standard error of the mean
SMCs	Smooth Muscle Cells
SNP	Sodium nitroprusside

TB	Tuberculosis
TGF- $\beta$	Transforming growth factor-beta
TNF- $\alpha$	Tumor necrosis factor-alpha
VCAM-1	Vascular cell adhesion molecule 1
vWF	von Willebrand factor

## SUMMARY

The overall goals of this project were to develop microstructurally based constitutive models to characterize the mechanical behavior of arteries and to investigate the effects of HIV proteins and antiretroviral drugs on the microstructure and mechanical behavior. To this end we created several constitutive models in aim 1 using a rule of mixtures approach, investigated the role of viral proteins in aim 2 through the use a transgenic mouse model, and studied the effects of the antiretroviral drug AZT administered to mice in aim 3.

It is well known that the local mechanical environment which cells experience mediates growth and remodeling and that subsequent growth and remodeling can change that mechanical environment. This remodeling includes changes in the content and organization of the constituents of arteries (collagen, elastin, and smooth muscle cells). The first aim thus created models that incorporated the content and organization of these constituents using a rule-of-mixtures approach. The models we developed were able to capture the mechanical behavior of the arteries as well as previously developed phenomenological models while providing more physical meaning to the parameters, some which can be measured experimentally for incorporation into future models.

Aims 2 and 3 investigated the mechanical and microstructural changes to murine arteries in response to HIV proteins or the drug AZT. While the development of antiretroviral therapy has greatly increased the life expectancy of patients with HIV, a number of other complications and co-morbidities including cardiovascular disease have become apparent. While clinical data has implicated both the virus and the antiretroviral drugs as playing roles, this work addressed the need of investigating these effects in a controlled manner. Specifically we used mouse

models and focused on the two subclinical markers of increased intima-media thickness and arterial stiffening.

Aim 2 used a transgenic mouse that expressed most of the human HIV proteins. We observed both intima-media thickening and arterial stiffening in alignment with clinical data. Other changes that also support a proatherogenic phenotype included decreased elastin content and changes in cathepsin activity. Aim 3 administered the antiretroviral drug AZT to healthy mice and we also observed the same subclinical markers of atherosclerosis including intima-media thickening and arterial stiffening as well as the other proatherogenic changes of decreased elastin and changes in cathepsin activity. Several other parameters including axial behavior, opening angles, collagen content, and collagen fiber angles were also quantified. These were important to fully characterize the vessel and may also be incorporated in the future into the constitutive models developed in aim1.

In conclusion, in aim 1 we developed a microstructurally based constitutive model of arteries that effectively captures the mechanical behavior and includes parameters that have more physical meaning and some of which are experimentally tractable. Aims 2 and 3 both observed several subclinical markers of atherosclerosis in mice that express HIV proteins or were given AZT, providing a good model for future work and suggesting that both the HIV virus and antiretroviral drugs may play roles in the development of atherosclerosis in HIV.

# CHAPTER 1

## SPECIFIC AIMS

### 1.1 Introduction

Acquired immunodeficiency syndrome (AIDS) is considered a global epidemic with human immunodeficiency virus-1 (HIV-1), the causative agent of AIDS, having a worldwide prevalence of over 34 million people (1). Due to the success of highly active antiretroviral therapy (HAART), HIV-1-infection has been transformed from a terminal diagnosis to a manageable chronic disease. HIV patients, however, have an elevated incidence of dyslipidemia, lipodystrophy, insulin resistance, diabetes mellitus, and cardiovascular disease (CVD); the latter includes an elevated risk of myocardial infarction (2-4) and higher prevalence of atherosclerotic lesions (5-7), as well as increases in markers of subclinical atherosclerosis including increased carotid artery intima-media thickness (8-13), increased arterial stiffness (8, 14, 15) and impaired flow-mediated brachial artery dilation, an indicator of endothelial dysfunction (8, 9, 14, 16-20).

Despite the numerous clinical studies, the roles and importance of the HIV-1 virus and the HAART drugs in causing these changes still remains unclear. Discrepancies exist between various studies due to the inability to control other cardiovascular risk factors such as age, gender, weight, cholesterol levels, smoking, and hypertension in all patients as well any confounding effects from different stages of HAART therapy. This study seeks to further investigate the independent roles of the HIV-1 virus and the HAART drug AZT in the development of cardiovascular disease, with emphasis on the development of geometric and biomechanical markers of atherosclerosis.

Towards this end, in Aim 1 we developed and tested a novel microstructurally-based constitutive model, capable of integrating tissue-level and microstructure biomechanical measurements. Specifically, this model can incorporate the relative content and organization of elastin, collagen, and smooth muscle cells comprising the vessel wall and provides a framework to integrate tissue level mechanical changes (e.g., arterial stiffening) with microstructural level changes (e.g., elastin fragmentation) (21-23). In aims 2 and 3 we quantified these biomechanical and microstructure measurements, in parallel with molecular markers of vascular remodeling, in common carotid arteries and aortas in an HIV-1 transgenic mouse model and mice administered the HAART drug AZT.

## **1.2 Specific Aim 1**

### **Develop a microstructurally based constitutive model of arteries.**

Mechanically mediated vascular remodeling occurs as vascular cells sense and respond to their local mechanical environment. Thus, fundamental to many studies of vascular remodeling is the quantification of the local mechanical environment under specific loading conditions; i.e., determining the distribution of stresses and strains of a vessel under applied loads (e.g., pressure, axial extension, luminal flow, etc.) Knowledge of the constitutive behavior of the vessel wall allows one to predict the local stresses and strains throughout the wall for a vessel of known geometry and applied loads. Given that the material response of biological tissues is governed by their internal structure (i.e., cell and extracellular matrix content and organization), the goal of this aim is to create a model that prescribes mechanical behavior based on those constituents such that changes

in various components determined experimentally as in the previous two aims can be incorporated into the model in the future.

### **1.3 Specific Aim 2**

**Characterize the mechanical behavior, microstructure, and protease activity of arteries from a HIV-1 transgenic mouse model.**

Clinical studies have shown that HIV-1 patients show early signs of atherosclerosis such as arterial stiffening and carotid intima-media thickening. However, the role of viral proteins and HAART drugs in these symptoms remains unclear. Therefore, the goal of this aim was to isolate the effects of the viral proteins on the arterial behavior through the use of a HIV-1 transgenic mouse model (HIV-1 Tg). These mice express all of the HIV-1 genes except for *gag* and *pol* and therefore the blood has circulating proteins that can interact and affect the arteries as in HIV patients. We hypothesized that common carotid arteries and aortas from HIV-1 Tg mice would exhibit increased arterial stiffness and intima-media thickness compared to their littermate controls and that these differences would correlate with differences in collagen and elastin content and organization, and cathepsin L, S, and V activity.

### **1.4 Specific Aim 3**

**Characterize the mechanical behavior, microstructure, and protease activity of arteries from wild type mice given the antiretroviral medication AZT.**

The various HAART drugs are also known to have negative effects on endothelial and vascular cells that could contribute to the increased cardiovascular disease in HIV patients. However, more *in vivo* data related to HAART's effects on the arterial wall is still needed. Therefore, the goal of this aim was to isolate the effects of HAART on the

arterial behavior through the administration of the nucleoside reverse transcriptase inhibitor (NRTI) drug azidothymidine (AZT) via oral gavage to otherwise healthy FVB/N mice. We hypothesized that the common carotid arteries and aortas from AZT treated mice would exhibit increased arterial stiffness and intima-media thickness compared to sham-fed controls and that these differences would correlate with differences in collagen and elastin content and organization and cathepsin L, S, and V activity.

## CHAPTER 2

### Background and Literature Review

#### 2.1 Arteries

Arteries and veins are the two major types of blood vessels within the cardiovascular system. Veins serve to return circulating blood to the heart while arteries are the conduits that carry blood away from the heart to the rest of the body to deliver oxygen and nutrients to the tissues. The arterial wall is a multilayered structure with the ability to sense and respond to changes in both blood pressure and flow in short time frames (dilation or constriction) or long term (growth and remodeling). The three layers that comprise the blood vessels are the intima, media, and adventia. (24, 25) The intima is the inmost layer and is primarily a single layer of endothelial cells on a basement membrane that line the lumen. The health and integrity of the cell layer is important as they provide a non-thrombogenic surface for blood flow as well as sense changes in flow or pressure and release signaling molecules such as nitric oxide (NO) and endothelin-1 (ET-1) to the outer layers of the vessel. The middle layer is the media, which is comprised of concentric layers of smooth muscle cells (SMCs) and elastin, which form elastic lamellae. These smooth muscle cells provide the ability of the artery to contract and dilate. The outermost layer of arteries is the adventia, which is comprised primarily of collagen and fibroblasts and some larger vessels (aorta) also has a vasa vasorum, which are a small blood vessel network to nourish the vessel wall itself. When healthy, arteries are able to supply proper blood flow to all the body's tissue, but various perturbations in the healthy homeostatic state can lead to damage or disease that impair this ability.

## 2.2 Cardiovascular Disease and Atherosclerosis

Cardiovascular disease (CVD) is widespread in the United States with one in every three deaths in 2008 attributed to some form of CVD (26). Many of these cardiovascular events occur as a consequence of atherosclerosis in the arteries. Atherosclerosis is a condition in which fat, inflammatory cells, and scar tissue accumulate in the arterial wall (26). Atherosclerosis is considered an inflammatory disease since immune cells play a large role in its development (27). The initiation of the disease is unclear but has been linked to hemodynamics, specifically regions of oscillatory flow or low shear stress, damage and dysfunction to the endothelial layer of the arterial wall, increased cholesterol or cytokine levels in the blood, amongst other factors (27-30). Once activated by any one of these mechanisms, the endothelial cells begin to express factors such as vascular cell adhesion molecule-1 (VCAM-1) and intercellular adhesion molecule-1 (ICAM-1), that promote the binding of monocytes and T lymphocytes circulating in the blood. The adhered monocytes then migrate through the endothelial layer into the arterial wall in a process thought to be promoted the expression of factors such as monocyte chemoattractant protein 1 (MCP-1). (27, 29, 31, 32) Once in the wall, the monocytes differentiate into macrophages that express receptors such as scavenger receptor A and CD36 which allow them to internalize and accumulate lipoproteins. Macrophage colony-stimulating factor (M-CSF) and a number of signaling molecules produced by endothelial and smooth muscle cells promote this transition. (27, 32) Within the wall, the macrophages continue to internalize lipids until they become lipid laden foam cells. They also replicate as well as release cytokines including interleukin-1 (IL-1) and tumor necrosis factor (TNF- $\alpha$ ) and other factors that promote further recruitment of cells. (27,

33) Smooth muscle cells also release a number cytokines including platelet derived growth factor (PDGF), transforming growth factor-beta (TGF- $\beta$ ), and interferon gamma (IFN $\gamma$ ). (31) The accumulation of these fat laden macrophages characterizes the early stage of atherosclerotic lesions known as fatty streaks. (34) The lesions continue to grow and narrow the lumen as smooth muscle cells take on a more “synthetic” phenotype in which they have increased proliferation and production of extracellular matrix (ECM) specifically collagen. Also, in lipid rich lesions it has been shown the smooth muscle cell have increased proteoglycan production which can more easily entrap LDL (low-density lipoprotein). Smooth muscles may contribute to the formation of a lipid laden core of the lesions themselves as they have been shown to express cholesterol and LDL receptors in the presence of various cytokines. (31)

Increased levels of reactive oxygen species are also associated with atherosclerotic vessels. While healthy vessels generate reactive oxygen species (ROS), which play roles in important signaling pathways, in atherosclerotic arteries, the levels of ROS are increased and can lead to negative effects on the vessels. The endothelial dysfunction and impaired vasodilation associated with ROS are primarily due to a decrease in the availability of nitric oxide (NO). Nitric oxide production is normally highly regulated by the level of eNOS (endothelial nitric oxide synthase) production within the cells; however, the regulation pathways for eNOS are closely related to redox pathways and thus increased ROS can disturb eNOS synthesis leading to decreased NO and endothelial dysfunction. (35) Other deleterious effects of disturbances in ROS, eNOS, and NO regulation include increasing leukocyte adhesion molecules like VCAM-1. (35, 36) Increased ROS can also increase the oxidation of LDL (ox-LDL), which

macrophages uptake as they transition to foam cells. The ox-LDL can also further exacerbate the decreased NO and endothelial cell inflammatory responses. Furthermore, increased ROS and decreased NO are thought to cause increased SMC proliferation, migration, and transition to a “synthetic” phenotype. (33, 35, 36)

While extracellular proteases play many important roles in healthy vessels including remodeling and healing, deregulation of the enzymes is also associated with various vessel pathologies. Proteases are a family of enzymes that irreversibly hydrolyze peptide bonds and are most commonly known for their ability to degrade ECM. The best known group of proteases are metalloproteinases, which have an active site that contains a metal atom (usually zinc). (37) Two other groups are serine proteases and cysteine proteases which include cathepsins. Originally cathepsins were thought to act primarily intracellularly to degrade proteins in the lysosomes, but a number of cells including macrophages, smooth muscle cells, and endothelial cells can transport cathepsins out of the cells for degradation of proteins extracellularly. (37) Studies have shown that protease activity (including cathepsin activity) is increased in atherosclerotic vessels. Macrophages that have migrated into the walls are thought to be a primary source of the increased levels of protease expression, though endothelial and smooth muscle cells also contribute. Histology of plaques has shown enlarged lysosomes in both macrophages and smooth muscle cells. (37, 38) Specifically, cathepsins S and K were found in the fibrous cap, foam cells, and adjacent to SMCs in atherosclerotic vessels, while healthy vessels had negligible cathepsins as detected by immunohistochemistry and Western and Northern blots. Extracts from the atherosclerotic tissue have shown that the cathepsins also have potent elastolytic activity. (38, 39) Stimulation of cultured smooth muscle cells

with interferon gamma (IFN $\gamma$ ), interleukin-1 beta (IL-1 $\beta$ ), or tumor necrosis factor- $\alpha$  (TNF- $\alpha$ ), cytokines released by cells during plaque formation, induced cathepsin S production and degradation of elastin. (38, 39) Increased proteolysis by the cathepsins (and other proteases) is thought to contribute progression of the disease by weakening the arterial wall and allowing infiltration and migration of monocytes into the wall and SMCs from the media to intima. Specifically, cathepsin S-deficient monocytes are not able to migrate through membranes containing an endothelial monolayer, collagen, and SMCs. (39) Additionally, increases in protease activity are thought to degrade the ECM of the fibrous cap over the plaque helping to lead to either erosion or rupture. (37, 38)

Atherosclerotic lesions are dangerous because they can lead to thrombosis and occlusion of the blood vessel. Thrombosis typically occurs as a result of either erosion or rupture of the plaque. Erosion damage occurs when the endothelial cells lining the vessel lumen become disrupted; this desquamation of the lumen exposes the underlying collagen to the blood which can activate platelets and trigger thrombosis. (27) The other and most common form of plaque disruption leading to thrombosis is plaque rupture. This typically occurs in plaques that have developed a very thin fibrous cap over a large lipid laden region. When the plaque ruptures, its contents come in contact with the bloodstream leading to thrombus formation. In some cases the thrombosis may not completely occlude the vessels, but instead it will heal itself creating a thick fibrous lesion that even more significantly narrows the lumen. (27)

While plaque erosion or rupture can be catastrophic to the patient, many people present few symptoms until thrombosis occurs. However, the American Heart Association, AHA, has been working on determining a number of preclinical signs that

can assess people's risk factors for the disease. These subclinical markers include coronary artery calcification (CAC), increased carotid intima-media thickness (cIMT), increased arterial stiffness (or vascular compliance), and impaired brachial artery flow-mediated dilation (FMD). (26) Coronary artery calcification, which is measured using computed tomography (CT) of chest, detects calcium deposits in the arteries which indicate some degree of atherosclerosis including levels below clinically significant lesions. Carotid intima-media thickness (cIMT) which is assessed via ultrasound is considered to be an even earlier marker of atherosclerosis since thickening is thought to occur prior to early lesion formation including calcification. Arterial stiffness can be measured directly in arteries that may be accessed via ultrasound (e.g., common carotid, brachial, femoral arteries). Pulse wave velocity, measured by applanation tonometry is another measure used to assess arterial stiffness of the aorta. Flow mediated dilation is measured by ultrasound; the brachial arterial diameter is measured before and after 5-minutes of occlusion with a blood pressure cuff, which induced reactive hyperemia. Reactive hyperemia and high post-occlusion flow stimulates nitric oxide release, resulting in vasodilation; impaired FMD indicates endothelial function. The last three of these techniques allow noninvasive early detection of atherosclerosis risk factors before any detectable plaques are formed and may provide a way for doctors to monitor patient's risk factors and health.

### **2.3 Pathology of HIV-1**

The Acquired Immune Deficiency Syndrome (AIDS) is a global epidemic with over 34 million people worldwide living with infection with the human immunodeficiency virus-1 (HIV-1) its causative agent (40). HIV-1 is a member of the

lentivirus family of retroviruses, which contain RNA that is converted to DNA in the cell with a reverse transcriptase enzyme. HIV-1 can infect a variety of cells in the body; however, it primarily infects CD4 positive lymphocytes. The virus binds to the CD4 surface protein before entering the cell, which causes a conformation change that enables fusion and entry into the cell (41). HIV is replicated mostly in helper T cells (CD4+) but is also found in macrophages, monocytes, B lymphocytes, natural killer cells, eosinophils, and dendritic cells.(41) The progression from initial infection to the development of AIDS is marked by an increased viral count and a decrease in the quantity of T cells. Cell death is thought to be primarily caused by accumulation of viral DNA in the cytoplasm or induced apoptosis. This decrease in helper T cells prevents the activation of other immune cells in response to future infections making the person more susceptible to opportunistic infections. These secondary opportunistic infections are often the cause of death in patients with advanced AIDS.

The virus contains nine genes; the *gag* and *env* encode the structural proteins, the *pol* gene encodes the reverse transcriptase, and the other 6 genes, *tat*, *nef*, *rev*, *vif*, *fpr*, and *vpu* encode for regulatory proteins. The viral replication process consists of several steps. First, the viral envelope must bind to the specific cell surface receptor on the host cell; specifically, the gp120 protein of the *env* gene binds to CD4 receptor as well as to CC and CXC chemokine receptors. Next, the gp41 tail on the envelope undergoes a conformation change that pulls the cell membrane and viral envelope together to promote fusion and thus entry of the virus into the cell. The viral RNA is transported into the host cell's nucleus where the reverse transcriptase in the *pol* gene helps transcribe the RNA into DNA. The viral DNA is then inserted into the cell's chromosomal DNA with the

help of the integrase protein in *pol*. The newly inserted viral genes are then transcribed more quickly with the aid of the *tat* protein. These new transcripts are transported to the cytoplasm in a process regulated by *rev*. Once in the cytoplasm the RNA is either packaged or translated in proteins. The structural proteins from *gag* and *env* move towards the cell surface, and the virus begins the budding process eventually separating from the host cell as a newly formed viral particle containing proteins and RNA transcripts. During the budding processes the protease (*pol* gene) must cleave several precursor proteins into their mature form in order for the virus to mature and have ability to infect new cells (42).

#### **2.4 Antiretroviral Therapy**

Since it was recognized that AIDS is caused by a virus, a number of drugs that attempt to prevent viral replication by inhibiting the virus at various stages within its replication cycle have been developed. There are six types of drugs: nucleoside reverse transcriptase inhibitors (NRTIs), nonnucleoside reverse transcriptase inhibitors (NNRTIs), protease inhibitors (PIs), integrase inhibitors, entry inhibitors (EIs), and CCR5 co-receptor antagonists (43, 44). Specifically, for highly active retroviral therapy (HAART) patients are given a combination of three drugs with typically at least one NRTI and a PI or NNRTI (45).

The first antiretroviral drug developed was azidothymidine, AZT, which is a nucleoside reverse transcriptase inhibitor (NRTI). NRTI's name is due to its similarity to the nucleosides that are the building blocks of RNA and DNA. However, these drugs differ from natural nucleosides in that their hydroxyl group (-OH) is replaced with another group that makes them incompatible with DNA elongation. Therefore, the drugs prevent viral replication by competing with natural nucleosides and impairing the reverse

transcription of the viral RNA into DNA. (46) Nonnucleoside reverse transcriptase inhibitors (NNRTIs) are a class of drugs that also interfere with reverse transcription stage of the viral cycle; however, NNRTIs bind to the viral reverse transcriptase enzyme preventing it from functioning. (46)

The HIV-1 protease enzyme is important in producing functional and infectious viral particles by cleaving the polypeptide chains to allow the proper proteins to fold and form. Protease inhibitors (PI) are a class of ARV's that interfere with the function of the protease's enzymatic actions prevent the viral particles that are produced from becoming mature infectious viruses capable of further replication. (46) Integrase inhibitors similarly bind to the viral integrase enzyme inhibiting the virus's ability to incorporate the viral DNA into the host cell DNA which is necessary for replication as RNA transcripts for new particles are made from the viral DNA once incorporated in the host cell DNA. (44) Entry inhibitors (EIs) or fusion inhibitors bind to the gp41 protein on the viral membrane. This prevents the protein from undergoing the necessary conformational changes to pull the virus closer to the cell membrane and eventually facilitate fusion of the virus to the cell and entry of its contents. (46) The newest class of antiretroviral medications is CCR5 co-receptor antagonists, which differ from the others in that they bind to the host cell rather than the viral components. Specifically, they bind the CCR5 co-receptor on the cell surface preventing the virus from binding and thus inhibiting viral infection of the cells. (44) Currently, many studies are trying to optimize the treatment of patients with resistance or poor response to previous drug regimes by incorporating the newer drugs in these last 3 classes.

## **2.5 Non-AIDS Related Complications**

The development and implementation of HAART has been effective at delaying the progression to the development of AIDS and increasing the life expectancy of HIV positive patients to begin to approach normal life expectancy. (47) However, the longer lifespan has led to the emergence of a number of other complications and conditions that were not observed prior to widespread use of HAART. (48) Several different serious (potentially fatal) infections are still prevalent in HIV patients, despite the immune recovery on HAART. (49) In particular, tuberculosis (TB) rates among HIV patients are still significantly higher than the general population. This could be partially due to the difficulty in diagnosing latent TB before starting HAART; the decision of when to start HAART in known TB positive patients is also difficult due the potential toxicity of taking both antituberculosis and antiretroviral drugs at the same time. (49-51) Hepatitis B is also a common co-infection with HIV partially because HIV infection modifies the behavior of hepatitis B affecting treatment strategy. (52) Similarly, hepatitis C is another common co-infection due the limited effectiveness of traditional treatments in HIV patients. End-stage liver disease related to hepatitis C is one of the leading causes of non-AIDS related death in HIV patients. (49, 53)

Cancers and malignancies are a common cause of death in HIV patients at incidence rates above that of the general population. However, the relationships between the virus, immunodeficiency, HAART, and cancer and malignancies still remain unclear. AIDS-defining malignancies include Kaposi sarcoma, non-Hodgkin lymphoma and cervical cancer while non-AIDS-defining malignancies include lung, anal canal,

gastrointestinal tract, liver, urogenital tract, upper airway, or other haematological cancers. (49, 54)

Many HIV patients who begin HAART treatment with late stage disease often have a counterintuitive decline in their health and increase in complications despite the recovery of their CD4+ counts. This response known as either immune restoration disease (IRD) or immune reconstitution inflammatory syndrome (IRIS) is thought to be the result of the restored immune system's hyperinflammatory response to any otherwise subclinical or quiescent pathogen. However, currently there is no standard to either avoid or manage the syndromes. (49, 55, 56)

Other complications common in HIV patients include progressive multifocal leukoencephalopathy, cognitive disorders, liver disease, bone and kidney disorders, and cardiovascular disease. Progressive multifocal leukoencephalopathy, a fatal disease where the myelin sheathes of nerves become damaged, is considered an AIDS-defining disease due to its prevalence in HIV patients. Interestingly, while HAART treatment generally leads to lower JCV (John Cunningham virus) levels (the causative agent of multifocal leukoencephalopathy), some patients see new onset or worsening of the disease following initiation of HAART, which is thought to possibly be due to increased inflammatory reactions with increased immune counts while on HAART. (49, 57) Cognitive disorders specifically dementia are also prevalent in the HIV patients, and while its pathogenesis is thought to be related to HIV proteins or systemic immunological effects, the pathways and early markers are unclear as well as the impact of HAART therapy. (49, 58) Non-alcoholic fatty liver disease is also common in HIV patients likely resulting from metabolic syndrome. Specific complications include hepatic steatosis,

non-alcoholic steatohepatitis, liver fibrosis, cirrhosis, and hepatocellular carcinoma. (49, 59) Bone disorders in HIV patients include osteopenia and osteoporosis, these conditions occur even in HAART naïve patient indicating that the virus itself plays a significant role in development while the role of HAART drugs remains unknown. (60) Before the implementation of HAART, glomerular conditions were the primary observed renal disorder; however, since HAART, tubular disorders including Faconi's syndrome have increased. In general, renal function is closely monitored in HIV patients as diagnosed conditions often have a poor prognosis. (49, 61) Finally, the incidence of cardiovascular disease is higher in the HIV population than the general population with studies suggesting that both HIV infection and HAART therapy play roles in its development. (49, 62-69)

## **2.6 HIV and Cardiovascular Disease**

HIV-1 patients have accelerated development of cardiovascular disease (49, 62-71) Due to the difficulty in conducting well controlled clinical studies, it is difficult to distinguish if the virus or the therapy is the major cause of the cardiovascular complications; however, a number of studies with varying degrees and stages of HAART therapy indicate that carotid intima-media thickening (cIMT) (8, 72-77), arterial stiffening (8, 78, 79), and endothelial dysfunction (8, 73, 78, 80, 81), early indicators in the development of atherosclerosis, are associated with HIV-1 in patients. Specifically, a study by van Vonderen et al. found that patients with HIV infection had significant differences in cIMT and stiffness of the carotid and femoral arteries from healthy control subjects with HIV patients having both thicker and stiffer arteries. Additionally no significant difference in cIMT was seen between the ART and ART naïve patients in the

study. (77) Another study by the same group found that while cIMT did increase for patients on two different HAART regimens over the course of the 24 month study, the carotid and brachial artery stiffness did not change though femoral artery stiffness did increase. (8) However interestingly, plasma indicators of endothelial function and inflammation including von Willebrand factor (vWF), soluble vascular cell adhesion molecule (VCAM-1), and soluble intercellular adhesion molecule (ICAM-1) improved over 24 months from the baseline values in the HAART naïve patients. This improvement in endothelial function markers seems to indicate that endothelial dysfunction may be caused by the HIV-1 virus and thus drugs to lower viral loads improved endothelial function. A study by Blum et al. also seems to confirm this hypothesis that endothelial function is dependent on viral load. (82) Ultrasound measurements of brachial artery dilation using methods for both endothelium dependent and independent dilation were taken in 24 HAART naïve patients with various levels of viral load. Endothelium-independent vasodilation was the same between groups, but the group with high viral loads had significantly less endothelium-dependent vasodilation than the low viral load group. Even after 3 months of antiretroviral treatment, the same inverse correlation between viral load and endothelial function was observed. Similarly, Oliviero et al. also observed both increased cIMT and impaired FMD of brachial artery in a cohort of HIV patients when compared to controls matched for metabolic risk factors (73), endothelial function was also impaired in a study in a study of low cardiovascular risk HIV patients (83), Hsue et al. showed that HIV patients have a larger cIMT that progressively thickens more rapidly than non HIV patients(72), and HIV positive

children without other cardiovascular risk factors were also found to have both arterial stiffening and endothelial dysfunction (78).

While HIV-1 is not believed to infect vascular endothelial cells *in vivo*, the dysfunction is thought to be caused by exposure of the cells to circulating infected CD4+ T cells, macrophages, and monocytes and HIV-1 viruses and proteins in the blood. HIV infected individuals have also been shown to have higher levels of reactive oxygen species (ROS), which can also cause endothelial dysfunction. (81) In particular the Tat protein, which is actively secreted by infected cells, has been found to have a variety of negative effects. Tat has been shown to decrease the ability of pig coronary arteries to dilate by the inhibiting the expression of nitric oxide synthase (NOS) and thus nitric oxide availability. (84) A study by Park et al. exposes cultured human lung microvascular endothelial cells to Tat and observed another of effects the protein had on the cell response. They found that treatment increased the secretion of monocyte chemoattractant protein-1 (MCP-1); migration of CD14+ monocytes and THP-1 monocytic cells in transwell inserts showed that the MCP-1 from the endothelial cell supernatants was indeed chemoattractant and increased migration. The study also investigated the signaling pathways activated by Tat that lead to the MCP-1 migration and found that MCP-1 was regulated by surface molecules Flk-1 and Flt-1 and PKC intracellularly. (85) Matzen et al. also investigated the effects of Tat on adhesion of monocytes and T-cells to endothelial cells. *In vitro* adhesion assays showed that HIV-1 (sometimes in synergy with TNF- $\alpha$ ) increased adhesion of both primary monocytes and T-lymphocytes to human microvascular endothelial cells. Similar results were seen using in ear venules of mice following injection of Tat (and TNF- $\alpha$ ). (86) Numerous other studies have found

various other effects of Tat, gp120, Vpu, and Nef proteins on endothelial cells including expression of several cell adhesion molecules, increasing endothelial permeability, cell proliferation, increased cytokine signals, induced apoptosis, and increased oxidative stress. (81)

## **2.7 HAART and Cardiovascular Disease**

While the HIV virus itself has been implicated in the development of cardiovascular disease, several studies have implicated HAART in the disease progression. (70, 87, 88) The various HAART drugs are also known to have negative effects on endothelial and vascular cells that could contribute to the increased cardiovascular disease in HIV patients as evidenced by increased carotid intima-media thickness (8, 72), arterial stiffening (8, 78, 79), and endothelial dysfunction (89-93). In one clinical study by van Vonderen et al., two of the measured clinical markers of atherosclerosis, increased IMT in the carotid and stiffness in the femoral artery, both further increased even with the initiation of HAART in previous therapy naïve patients. (8) Increased arterial stiffness is also confirmed by another study which found exposure to NRTIs or PIs independent factors associated with increased stiffness as measured by heart rate corrected augmentation index. (79) Blanco et al. also investigated endothelial function in HIV-infected patients with low coronary risk factors. (83) The study found the FMD of the brachial artery was significantly reduced between the HIV patients on HAART and control subjects. The HAART naïve patients showed an intermediate impairment of FMD but it was not significantly different from either group. Other studies had similar results with HIV patients receiving PIs in their HAART regimen having decreased vascular reactivity than HIV negative patients and HIV positive

patients not receiving PIs.(89) A study by Shanker et al. found that endothelium-dependent dilation in arteries in the leg was impaired after healthy HIV negative patients were given the PI indinavir for 4 weeks. (91)

On an *in vitro* scale, NRTIs, (which includes AZT), are the class of HAART drugs that have been most extensively studied with respect their effect on endothelial cells. In particular NRTIs are thought to interfere with mitochondrial DNA replication and repair resulting in damage to cells. (94) Hebert et al. found that AZT caused significant decreases in cellular respiration, a marker for mitochondrial activity. In the study, human umbilical vein endothelial cells were cultured with media containing the NRTI AZT, the PI indinavir, or AZT and indinavir. They observed increases in cell death in all of the treated groups as well as large (3-10 fold) decreases in oxygen consumption and ATP production, both markers of mitochondrial function. The endothelial cells also showed increased endothelin-1 (ET-1) production. ET-1 acts as both a vasoconstrictor and a mitogen, and its increased production resulted in increased proliferation of both endothelial cells and vascular smooth muscles cells in co-culture. (95) Another study with AZT found that treatment of healthy mice with AZT for 35 days reduced the endothelial-dependent dilation of the aorta when exposed to acetylcholine while the non-endothelial dependent dilation response to nitric oxide (NO) (administered as sodium nitroprusside, SNP ) was the same for the wildtype and treated mice. Additionally, the treatment had no effect on the aortic contractility when exposed to either potassium chloride (KCl) or phenylephrine (PE). Additionally, the vessels had significantly increased levels of superoxide levels. (96)

The other class of HAART drugs associated with increased cardiovascular disease is the protease inhibitors (PIs). The same study by Hebert et al. also found that indinavir (a PI) also had a negative effect on the mitochondria as evidenced by decreased oxygen consumption. (95) Endothelial cells showed an increase in oxidative stress and monocyte adhesion in response PIs and HAART combinations was observed in a study by Mondal et al. (97) Human aortic endothelial cells in culture were exposed to indinavir (PI), nelfinavir (PI), zidovudine/AZT (NRTI), efavirenz (NNRTI), or two different HAART cocktails containing AZT, efavirenz, and one of the two PIs. Exposure to both HAART cocktails stimulated ROS production 1.5-2.5 fold over control (untreated) cells. Monocyte adhesion assays showed that both PIs stimulated adhesion while the other two drugs alone had little effect. However, the combinations of the different classes in the HAART cocktails increased the adhesion even more than any of the drugs alone. Both ELISA and RT-PCR also showed increases in the cellular adhesion molecules, which play a role in monocyte adhesion. Another study with human endothelial cells in vitro showed that culture with the PI ritonavir increased permeability, decreased the production of tight junction proteins, and increased the level of superoxide production. (98) Additionally, the PIs amprenavir, indinavir, and ritonavir have been shown to increase cholesterol and cholesteryl ester uptake in macrophages independent of dyslipidemia. This increased uptake of cholesterol is instead thought to be regulated by CD36, as evidenced by upregulation of CD36 in cells treated the PIs, while treatment with CD36 inhibitors prevent the increased uptake. Additionally, mice treated with CD36 inhibitors showed less signs of atherosclerotic lesion formation than the control animals. (99) The NNRTI, efavirenz has also been shown to have pro-atherosclerotic effects on endothelial

cells as well. Specifically, human aortic endothelial cells exposed to efavirenz showed an increase in the permeability of a confluent endothelial monolayer and a corresponding decrease in the tight junction proteins of ZO-1, claudin-1, occluding, and JAM-1. Staining with dihydroethidium also indicated an increase in the levels of ROS produced by the cells, which could potentially be the result of the observed decreased mitochondrial membrane potential in the treated cells. (100) In conclusion, the primarily *in vitro* work thus far shows that antiretroviral drugs do indeed have negative effects on the cells, but importance of these effects leading to quantifiable changes in the vasculature and disease states still remains to be determined.

## 2.8 Vascular Mechanics

In vivo, arteries are under constant multiaxial mechanical loading. Pulsatile blood pressure distends the vessel and induces a cyclic circumferential stress while blood flow through the vessel induces a shear stress along the luminal wall. Finally the vessels are under an axial load in vivo, which is demonstrated by their retraction upon excision. (24)

The means of these three stresses are defined as follows:

$$\tau_w = \frac{4\mu Q}{\pi r_i^3} \quad \sigma_\theta = \frac{Pr_i}{h} \quad \sigma_z = \frac{f}{\pi(r_o^2 - r_i^2)} \quad (2.1)$$

where  $\tau_w$  is mean wall shear stress,  $\sigma_\theta$  is mean circumferential stress,  $\sigma_z$  is mean axial stress,  $\mu$  is viscosity of the blood,  $Q$  is the luminal blood flow rate,  $r_i$  is the inner (luminal) radius,  $r_o$  is the outer radius,  $P$  is the transmural pressure,  $h$  the wall thickness, and  $f$  is the axial force. Besides changing geometric parameters (i.e. inner diameter or thickness) in response to mechanical perturbations, vascular remodeling can also change the compliance or stiffness of the vessel wall.

Previous studies have shown that vessels respond and remodel to changes in these loading conditions. A well known study by Kamiya and Togawa showed that wall shear stress was restored to an original value in canine carotid arteries subjected to increased flow. (101) Clark and Glagov found that aortic thickening during development was correlated to mean circumferential stress, and a study by Jackson et al. indicated that axial stress is regulated by remodeling as well. (102, 103) In addition to restoring mean stress, cells also appear to respond to restore local changes in stress as well. For example Matsumoto and Hayashi showed that the different layers of blood vessels thicken to different degrees in response to supra-physiologic loading with the inner layers increasing the most due to the highest stress in that layer. (104) Thus vascular cells including endothelial cells, smooth muscle cells, and fibroblasts have the ability to sense mechanical changes and respond via a variety of mechanisms including production of vasoactive molecules, extracellular matrix (ECM), and ECM-degrading proteases. Additionally, HIV-1 and HAART drugs cause physiologic changes that can perturb normal cell behavior and lead to changes in the vascular wall.

## **2.9 Constitutive Models of Blood Vessels**

While we know that cells respond to stresses in their local environment, these forces and stresses cannot be measured directly; thus there is a need to create constitutive models of the material behavior of the vessels in order to calculate these stresses. In order to develop the proper constitutive model we must first consider the characteristics of the blood vessel. Specifically, arteries have a highly nonlinear behavior with an initial compliant region and stiffer later response.(105) Arteries are also considered to be pseudoelastic for the models; this term was first developed by Fung to characterize

arterial behavior since the observed hysteresis indicates that the vessels are not completely elastic but they do have repeatable loading and unloading curves that can be modeled separately.(106) Histology and mechanical tests also indicate arteries are anisotropic with differing material properties in the circumferential and the axial directions, though due to symmetry they are usually assumed to have transverse or orthotropic isotropy. Due to their layered natures, arteries are heterogeneous though intima layer is thought to have little effect on the mechanics. Additionally, it has been suggested that because the adventia is relatively thin for many of the commonly studied arteries it can be assumed that that vessel wall is relatively homogeneous despite the different compositional and mechanical behavior of each layer. (25, 106, 107) Finally, while it is known that arterial wall contains both solids (ECM proteins and cells) and water (intra and extracellular), it is often modeled as an incompressible solid rather than a composite mixture of solid and fluid since the movement of water in/out of the vessels is minimal. (25)

Several different groups have previously developed models for the artery with differing degrees of complexity. Chuong and Fung developed a three dimensional constitutive relation for arteries that is still widely used for vascular modeling. (21) The model represents the strain energy function,  $W$ , as an exponential equation with six parameters that are fit to the data. A slight variation of this model by Holzapfel and Weizsacker includes one more term before the Fung-type exponential to help incorporate the initial stiffening then softening response observed in vessels before the non-linear stiffening response captured by the Fung model. (108) While these early models captured the behavior of the arteries, they were phenomenological in the sense that the parameters

lacked much physical meaning in terms of the arterial structure. Thus Holzapfel developed a fiber model for arterial behavior, which begins to incorporate the histological observed structure by modeling the vessels as an isotropic non-collagenous matrix with two helically wound embedded fibers (collagen). (23) There were a few groups that developed more structural models before the Holzapfel; however, they were not widely adopted (109, 110). This model by Holzapfel has been adapted by others including Baek, who created four fibers (axial, circumferential, and two helical) (111).

Many models (even the three dimensional/thick walled models) model the artery as a single layer; however, several groups have attempted to model the vessel as two layers; a media and adventitia. The fiber model by Holzapfel was two layers with each layer having its own unique material parameters, fiber angles, and geometry (radius, thickness, and opening angles) (23). Other two layer models include earlier ones by von Maltzahn, Demiray and Vito, and Rachev (112, 113).

Another feature of arteries that is neglected by most models is the active properties of arteries. The smooth muscle cells within the arterial wall have the ability to contract and relax in response to stimuli and to control the hemodynamics in the vessels. Therefore, the active properties also can affect the distensibility of the arteries and thus including them in the mechanical analysis can provide a more accurate model. However, accurately determining the active response of arteries is difficult since excision and external manipulation of the arteries to prepare them for testing could possibly change their response (i.e. damage may occur); this difficulty explains the reason the active response of smooth muscles is often neglected from analysis. However, several papers by Rachev & Hayashi and Zulliger et al. have presented formulations for incorporating

active smooth muscle. (114, 115) Despite the numerous different constitutive models available there is still room for improvement to create even more structurally based models and develop model which not only use algorithms to fit parameters but also contain some experimentally tractable parameters; aim 1 of this dissertation details the creation of this new microstructurally motivated model.

## CHAPTER 3

### **Specific Aim 1: Develop a microstructurally based constitutive model of arteries.**

#### **3.1 Introduction**

Mechanically mediated vascular remodeling occurs as vascular cells sense and respond to their local mechanical environment. Thus, fundamental to many studies of vascular remodeling is the quantification of the local mechanical environment under specific loading conditions; i.e., determining the distribution of stresses and strains of a vessel under applied loads (e.g., pressure, axial extension, luminal flow, etc.) Knowledge of the constitutive behavior of the vessel wall allows one to predict the local stresses and strains throughout the wall for a vessel of known geometry and applied loads. Given that the material response of biological tissues is governed by their internal constitution (i.e., cell and extracellular matrix content and organization), many argue that a predictive, widely applicable constitutive relation for arteries and other soft tissues must include parameters that account for the underlying microstructure (116-119). Such models will be particularly useful in quantifying remodeling responses associated with development, aging, disease progression, and clinical interventions, where the evolution of structural parameters may be experimentally quantified.

In this aim, we created newly proposed constitutive models by fitting biaxial mechanical data from mouse carotid arteries that incorporated four structurally significant constituents (collagen, elastin, smooth muscle, and water) into the formulations. We used previously reported biaxial biomechanical behavior and geometry of mouse carotid arteries exposed to normal pressure and luminal flow but altered axial extension to determine parameters and evaluate the model (120). We created several variants of a rule

of mixtures constitutive models (121) which we compared to both the model by Chuong and Fung (122) and a four fiber-family model (123). In addition to minimizing the error between experimental data and model predictions, we imposed penalties that required each constituent to be structurally significant. That is, we enforced penalties that encouraged parameter sets in which elastin contributes significantly to the overall response over low loads and collagen dominates the response over high loads. These constraints ascribe additional microstructural ‘meaning’ to the constitutive model. Whereas imposing such penalties necessarily reduces the goodness of fit of model predictions to experimental data, we submit that the marginal reduction in the goodness of fit observed in our results was off-set by the improved structural interpretation.

## 3.2 Methods

### 3.2.1 Theoretical framework

Kinematics: In traditional vascular mechanics, one typically considers three configurations: a loaded configuration  $\beta_t$ , a traction-free (unloaded) configuration  $\beta_u$ , and a (nearly stress-free) reference configuration  $\beta_o$ ; see Chuong and Fung (122). For inflation and extension of an axisymmetric tube, the deformation gradient, right Cauchy Green strain, and Green strain tensors have components

$$\begin{aligned} [\mathbf{F}] &= \text{diag} \{ \lambda_r, \lambda_\theta, \lambda_z \}, & [\mathbf{C}] &= \text{diag} \{ \lambda_r^2, \lambda_\theta^2, \lambda_z^2 \}, \\ [\mathbf{E}] &= \text{diag} \{ (\lambda_r^2 - 1) / 2, (\lambda_\theta^2 - 1) / 2, (\lambda_z^2 - 1) / 2 \} \end{aligned} \quad (3.1)$$

where

$$\lambda_r = \frac{\partial r}{\partial R} \quad \lambda_\theta = \frac{\pi r}{\Theta_o R} \quad \text{and} \quad \lambda_z = \lambda \Lambda, \quad (3.2)$$

and  $\Lambda$  and  $\lambda$  are the axial stretches for the motions from  $\beta_o$  to  $\beta_u$  and from  $\beta_u$  to  $\beta_t$ , respectively and  $\Theta_o$  is the sectorial angle in  $\beta_o$ . If the material is assumed to be incompressible,  $\det(\mathbf{F}) = 1$  and the current radius may be related to the reference radius as

$$r = \sqrt{\frac{\Theta_o}{\pi\lambda\Lambda}(R^2 - R_i^2) + r_i^2} \quad \text{or} \quad r = \sqrt{r_o^2 - \frac{\Theta_o}{\pi\lambda\Lambda}(R_o^2 - R^2)}, \quad (3.3)$$

where  $R_i$  and  $R_o$  are the inner or outer radii in  $\beta_o$  and  $r_i$  and  $r_o$  are the inner and outer radii in  $\beta_t$ . Thus, given measured values for the reference configuration ( $R_i$ ,  $R_o$ , the stress-free axial length  $L_z$ , and  $\Theta_o$ ) and the current configuration ( $r_o$  (or  $r_i$ ) and the loaded length  $\ell$ ), the components of  $\mathbf{F}$ ,  $\mathbf{C}$ , and  $\mathbf{E}$  are easily calculated.

Unfortunately, in Gleason et al. (124), opening angle measurements were not performed for the freshly isolated and cultured vessels. Thus, here we approached the problem in an inverse fashion. Let us prescribe the state of strain in the *in vivo* (loaded) configuration. Let the inner radius, outer radius, and length in the *in vivo* configuration be denoted  $r_i^h$ ,  $r_o^h$ , and  $\ell^h$ , and let the homeostatic stretches be denoted  $\lambda_\theta^h(r)$ ,  $\lambda_z^h(r)$ ,  $\lambda_r^h(r)$ , where  $\lambda_r^h = 1/\lambda_\theta^h\lambda_z^h$ . Now, we may define the true stress free (or natural) configuration of a material point located in a current configuration at radius  $r \in [r_i, r_o]$  by defining a reference radius and length, as

$$L_\theta^n(r) = 2\pi R^n(r) = \frac{2\pi r^h}{\lambda_\theta^h(r^h)} \quad \text{and} \quad L_z^n(r) = \frac{\ell^h}{\lambda_z^h(r)}, \quad (3.4)$$

where  $R^n$  is the radius and  $L_z^n$  is the axial length of a cylindrical shell for which the stress is zero (for this material point);  $L_\theta^n$  is the arc length of this cylindrical shell. Given

equation 3.4 in any (tubular) configuration with inner radius  $r_i$  and length  $\ell$ , the current radius may be calculated via incompressibility as

$$r = \sqrt{\left( (r^h)^2 - (r_i^h)^2 \right) \frac{\ell^h}{\ell} + r_i^2} \quad (3.5)$$

and the stretches may be calculated as

$$\lambda_\theta(r) = \frac{r}{R^n} = \frac{2\pi r}{L_\theta^n} \quad \lambda_z(r) = \frac{\ell}{L_z^n} \quad \lambda_r(r) = \frac{1}{\lambda_\theta \lambda_z} = \frac{R^n L_z^n}{r \ell} = \frac{L_\theta^n L_z^n}{2\pi r \ell}. \quad (3.6)$$

Given these stretches the components of  $\mathbf{F}$ ,  $\mathbf{C}$ , and  $\mathbf{E}$  for extension and inflation are easily calculated via equations 3.1.

Equilibrium: For inflation and extension of a long, straight, axisymmetric tube, equilibrium requires that  $T_{r\theta} = T_{rz} = 0$  and  $\partial T_{rr} / \partial r + (T_{rr} - T_{\theta\theta}) / r = 0$ . Noting that  $-T_{rr}(r_i) = P$  is the luminal pressure and  $T_{rr}(r_o) = 0$ , equilibrium requires that

$$P = \int_{r_i}^{r_o} (\hat{T}_{\theta\theta} - \hat{T}_{rr}) \frac{dr}{r} \quad (3.7)$$

where

$$\mathbf{T} = \hat{\mathbf{T}} - p\mathbf{I} \quad \text{and} \quad \hat{\mathbf{T}} = 2\mathbf{F}(\partial W / \partial \mathbf{C})\mathbf{F}^T \quad (3.8)$$

$\hat{\mathbf{T}}$  is the so-called ‘extra’ stress due to the deformation and  $W$  is the strain energy density function. Axial equilibrium requires that the magnitude of the axial force,  $f$ , maintaining the *in vivo* axial extension be

$$f = 2\pi \int_{r_i}^{r_o} T_{zz} r \, dr - \Gamma(\pi r_i^2 P), \quad (3.9)$$

where the first term on the right hand side is due to the traction force applied to the vessel wall and the second term on the right hand side is due to the pressure acting over the end-

cap;  $\Gamma = 1$  or  $0$  for a closed or open ended tube, respectively. Equation 3.9 can be written as

$$f = \pi \int_{r_i}^{r_o} (2\hat{T}_{zz} - \hat{T}_{\theta\theta} - \hat{T}_{rr}) r dr + \pi r_i^2 P(1 - \Gamma) \quad (3.10)$$

see Humphrey (125). For *ex vivo* biomechanical testing,  $\Gamma = 1$ . Given equations 3.2 and 3.2 or 3.6 the components of the ‘extra’ stress may be calculated as

$$\hat{T}_{ii} = 2(F_{ii})^2 \left( \frac{\partial W}{\partial c_{ii}} \right) = (F_{ii})^2 \left( \frac{\partial W}{\partial E_{ii}} \right) \quad (\text{no sum}) \quad (3.11)$$

where  $i = r, \theta, \text{ or } z$ .

### 3.2.2 Phenomenological Models

We considered the model of Chuong and Fung (122) and a four fiber-family model in addition to several variants of a rule of mixtures model to describe the constitutive behavior of these vessels.

Fung Model: Consider the strain energy function of Chuong and Fung (122)

$$W = (c/2)[e^Q - 1] \quad (3.12)$$

where

$$Q = c_1 E_{\theta\theta}^2 + c_2 E_{zz}^2 + c_3 E_{rr}^2 + 2c_4 E_{\theta\theta} E_{zz} + 2c_5 E_{rr} E_{zz} + 2c_6 E_{rr} E_{\theta\theta}, \quad (3.13)$$

and where  $c$  and  $c_{1-6}$  are material parameters. Given this strain energy function, the components of the extra stress due to the deformation are

$$\begin{aligned} \hat{T}_{rr} &= c\lambda_r^2 [c_3 E_{rr} + c_5 E_{zz} + c_6 E_{\theta\theta}] \exp [Q] \\ \hat{T}_{\theta\theta} &= c\lambda_\theta^2 [c_1 E_{\theta\theta} + c_4 E_{zz} + c_6 E_{rr}] \exp [Q] \\ \hat{T}_{zz} &= c\lambda_z^2 [c_2 E_{zz} + c_4 E_{\theta\theta} + c_5 E_{rr}] \exp [Q] \end{aligned} \quad (3.14)$$

from which  $P$  and  $f_m$  can be calculated via equations 3.7 and 3.10.

Four Fiber-Family Model: Consider a four fiber-family proposed by Baek et al. (123), which is a simple extension of the model proposed by Holzapfel et al. (118) and Spencer (126), with strain energy function

$$w = \frac{b}{2}(I_1 - 3) + \sum_{k=1,2,3,4} \frac{b_1^k}{2b_2^k} \left\{ \exp \left[ b_2^k \left( (\lambda^k)^2 - 1 \right)^2 \right] - 1 \right\} \quad (3.15)$$

where  $b$ ,  $b_1^k$ , and  $b_2^k$  are material parameters with  $k$  denoting the  $k^{\text{th}}$  fiber family,  $I_1 = \text{tr}(\mathbf{C}) = C_{rr} + C_{\theta\theta} + C_{zz}$  is the first invariant of  $\mathbf{C}$ ,  $\lambda^k = \sqrt{\mathbf{M}^k \cdot \mathbf{C} \mathbf{M}^k}$  is the stretch of the  $k^{\text{th}}$  fiber family,  $\mathbf{M}^k = \sin(\alpha^k) \mathbf{e}_\theta + \cos(\alpha^k) \mathbf{e}_z$  is the unit vector along the  $k^{\text{th}}$  fiber direction in the reference configuration, and  $\alpha^k$  is the associated angle between the axial and fiber directions. In general,

$(\lambda^k)^2 = C_{\theta\theta} \sin^2(\alpha^k) + 2C_{\theta z} \sin(\alpha^k) \cos(\alpha^k) + C_{zz} \cos^2(\alpha^k)$ , but  $C_{\theta z} = 0$  for inflation and extension tests, given material symmetry. In addition, we note that under compression the fiber-families do not contribute to the mechanical response in an exponential fashion, as they do in tension. Thus, when  $\lambda^k < 1$ , we set  $b_1^k = 0$ ; therefore, we model the vessel under compression as a neo-Hookean material. Here, we consider four fiber families with  $\alpha^1 = 90^\circ$  (circumferential),  $\alpha^2 = 0^\circ$  (axial), and  $\alpha^3 = -\alpha^4 = \alpha$  (diagonal) which is left as a variable to be determined along with the seven material parameters (with  $b_1^3 = b_1^4$  and  $b_2^3 = b_2^4$  for the diagonal fibers to ensure material symmetry) via non-linear regression.

Given this strain energy function, the components of the extra stress due to the deformation are

$$\hat{T}_{rr} = \lambda_r^2 b \quad (3.16)$$

$$\hat{T}_{\theta\theta} = \lambda_\theta^2 (b + b_1^1 (\lambda_\theta^2 - 1) \exp \{ b_2^1 (\lambda_\theta^2 - 1)^2 \}) + 2b_1^3 \sin^2(\alpha) [(\lambda^{(3)})^2 - 1] \exp \{ b_2 [(\lambda^{(3)})^2 - 1]^2 \}$$

$$\hat{\mathbf{T}}_{zz} = \lambda_z^2(b + b_1^2(\lambda_z^2 - 1) \exp\{b_2^2(\lambda_z^2 - 1)^2\} + 2b_1^3 \cos^2(\alpha) [(\lambda^{(3)})^2 - 1] \exp\{b_2 [(\lambda^{(3)})^2 - 1]^2\})$$

from which  $P$  and  $f$  can be calculated via equations 3.7 and 3.10. Note that  $\lambda^{(3)} = \lambda^{(4)}$  is the stretch in fiber  $k=3$  (and  $k=4$ ).

### 3.2.3 Microstructurally-motivated models: a discrete set of fibers

It has long been thought that elastin contributes to the highly distensible region on pressure-diameter curves of arteries at low pressures and collagen contributes to the stiff region of these curves at high pressures; see, for example, the classic paper by Roach and Burton (127). Smooth muscle cells also contribute significantly to the overall mechanical response of blood vessels, under both passive and active (contractile) conditions. Indeed, other key structural constituents have also been implicated as significant contributors to the overall mechanical response (128). The amount, organization, and mechanical state of key structural constituents can vary spatially in arteries and can vary temporally as different constituents are produced, degraded, and remodeled. As the tissue remodels and grows, constituent turnover and growth can occur at different rates and to different extents. Constrained mixture theory provides a convenient theoretical framework for quantifying the spatial and temporal variations in mechanical behavior in terms of microstructural metrics.

Constitutive Equations: Non-Uniform Constrained Mixture: We will adopt a simple rule of mixtures approach; that is, let the total stress be given as the sum of the stresses borne by key, individual structural constituents. In particular, we will follow Gleason et al. (121) and let

$$\mathbf{T} = \sum_j \phi^j(r) [\mathbf{T}^j + \mathbf{T}_{act}^j] \quad (3.17)$$

where  $\phi^j(r)$  is the mass fraction of constituent  $j$ , which may vary with position,  $\mathbf{T}$  is the total (mixture) stress at a point,  $\mathbf{T}^j$  is the (passive) stress borne by constituent  $j$ , and  $\mathbf{T}_{act}^j$  is the active (contractile) stress borne by constituent  $j$ . The passive response of each constituent will be model as an incompressible elastic material; thus,

$$\mathbf{T}^j = -p^j \mathbf{I} + 2\mathbf{F}^j \left( \partial W^j / \partial \mathbf{C}^j \right) (\mathbf{F}^j)^T \quad (3.18)$$

where we also allow the material to be *non-uniform*. That is, at each point, each passive constituent may be present at a different state of strain (i.e., possess different stress free configurations); thus, each constituent can experience different deformations.

Let us consider the passive response of the blood vessel; i.e., let  $\mathbf{T}_{act}^j = \mathbf{0}$ . Given equation 3.18, equation 3.17 may be re-written as

$$\mathbf{T} = -p \mathbf{I} + \sum_j \phi^j \hat{\mathbf{T}}^j, \quad (3.19)$$

where  $\hat{\mathbf{T}}^j = 2\mathbf{F}^j (\partial W^j / \partial \mathbf{C}^j) (\mathbf{F}^j)^T$  is the ‘extra’ stress due to the deformation for constituent  $j$  and  $p = \sum_j \phi^j p^j$  is the Lagrange multiplier which arises due to incompressibility. Analogous to equation (3.8), the ‘extra’ stress due to the deformation for the mixture is  $\hat{\mathbf{T}} = \sum_j \phi^j \hat{\mathbf{T}}^j$ .

Let us consider four key structural constituents: elastin, collagen, smooth muscle, and water. Let water be modeled as an inviscid fluid; thus  $\mathbf{T}^w = -p^w \mathbf{I}$  (and  $\hat{\mathbf{T}}^w = \mathbf{0}$ ). Let elastin be modeled as an isotropic material; we employ a neo-Hookean model for elastin,

$$W^e = b^e (I_1^e - 3) \quad (3.20)$$

where  $b^e$  is a material parameter. Let muscle be modeled as a transversely isotropic material (i.e., one fiber-family model) with a preferred circumferential direction as

$$W^m = \frac{b^m}{2}(I_1^m - 3) + \frac{b_1^m}{4b_2^m} \left( \exp \left\{ \frac{b_2^m}{2} \left( (\lambda_\theta^m)^2 - 1 \right)^2 \right\} - 1 \right) \quad (3.21)$$

where  $b^m$ ,  $b_1^m$ , and  $b_2^m$  are material parameters. Again we assume that the fibers do not contribute exponentially under compression; thus we set  $b_1^m = 0$  when  $\lambda_\theta^m < 1$ . Let collagen be modeled with a three fiber-family model

$$W^c = \frac{b^c}{2}(I_1^c - 3) + \sum_{k=1,2,3} \frac{b_1^{ck}}{2b_2^{ck}} \left\{ \exp \left[ \frac{b_2^{ck}}{2} \left( (\lambda_k^c)^2 - 1 \right)^2 \right] - 1 \right\} \quad (3.22)$$

where  $b^c$ ,  $b_1^{ck}$ , and  $b_2^{ck}$  are material parameters; again we set  $b_1^{ck} = 0$  when  $\lambda_k^c < 1$ . Here the collagen fibers are oriented at angles  $0^\circ$  and  $\pm\alpha^c$ . We neglect the contribution of the ‘isotropic’ part of equation 3.22 thus,  $b^c \approx 0$ . That is, we assume that the collagen fibers are embedded in the amorphous matrix described by the isotropic terms in equations 3.20 and 3.21.

Kinematics: Non-Uniform Constrained Mixture: The components of  $\mathbf{F}^j$  and  $\mathbf{C}^j$

for inflation and extension are easily calculated as

$$[\mathbf{F}^j] = \text{diag} \left\{ \lambda_r^j(r), \lambda_\theta^j(r), \lambda_z^j \right\} \quad \text{and} \quad [\mathbf{C}^j] = \text{diag} \left\{ (\lambda_r^j(r))^2, (\lambda_\theta^j(r))^2, (\lambda_z^j)^2 \right\}. \quad (3.23)$$

For elastin and muscle ( $j = e$  or  $m$ ), we will quantify the stretches as

$$\lambda_\theta^j(r) = \frac{r}{(R^n)^j} = \frac{2\pi r}{(L_\theta^n)^j}, \quad \lambda_z^j = \frac{\ell}{(L_z^n)^j}, \quad \lambda_r^j(r) = \frac{1}{\lambda_\theta^j \lambda_z^j} = \frac{(R^n)^j (L_z^n)^j}{r\ell} = \frac{(L_\theta^n)^j (L_z^n)^j}{2\pi r\ell} \quad (3.24)$$

where  $(R^n)^j$  is the radius and  $(L_z^n)^j$  the axial length of a cylindrical shell for which constituent  $j$  is at zero stress (for this material point);  $(L_\theta^n)^j$  is the arch length of this

cylindrical shell. Thus, in addition to determining material parameters, one must either prescribe or experimentally quantify the natural configurations  $(R^n)^j$  and  $(L_z^n)^j$  for each constituent. One way to prescribe these natural configurations is to assume that each constituent is present at homeostatic stretches  $\lambda_i^j|_h$  in an *in vivo* (homeostatic) configuration  $r = r^h$  and  $\ell = \ell^h$ ; given these stretches and this loaded geometry,  $(R^n)^j$  and  $(L_z^n)^j$  may be determined via equations 3.24.

For collagen ( $j = c$ ), we let the current and natural configurations of each fiber-family be described in terms of a fiber angle and fiber length. Let  $\omega^{jk}$  and  $\Omega^{jk}$  be the fiber angle of fiber-family  $k$  of constituent  $j$  (i.e., collagen) in the current and natural configurations, respectively, and let  $\gamma^{jk}$  and  $\Gamma^{jk}$  be the length of each fiber-family  $k$  of constituent  $j$  in the current and natural configurations, respectively. Thus, instead of prescribing the natural configuration in terms of  $(R^n)^j$  and  $(L_z^n)^j$ , we will prescribe the natural configuration in terms of  $\Omega^{jk}$  and  $\Gamma^{jk}$ . Let us assume that each fiber  $k$  of constituent  $j$  is present at homeostatic stretch  $\lambda_k^j|_h$  and a homeostatic fiber orientation  $\omega^{jk}|_h$  in the *in vivo* (homeostatic) configuration  $r = r^h$  and  $\ell = \ell^h$ . The length of the fiber in the *in vivo* configuration can be calculated as

$$(\delta^{jk})^h = \begin{cases} \frac{\ell^h}{\cos(\omega^{jk}|_h)} & \text{for } 0 \leq \omega^{jk}|_h \leq \tan\left(\frac{2\pi r^h}{\ell^h}\right) \\ \frac{2\pi r^h}{\sin(\omega^{jk}|_h)} & \text{for } \tan\left(\frac{2\pi r^h}{\ell^h}\right) \leq \omega^{jk}|_h \leq \frac{\pi}{2} \end{cases}. \quad (3.25)$$

The stress free length of the fiber can then be calculated as

$$\Gamma^{jk}(r) = \frac{(\delta^{jk})^h}{\lambda_k^j|_h}, \quad (3.26)$$

where we emphasize that the reference length of each fiber family will vary with radial location. Note, that this fiber will be stress free as long as the length of the fiber equals the unloaded length  $\Gamma^{jk}$ ; thus, the stress free configuration may be defined at any stress free fiber orientation angle  $\Omega^{jk}$ . Let us define the natural configuration, such that when the fiber length is  $\Gamma^{jk}$ , the dimensions of the cylindrical shell passing through  $r = r^h$  with length  $\ell = \ell^h$  are such that  $2\pi(R^n)^j = (L^n)^j$ . For this case,

$$\Omega^{jk}(r) = \tan^{-1} \left[ \frac{\ell^h}{2\pi r^h} \tan(\omega^{jk}|_h) \right], \quad (3.27)$$

where each fiber angle in the reference configuration will vary with radial location.

Given this natural configuration  $(\Gamma^{jk}, \Omega^{jk})$ , the fiber stretch  $\lambda_k^j$  and fiber angle  $\omega^{jk}$  in any (loaded) configuration  $\beta_t$  may be evaluated as

$$\lambda^{jk} = \begin{cases} \frac{\ell}{\Gamma^{jk} \cos(\omega^{jk}(\Omega^{jk}))} & \text{for } 0 \leq \Omega^{jk} \leq 45^\circ \\ \frac{2\pi r}{\Gamma^{jk} \sin(\omega^{jk}(\Omega^{jk}))} & \text{for } 45^\circ \leq \Omega^{jk} \leq 90^\circ \end{cases} \quad \text{and} \quad \omega^{jk} = \tan^{-1} \left[ \frac{2\pi r}{\ell} \tan \Omega^{jk} \right] \quad (3.28)$$

Thus, given values for  $\lambda^{ck}$  and  $\omega^{ck}$  via equations 3.28, we can evaluate equation 3.22.

### 3.2.4. Microstructurally-motivated models: distributions of fibers

Microscopy reveals that cells and fibrous matrix constituents, such as collagen, exhibit not just a few discrete fiber directions, but rather a continuous distribution of fiber directions. Microscopy also reveals significant variations in the undulation collagen fibers (22) as well as in the lengths of the smooth muscle cells in normal arteries. (129)

Thus, we will allow different members of each constituent class to possess different sets of natural configurations and describe the distribution of mass over these different sets of natural configurations via distribution functions.

For elastin and muscle, we adopt the approach of Gleason and Humphrey(130). Briefly, we assume that constituent  $j$  is present in the *in vivo* state at a homeostatic distribution of stretches  $\Lambda_h^j(\tilde{\lambda}_\theta, \tilde{\lambda}_z)$ . Rather than prescribing the functional form of  $\Lambda_h^j(\tilde{\lambda}_\theta, \tilde{\lambda}_z)$ , we simply prescribe the functional form of the distribution of natural configurations  $R_h^j(\tilde{R}, \tilde{L}; r)$  that results from laying down new material with the distribution of stretches  $\Lambda_h^j(\tilde{\lambda}_\theta, \tilde{\lambda}_z)$  in the (known) loaded configuration. We let  $R_h^j(\tilde{R}, \tilde{L}; r)$  be described by a Beta probability distribution function, with independent variables  $\tilde{R}$  and  $\tilde{L}$ , as

$$R_h^j(\tilde{R}, \tilde{L}; r) = \left( \frac{(\tilde{R} - R_{min}^j(r))^{p_A^j - 1} (R_{max}^j(r) - \tilde{R})^{q_A^j - 1}}{B(p_A^j, q_A^j) (R_{max}^j(r) - R_{min}^j(r))^{p_A^j + q_A^j - 1}} \right) \left( \frac{(\tilde{L} - L_{min}^j)^{p_L^j - 1} (L_{max}^j - \tilde{L})^{q_L^j - 1}}{B(p_L^j, q_L^j) (L_{max}^j - L_{min}^j)^{p_L^j + q_L^j - 1}} \right) \quad (3.29)$$

where  $p_A^j, q_A^j, p_L^j,$  and  $q_L^j$  are shape parameters,  $B(\cdot, \cdot)$  is the Beta function,  $R_{min}^j(r) = \bar{R}^j(r) - \Delta R^j/2$ ,  $R_{max}^j(r) = \bar{R}^j(r) + \Delta R^j/2$ ,  $L_{min}^j = \bar{L}^j - \Delta L^j/2$ ,  $L_{max}^j = \bar{L}^j + \Delta L^j/2$ ,  $\bar{R}^j$  and  $\bar{L}^j$  are mean values of the natural configurations, and  $\Delta R^j$  and  $\Delta L^j$  are the widths of the distribution. If we know the current state  $(r^h, \ell^h)$ , we can prescribe the mean natural configurations of the distribution as

$$\bar{R}^j = \frac{r^h}{\lambda_\theta^j|_h} \quad \text{and} \quad \bar{L}^j = \frac{\ell^h}{\lambda_z^j|_h}, \quad (3.30)$$

where  $\lambda_\theta^j|_h$  and  $\lambda_z^j|_h$  are the mean value of the preferred homeostatic stretch distribution.

We will consider collagen to be comprised of a distribution of fibers with fiber orientations  $\tilde{\omega} \in [0, 90]$  and fiber stretches  $\tilde{\lambda}_f$ . Thus, we let

$$W^c = \int_{\tilde{\Gamma}=\Gamma_1}^{\tilde{\Gamma}=\Gamma_1} \int_{\tilde{\Omega}=0}^{\tilde{\Omega}=\frac{\pi}{2}} \hat{R}^c(\tilde{\Gamma}, \tilde{\Omega}; r) \frac{b_1^c}{b_2^c} \left[ \exp\left(b_2^c \left( (\tilde{\lambda}_f)^2 - 1 \right)^2\right) - 1 \right] d\tilde{\Omega} d\tilde{\Gamma} \quad (3.31)$$

where  $\hat{R}^c(\tilde{\Gamma}, \tilde{\Omega})$  describes how the mass of collagen is distributed over all possible combinations of natural configurations  $(\tilde{\Gamma}, \tilde{\Omega})$ . Each fiber is oriented in the  $\tilde{Z} - \tilde{\Theta}$  plane,  $\tilde{\lambda}_f = \gamma / \tilde{\Gamma} = \tilde{C}_{\theta\theta} \sin^2(\tilde{\Omega}) + 2\tilde{C}_{\theta z} \sin(\Omega_n^j) \cos(\Omega_n^c) + \tilde{C}_{zz} \cos^2(\tilde{\Omega})$ , where  $\tilde{\Omega}$  denotes the angle between the fiber direction and  $\tilde{Z}$  axis in the natural configuration,  $\gamma$  is the length of the fiber in the loaded configuration, and  $\tilde{\Gamma}$  is the unloaded length of fibers oriented in the direction  $\tilde{\Omega}$ .

We will let the fibers be laid down at a homeostatic distribution of fiber angles described via a sum of normal distribution functions, given as

$$A(\tilde{\Omega}) = \left[ \frac{1}{2 \sum_p a_p} \right] \sum_p \frac{a_p}{\sigma_p \sqrt{2\pi}} \sum_{n=1}^2 \left\{ \exp \left[ \frac{-(\tilde{\omega} + (-1)^n \bar{\omega}_p)}{2\sigma_p^2} \right] + \exp \left[ \frac{-(\tilde{\omega} + (-1)^n (\bar{\omega}_p - 180))}{2\sigma_p^2} \right] \right\} \quad (3.32)$$

where following equation (3.27),  $\tilde{\omega}$  is related to  $\tilde{\Omega}$  as

$$\tilde{\omega}(\tilde{\Omega}) = \tan^{-1} \left[ \frac{2\pi r^h}{\ell^h} \tan(\tilde{\Omega}) \right], \quad (3.33)$$

and  $\bar{\omega}_p$  and  $\sigma_p$  are the mean and standard deviation of normal distribution  $p$ . Here  $p = 2$ ,  $\sigma_1 = \sigma_2 = 10^\circ$ , and  $\bar{\omega}_1 = 0^\circ$ , while  $\bar{\omega}_2$  will be solved along with material and other structural parameters via regression. In addition, we will assume that at each fiber angle,

$\tilde{\omega}$ , the fibers are laid down at a homeostatic distribution of stretches,  $\Lambda_h^c(\tilde{\lambda}_f, \tilde{\omega}; s)$ . As with elastin and smooth muscle, rather than prescribing the distribution of *in vivo* stretches and then mapping these stretches back to a reference state, we will simply prescribe the distribution of fiber lengths ( $\tilde{\Gamma}$ ) in the reference state; let this distribution be denoted as  $B(\tilde{\Gamma}, \tilde{\Omega}; r)$ , via a Beta distribution function, as

$$B(\tilde{\Gamma}, \tilde{\Omega}) = \left( \frac{(\tilde{\Gamma} - \Gamma_{min}(\tilde{\omega}))^{p^c(\tilde{\omega})-1} (\Gamma_{max}(\tilde{\omega}) - \tilde{\Gamma})^{q^c(\tilde{\omega})-1}}{B(p^c(\tilde{\omega}), q^c(\tilde{\omega})) (\Gamma_{max}(\tilde{\omega}) - \Gamma_{min}(\tilde{\omega}))^{p^c(\tilde{\omega})+q^c(\tilde{\omega})-1}} \right) \quad (3.34)$$

where we recall that  $\tilde{\omega} = \tilde{\omega}(\tilde{\Omega}; s)$ ,  $p^j(\tilde{\omega})$  and  $q^j(\tilde{\omega})$  are shape parameters,  $\Gamma_{max}(\tilde{\omega})$  and  $\Gamma_{min}(\tilde{\omega})$  are the maximum and minimum values of  $\tilde{\Gamma}$  (i.e.,  $B(\tilde{\Gamma}, \tilde{\Omega}) = 0$  for  $\tilde{\Gamma} > \Gamma_{max}$  or  $\tilde{\Gamma} < \Gamma_{min}$ ), and  $B(\cdot, \cdot)$  is the Beta function. We let  $p^j(\tilde{\omega}) = q^j(\tilde{\omega}) = 4.5$  and  $\Delta\Gamma = \Gamma_{max} - \Gamma_{min} = 0.10$ .

The distribution of mass over all combinations of fiber angle and fiber stretch may be given as

$$\hat{R}^j(\tilde{\Gamma}, \tilde{\Omega}; r) = A^j(\tilde{\omega}(\tilde{\Omega}); r) \hat{B}^j(\tilde{\Gamma}, \tilde{\Omega}; r). \quad (3.35)$$

Note that this distribution function has the properties

$$\hat{R}^j(\tilde{\Gamma}, \tilde{\Omega}) > 0, \quad \forall \tilde{\Gamma}, \tilde{\Omega} \quad \text{and} \quad \int_{\Gamma_{min}}^{\Gamma_{max}} \int_0^{\pi} \hat{R}^j(\tilde{\Gamma}, \tilde{\Omega}) d\tilde{\Omega} d\tilde{\Gamma} = 1 \quad (3.36)$$

Here, we only consider distribution functions that possess symmetry about the  $r-z$  plane and the  $r-\theta$  plane; thus the limits of integration of  $\tilde{\Omega} = 0$  to  $\pi/2$  in equation 3.31 represent the first quadrant, which is repeated in the 2<sup>nd</sup> quadrant (and in the 3<sup>rd</sup> and 4<sup>th</sup> quadrant). In equation 3.22, only symmetry about the  $r-\theta$  plane is required. Note, too, that given symmetry of  $\hat{R}^j(\tilde{\Gamma}, \tilde{\Omega})$ ,

$$\int_{\Gamma_{min}}^{\Gamma_{max}} \int_0^{\pi} \hat{R}^j(\tilde{\Gamma}, \tilde{\Omega}) d\tilde{\Omega} d\tilde{\Gamma} = 2 \int_{\Gamma_{min}}^{\Gamma_{max}} \int_0^{\pi/2} \hat{R}^j(\tilde{\Gamma}, \tilde{\Omega}) d\tilde{\Omega} d\tilde{\Gamma} = 1 \quad (3.37)$$

Therefore, from equation 3.22 to equation 3.31, we set the limits of integration of  $\tilde{\Omega} = 0$  to  $\pi/2$  and multiply by 2.

### 3.2.5 Parameter Estimation

Material parameters were determined via a nonlinear regression technique that minimized the error between measured values of  $P$  and  $f$  and calculated values of  $P$  and  $f$  from equations 3.7 and 3.10 given measured values of outer diameter and length under these measured values of  $P$  and  $f$ ; also unloaded radius, length, and thickness where measured. We employ equation 3.1, with equation 3.6, and specify the *in vivo* configuration and transmural strains in this configuration to determine  $\mathbf{F}$  and  $\mathbf{C}$ . We seek to identify material parameters via nonlinear regression with the minimization function

$$min\_fun = error + \sum_i (penalty(i))^2 \quad (3.38)$$

where

$$error = \sum_{i=1}^n \left( \frac{P_{meas}(i) - P_{model}(i)}{P_{meas}(i)} \right)^2 + \sum_{i=1}^n \left( \frac{f_{meas}(i) - f_{model}(i)}{f_{meas}(i)} \right)^2 \quad (3.39)$$

quantifies the difference between experimental data and modeling predictions and  $penalty(i)$  is a penalty function that is used to enforce several ‘side conditions’ described further below. Calculations were performed in MatLab 7.4 using the *lsqnonlin* subroutine; this subroutine allows the prescription of upper and lower limits on the parameter values. Data was taken between 0 and 160 mmHg for the  $P-d$  tests and

between 0 mN and 40 for the  $f - \ell$  tests; taken together, the three  $P - d$  tests and three  $f - \ell$  tests represent  $n = 800$  to 1200 data points.

### 3.2.6 Penalty Set

The microstructural motivation for proposing a mixture based constitutive equations 3.19-3.22 is that each constituent (elastin, collagen, muscle, and water) will be ‘structurally significant’. By structurally significant, we mean that each contributes significantly to the overall biomechanical response. Thus, in addition to minimizing the error between experimental data and the model prediction, we also seek a set of parameters that represent well the characteristic responses of each constituent. Simply identifying the material parameters in equations 3.20-3.22 by minimizing the error function 3.39, does not ensure that each constituent will contribute significantly to the overall stress. For example, a good fit may occur with  $b^e$  very small; thus, the contribution of elastin to the overall stress would be negligible. To ensure that each constituent is structurally significant, we must impose additional constraints (or penalties) on the error function during parameter estimation. We enforce the constraint that, under modest pressure, the stress in elastin contributes to at least 30% of the overall stress and under high pressure, the stress in the collagen contributes to at least 75% of the overall stress. Let us impose the following constraints.

1. For  $59 < P < 61$  mmHg and  $1.79 < \lambda_z < 1.81$ , let

$$\hat{T}_{\theta\theta}^e / \hat{T}_{\theta\theta} > 30\% \quad (3.40)$$

2. For  $159 < P < 161$  mmHg  $\lambda_z > 1.9$ , let

$$\hat{T}_{\theta\theta}^c / \hat{T}_{\theta\theta} > 75\% \quad (3.41)$$

The first constraint (equation 3.40) ensures that elastin contributes significantly under sub-physiological loading. The second constraint (equation 3.41) ensures that collagen bears much of the load over supraphysiological loading. These constraints may be enforced via the penalty method described below. For example, if the pressure and stretch are within the loading range specified and  $\hat{T}_{\theta\theta}^e/\hat{T}_{\theta\theta} > 30\%$ , then let

$$penalty(i) = penalty(i) + w(0.30 - \hat{T}_{\theta\theta}^e(i)/\hat{T}_{\theta\theta}(i))$$

where  $w$  is a weighting parameter and  $i$  denotes the  $i^{\text{th}}$  data point.

### 3.2.7 Statistical Analysis

Parameters were obtained for each of the models for all of the data sets. Data sets were from 3 groups of 6 vessels with culture stretches of  $\lambda_z^*=1.65$ ,  $\lambda_z^*=1.80$ , and  $\lambda_z^*=1.95$  on day 0 and day 2 of culture. Note, the high stretch only had 5 complete data sets. An ANOVA analysis was performed using Minitab to test for differences in parameters between the groups both at day 0 and day 2. Additionally, a repeated measures ANOVA was used to investigate changes within each of the three groups between the two time points. Statistical differences were reported for  $p < 0.05$ .

## 3.3 Results

### 3.3.1 Chuong and Fung Model

The lower and upper limits of parameter values were set at  $c \in [0, 10^{10}]$  and  $c_i \in [0, 10]$  for  $i = 1, \dots, 6$ . The final fitted parameter values were insensitive to initial parameter guesses. The mean value of the *error* was 0.085, which provided a reasonably good fit to data (Figure 3.1).

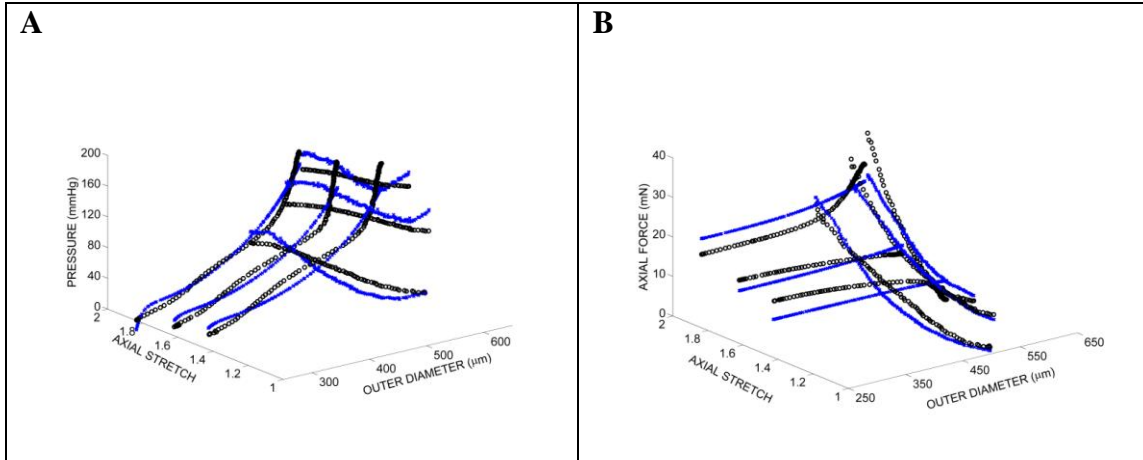


**Figure 3.1: The Chuong and Fung phenomenological model fits the data well.** Nonlinear regression techniques were used to calculate parameters for the Chuong and Fung model from the biaxial mechanical data. The results were then plotted with the data to visualize the goodness of fit. Panel A is from the pressure-diameter tests and shows pressure versus outer diameter and axial stretch while B shows axial force versus outer diameter and axial stretch from the force-length tests. Open black circles represent experimental data and blue x's represent model predictions. The fit visually looks reasonable and was confirmed by an error value of 0.085.

Statistically significant differences were observed between groups cultured at  $\lambda_z^* = 1.65$  and  $\lambda_z^* = 1.95$  for parameters  $c$ ,  $c_2$ ,  $c_4$  and  $c_6$  (Table 3.1). In addition,  $c$  and  $c_2$  differed across the groups cultured at  $\lambda_z^* = 1.80$  and  $\lambda_z^* = 1.95$  and  $c_4$  was different between 1.65 and 1.80. Repeated measures ANOVA showed differences all parameters in the  $\lambda_z^* = 1.65$  culture group between day 0 and day 2 and differences in  $c$ ,  $c_1$ ,  $c_2$ ,  $c_3$  and  $c_5$  for the  $\lambda_z^* = 1.80$  group between day 0 and day 2.

Table 3.1: Material parameters for the model of Chuong and Fung determined via non-linear regression. <sup>a</sup> indicates  $p < 0.05$  when comparing 1.65 and 1.95 on day 2, <sup>b</sup> indicates  $p < 0.05$  when comparing 1.80 and 1.95 on day 2, <sup>c</sup> indicates  $p < 0.05$  when comparing 1.65 and 1.80 on day 2, <sup>d</sup> indicates  $p < 0.05$  when comparing day 0 and day 2 the 1.65 group, and <sup>e</sup> indicates  $p < 0.05$  when comparing day 0 and day 2 for the 1.80 group.

	c (kPa)	c <sub>1</sub>	c <sub>2</sub>	c <sub>3</sub>	c <sub>4</sub>	c <sub>5</sub>	c <sub>6</sub>	error
Day 0, $\lambda_z^* = 1.65$								
053104_01	246	0.106	0.299	0.874	0.010	0.218	0.000	0.068
053104_02	140	0.077	0.433	1.158	0.011	0.278	0.000	0.067
061604_01	312	0.186	0.201	0.891	0.000	0.114	0.053	0.072
080304_02	319	0.055	0.219	0.339	0.000	0.065	0.000	0.076
100504_01	336	0.069	0.165	0.314	0.000	0.051	0.020	0.081
100504_02	333	0.073	0.175	0.285	0.000	0.036	0.027	0.099
	281	<sup>d</sup> 0.094	<sup>d</sup> 0.249	<sup>d</sup> 0.644	<sup>d</sup> 0.004	<sup>d</sup> 0.127	<sup>d</sup> 0.017	<sup>d</sup> 0.077
	76.4	0.048	0.102	0.376	0.005	0.099	0.021	0.012
Day 2, $\lambda_z^* = 1.65$								
053104_01	82.9	0.425	0.933	3.160	0.136	0.831	0.348	0.091
053104_02	57.9	0.287	0.915	2.718	0.092	0.728	0.229	0.092
061604_01	85.1	0.307	0.603	2.449	0.070	0.520	0.347	0.086
080304_02	62.6	0.142	0.878	1.758	0.025	0.447	0.000	0.098
100504_01	58.9	0.150	0.899	1.190	0.011	0.400	0.000	0.110
100504_02	56.3	0.379	0.744	1.518	0.062	0.286	0.188	0.093
	67.3	<sup>a,d</sup> 0.282	<sup>d</sup> 0.829	<sup>a,d</sup> 2.132	<sup>d</sup> 0.066	<sup>a,c,d</sup> 0.535	<sup>a,d</sup> 0.185	<sup>d</sup> 0.095
	13.1	0.116	0.129	0.762	0.045	0.206	0.157	0.008
Day 0, $\lambda_z^* = 1.8$								
060504_02	486	0.050	0.162	0.209	0.003	0.040	0.000	0.095
060804_02	991	0.047	0.093	0.088	0.000	0.002	0.001	0.078
092604_01	321	0.067	0.222	0.273	0.007	0.069	0.000	0.062
092604_02	126	0.113	0.665	2.310	0.044	0.624	0.044	0.068
100804_01	411	0.045	0.167	0.185	0.001	0.036	0.000	0.109
100804_02	295	0.049	0.204	0.195	0.000	0.039	0.005	0.083
	438	<sup>e</sup> 0.062	<sup>e</sup> 0.252	<sup>e</sup> 0.543	<sup>e</sup> 0.009	0.135	<sup>e</sup> 0.008	0.083
	296.7	0.026	0.207	0.868	0.017	0.241	0.018	0.017
Day 2, $\lambda_z^* = 1.8$								
060504_02	143	0.199	0.529	1.113	0.011	0.208	0.103	0.091
060804_02	185	0.175	0.458	0.742	0.020	0.148	0.057	0.080
092604_01	118	0.111	0.639	0.668	0.000	0.153	0.000	0.072
092604_02	37.4	0.216	1.275	3.706	0.019	0.908	0.080	0.074
100804_01	70.8	0.153	0.847	1.526	0.018	0.417	0.000	0.088
100804_02	54.3	0.196	0.750	0.620	0.000	0.063	0.000	0.089
	101	<sup>b,e</sup> 0.175	<sup>e</sup> 0.750	<sup>b,e</sup> 1.396	<sup>e</sup> 0.011	<sup>c</sup> 0.316	<sup>e</sup> 0.040	0.082
	57.0	0.038	0.294	1.183	0.009	0.313	0.046	0.008
Day 0, $\lambda_z^* = 1.95$								
052804_01	323	0.122	0.210	0.612	0.008	0.119	0.000	0.061
052804_02	457	0.017	0.269	0.338	0.011	0.161	0.000	0.060

061204_01	270	0.128	0.281	1.043	0.031	0.244	0.085	0.074
061204_02	397	0.070	0.182	0.272	0.000	0.039	0.010	0.081
093004_01	276	0.075	0.219	0.412	0.000	0.082	0.000	0.067
	345	0.082	0.232	0.535	0.010	0.129	0.019	0.069
	80.7	0.045	0.042	0.311	0.013	0.078	0.037	0.009
Day 2, $\lambda_z^*=1.95$								
052804_01	381	0.164	0.190	0.677	0.000	0.072	0.121	0.135
052804_02	132	0.154	0.469	1.788	0.000	0.000	0.183	0.078
061204_01	92.9	0.291	0.675	2.056	0.000	0.303	0.311	0.147
061204_02	332	0.086	0.227	0.272	0.000	0.000	0.064	0.095
093004_01	247	0.047	0.306	0.249	0.000	0.053	0.024	0.081
	237	<sup>a,b</sup> 0.148	0.373	<sup>a,b</sup> 1.008	0.000	<sup>a</sup> 0.086	<sup>a</sup> 0.141	0.107
	124.2	0.093	0.200	0.857	0.000	0.126	0.113	0.032

<sup>a</sup>Indicates  $p < 0.05$  when comparing 1.65 and 1.95 on day 2.

<sup>b</sup>Indicates  $p < 0.05$  when comparing 1.8 and 1.95 on day 2.

<sup>c</sup>Indicates  $p < 0.05$  when comparing 1.65 and 1.8 on day 2.

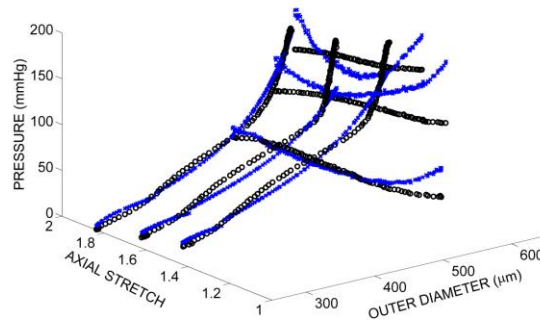
<sup>d</sup>Indicates  $p < 0.05$  when comparing day 0 and day 2 for the 1.65 group.

<sup>e</sup>Indicates  $p < 0.05$  when comparing day 0 and day 2 for the 1.8 group.

### 3.3.2 Four Fiber-Family Model

The lower and upper limits of the parameters were  $b$  and  $b_1^k \in [0, 10^5]$ ,  $b_2^k \in [10^{-4}, 10^5]$ , and  $\alpha \in [5^\circ, 85^\circ]$ . Final parameter values were insensitive to initial guesses. The model provided a good fit to data with a mean value of the  $error = 0.055$  (Figure 3.2). For all vessels at all culture times the fiber-family model provided a better fit than the Fung model (Table 3.2); this finding is consistent with Gleason *et al.* (131). A significant difference was seen for  $b_1^3$  at day 2 across the low ( $\lambda_z^* = 1.65$ ) and high ( $\lambda_z^* = 1.95$ ) stretch culture groups and across day 0 and day 2 for low stretch culture group. Additionally, the parameter  $b_2^2$  is significantly different across day 0 and day 2 for the  $\lambda_z^* = 1.80$  cultured vessels.

A



B

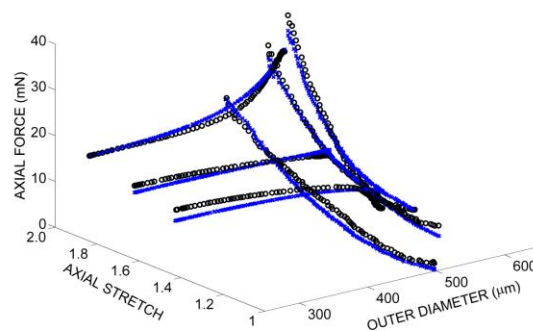


**Figure 3.2: The Four Fiber-Family Model has a better fit than the Chuong and Fung Model.** Nonlinear regression techniques were used to calculate parameters for the four fiber-family model from the biaxial mechanical data. The results were then plotted with the data to visualize the goodness of fit. Panel A is from the pressure-diameter tests and shows pressure versus outer diameter and axial stretch while B shows axial force versus outer diameter and axial stretch from the force-length tests. Open black circles represent experimental data and blue x's represent model predictions. The fit visually looks good and improvement over the Chuong and Fung model was confirmed by an error value of 0.055.

Table 3.2: Material parameters for the model of the four-fiber family model determined via non-linear regression. <sup>a</sup> indicates p<0.05 when comparing 1.65 and 1.95 on day 2, <sup>b</sup> indicates day 0 and day 2 the 1.65 group, <sup>c</sup> indicates p<0.05 when comparing day 0 and day 2 for the 1.80 group.

	b (kPa)	b <sub>1</sub> <sup>1</sup> (kPa)	b <sub>2</sub> <sup>1</sup>	b <sub>1</sub> <sup>2</sup> (kPa)	b <sub>2</sub> <sup>2</sup>	b <sub>1</sub> <sup>3</sup> (kPa)	b <sub>2</sub> <sup>3</sup>	α	error
Day 0, λ <sub>z</sub> *=1.65									
053104_01	18.3	9.1	0.076	28.5	0.036	0.0068	0.986	32.5	0.037
053104_02	16.2	1.7	0.102	28.1	0.047	0.0072	0.922	31.6	0.034
061604_01	39.5	0.5	0.828	12.7	0.096	0.0000	2.463	49.4	0.038
080304_02	11.6	4.9	0.052	36.1	0.015	0.0001	1.373	31.6	0.046
100504_01	6.4	8.2	0.041	28.3	0.010	0.0000	1.627	30.7	0.054
100504_02	7.2	8.0	0.043	32.1	0.009	0.0000	1.555	37.5	0.065
<i>Mean</i>	16.5	5.4	0.191	27.6	0.035	0.0023	1.488	35.5	0.046
<i>SD</i>	12.2	3.6	0.313	8.0	0.033	0.0036	0.559	7.2	0.012
Day 2, λ <sub>z</sub> *=1.65									
053104_01	20.3	6.7	0.389	33.7	0.094	0.4074	1.063	35.0	0.064
053104_02	11.9	3.0	0.274	25.4	0.089	0.2354	0.947	32.7	0.064
061604_01	12.5	3.6	0.246	28.7	0.036	0.0119	1.228	35.3	0.044
080304_02	13.9	1.9	0.152	39.4	0.046	0.0829	0.991	26.6	0.051
100504_01	2.7	4.7	0.079	40.7	0.028	0.0941	0.973	25.5	0.071
100504_02	9.1	7.7	0.214	32.1	0.037	0.2433	0.938	32.3	0.063
<i>Mean</i>	11.7	4.6	0.226	33.3	0.055	0.1792	1.023	31.2	0.059
<i>SD</i>	5.8	2.2	0.106	5.9	0.029	0.1441	0.110	4.2	0.010
Day 0, λ <sub>z</sub> *=1.8									
060504_02	13.0	7.8	0.037	37.1	0.024	0.0022	0.950	41.1	0.039
060804_02	16.8	15.7	0.001	42.2	0.023	0.0010	1.263	63.8	0.043
092604_01	11.1	8.1	0.035	35.2	0.028	0.0042	0.951	40.2	0.040
092604_02	19.4	5.8	0.064	37.6	0.060	0.2072	0.687	29.9	0.048
100804_01	8.2	7.8	0.025	38.4	0.000	0.0000	2.073	13.8	0.090
100804_02	3.9	6.8	0.016	34.5	0.015	0.0001	1.148	35.1	0.055
<i>Mean</i>	12.1	8.7	0.030	37.5	0.025	0.0358	1.179	37.3	0.053
<i>SD</i>	5.6	3.5	0.022	27.6	0.020	0.0840	0.481	16.4	0.019
Day 2, λ <sub>z</sub> *=1.8									
060504_02	17.4	4.2	0.197	39.9	0.063	0.0021	1.635	36.6	0.057
060804_02	25.9	0.6	0.591	38.5	0.065	0.0389	1.227	36.3	0.046
092604_01	17.1	0.5	0.216	39.0	0.096	0.0266	1.072	33.0	0.045
092604_02	3.6	9.9	0.036	43.3	0.076	0.1153	0.968	24.3	0.049
100804_01	3.3	10.6	0.023	44.4	0.019	0.0500	1.189	24.2	0.058
100804_02	4.8	7.6	0.054	39.0	0.035	0.0530	1.045	27.0	0.055
<i>Mean</i>	12.0	5.6	0.186	40.7	0.059	0.0476	1.189	30.2	0.052
<i>SD</i>	9.4	4.5	0.215	2.5	0.028	0.0380	0.238	5.8	0.006
Day 0, λ <sub>z</sub> *=1.95									

052804_01	26.9	6.5	0.203	21.1	0.052	0.0003	1.698	41.4	0.039
052804_02	3.0	5.7	0.000	60.4	0.000	0.0828	0.605	20.5	0.037
061204_01	21.0	6.4	0.144	26.7	0.041	0.0018	1.286	35.8	0.040
061204_02	17.7	3.3	0.136	32.5	0.028	0.0000	1.727	38.6	0.047
093004_01	17.0	2.2	0.136	25.3	0.033	0.0001	1.355	36.0	0.051
<i>Mean</i>	<i>17.1</i>	<i>4.8</i>	<i>0.124</i>	<i>33.2</i>	<i>0.031</i>	<i>0.0170</i>	<i>1.334</i>	<i>34.4</i>	<i>0.043</i>
<i>SD</i>	<i>8.8</i>	<i>1.9</i>	<i>0.075</i>	<i>15.7</i>	<i>0.020</i>	<i>0.0368</i>	<i>0.453</i>	<i>8.1</i>	<i>0.006</i>
Day 2, $\lambda_2^*=1.95$									
052804_01	22.96	3.37	0.358	21.8	0.085	0.0000	4.795	52.3	0.116
052804_02	16.38	2.63	0.117	43.2	0.097	0.0016	1.400	40.2	0.064
061204_01	12.37	2.75	0.230	41.3	0.045	0.0018	1.597	29.5	0.087
061204_02	6.39	7.78	0.021	40.0	0.055	0.0001	1.400	61.5	0.065
093004_01	2.63	4.49	0.020	42.3	0.026	0.0000	1.738	29.3	0.059
<i>Mean</i>	<i>12.15</i>	<i>4.20</i>	<i>0.149</i>	<i>37.7</i>	<i>0.062</i>	<i>0.0007</i>	<i>2.186</i>	<i>42.6</i>	<i>0.078</i>
<i>SD</i>	<i>8.04</i>	<i>2.13</i>	<i>0.145</i>	<i>9.0</i>	<i>0.029</i>	<i>0.0009</i>	<i>1.466</i>	<i>14.2</i>	<i>0.024</i>

a p<0.05 when comparing 1.65 and 1.95 on day 2

b p<0.05 when comparing day 0 and day 2 for group 1.65

c p<0.05 when comparing day 0 and day 2 for group 1.80

### 3.3.3 Microstructurally-Motivated Models: A Discrete Set of Fibers

We considered several variants of the rule of mixtures model, discussed separately below. In all cases, we prescribed the lower and upper limits of the parameters as  $b^e, b^m, b_1^m, b_1^{c1}$ , and  $b_1^{c2} \in [0, 10]$ ,  $b_2^m, b_2^{c1}$  and  $b_2^{c2} \in [10^{-5}, 10]$ , and  $\Omega^{c2} \Big|_h \in [5^\circ, 85^\circ]$ .

Final parameter values were insensitive to initial guesses. For the models that include material non-uniformity, unless otherwise noted, we prescribe the limits

$$(R^n)^e / R^n \in [0.8, 0.95], \quad (L^n)^e / L^n \in [0.8, 0.95], \quad (R^n)^m / R^n \in [0.95, 1.1],$$

$$(L^n)^m / L^n \in [0.95, 1.1], \quad \lambda^{c1} \Big|_h \in [1.0, 1.876].$$

Note that these limits force elastin to be in tension in the stress free state, collagen to be in compression in the stress free state, and

muscle may be in tension or compression. Rather than tabulating statistical differences in parameters for each variation of the rule of mixtures model, we instead present parameters from representative vessels from day 0 and day 2 at each culture stretch to allow comparison of the different model variations (Table 3.3).

ROM A: Uniform Four-Fiber: 1 Muscle Fiber, 3 Collagen Fibers (8 Material Parameters, 1 Structural Parameter): Consider the rule of mixtures equations proposed

above, but assume that the material is uniform; thus,  $(R^n)^e = (R^n)^c = (R^n)^m = R^n$  and  $(L_z^n)^e = (L_z^n)^c = (L_z^n)^m = L^n$ . For this case,  $\lambda_{rr}^e = \lambda_{rr}^c = \lambda_{rr}^m = \lambda_{rr}$ ,  $\lambda_{\theta\theta}^e = \lambda_{\theta\theta}^c = \lambda_{\theta\theta}^m = \lambda_{\theta\theta}$ ,  $\lambda_{zz}^e = \lambda_{zz}^c = \lambda_{zz}^m = \lambda_{zz}$

and

$$\hat{T}_{rr} = (\lambda_{rr})^2(\phi^e b^e + \phi^m b^m) \quad (3.42)$$

$$\begin{aligned} \hat{T}_{\theta\theta} = & (\lambda_{\theta\theta})^2(\phi^e b^e + \phi^m b^m) + \phi^m b_1^m ((\lambda_{\theta\theta})^2 - 1) \exp\{b_2^m ((\lambda_{\theta\theta})^2 - 1)^2\} \\ & + 2\phi^c b_1^c \sin^2(\alpha)[(\lambda^c)^2 - 1] \exp\{b_2 [(\lambda^c)^2 - 1]^2\} \end{aligned}$$

$$\begin{aligned} \hat{T}_{zz} = & (\lambda_{zz})^2(\phi^e b^e + \phi^c b^c + \phi^m b^m) + \phi^e b_1^e ((\lambda_{zz})^2 - 1) \exp\{b_2^e ((\lambda_{zz})^2 - 1)^2\} \\ & + 2\phi^c b_1^c \cos^2(\alpha)[(\lambda^c)^2 - 1] \exp\{b_2 [(\lambda^c)^2 - 1]^2\} \end{aligned}$$

Notice that this model reduces to the four fiber-family model described above; if

$$b = (\phi^e b^e + \phi^m b^m), \quad b_1^1 = \phi^m b_1^m, \quad b_2^1 = b_2^m, \quad b_1^2 = \phi^c b_1^c, \quad b_2^2 = b_2^c, \quad b_1^3 = \phi^e b_1^e, \quad \text{and} \quad b_2^3 = b_2^e,$$

then equations 3.43 are identical to equations 3.16, determined from a four fiber-family

model. If we let  $b^e = b/(2\phi^e)$  and  $b^m = b/(2\phi^m)$ , then the identical fits as above with the

four fiber-family model will be achieved. The mean *error* for the four vessels considered

was 0.055, which was equal to the mean of all vessels for the four fiber-family model;

thus, these four vessels are considered representative.

Table 3.3: Material parameters representative data for the various versions of the rule-of-mixtures constitutive model

	$b^e$	$b^m$	$b_1^m$		$b_1^{cz}$	$b_1^{ca}$			$\omega^{c2}$	$R^e$	$L_z^e$	$R^m$	$L_z^m$	$\lambda^c$	<i>error</i>	<i>penalty</i>
	(kPa)	(kPa)	(kPa)	$b_2^m$	(kPa)	$b_2^{cz}$	(kPa)	$b_2^{ca}$								
Day 0, $\lambda_z^*=1.65$ (061604_01)																
ROM A																
(no																
pen)	215	163	165	0.034	96.2	0.107	0.0	1.895	63.2	--	--	--	--	--	0.041	--
ROM A	380	158	0.0	0.000	59.4	0.152	1.09	0.977	65.6	--	--	--	--	--	0.051	0.002
ROM B	380	157	0.0	0.008	1983	1.171	102	5.267	65.2	0.96	0.80	1.10	0.99	1.273	0.051	0.002
ROM C	505	170	0.0	0.000	389	4.331	--	--	60.0	1.00	0.80	1.10	0.95	1.222	0.081	0.006
Fiber	282	130	45.1	0.000	2345	0.751	240	3.436	64.7	0.92	0.80	1.10	0.95	1.303	0.056	0.002
Day 2, $\lambda_z^*=1.65$ (061604_01)																
ROM A																
(no																
pen)	104	69.3	40.5	0.246	192	0.036	0.1	1.228	35.3	--	--	--	--	--	0.044	--
ROM A	149	16.7	37.3	0.060	115	0.136	5.4	0.570	49.4	--	--	--	--	--	0.089	0.001
ROM B	153	28.6	6.7	0.702	288	0.153	8.9	0.438	47.7	1.00	0.80	1.10	1.10	1.876	0.086	0.001
ROM C	149	0.0	0.0	2.341	59.7	0.361	--	--	36.4	1.00	0.80	1.10	1.09	1.760	0.129	0.006
Fiber	61.3	12.7	88.9	0.022	1700	0.548	403	0.985	46.8	0.90	0.80	1.10	0.95	1.433	0.101	0.008
Day 2, $\lambda_z^*=1.80$ (100804_02)																
ROM A																
(no																
pen)	37.3	24.3	86.1	0.052	262	0.034	0.4	1.046	27.0	--	--	--	--	--	0.055	--
ROM A	105	9.2	13.3	0.158	107	0.205	11.5	0.446	37.8	--	--	--	--	--	0.088	0.001
ROM B	105	35.8	15.2	0.302	337	0.194	12.0	0.401	39.1	1.00	0.81	1.10	1.10	1.876	0.088	0.001
ROM C	113	0.0	10.5	0.401	59.7	0.361	--	--	36.4	1.00	0.80	1.10	1.09	1.760	0.129	0.006
Fiber	73.8	2.6	78.0	0.000	1878	0.967	407	1.248	39.8	0.95	0.80	1.10	0.95	1.406	0.113	0.010
Day 2, $\lambda_z^*=1.95$ (052804_02)																
ROM A																
(no																
pen)	137	91.0	29.2	0.117	288	0.097	0.0	1.400	40.2	--	--	--	--	--	0.064	--
ROM A	134	83.1	0.0	0.000	225	0.153	6.8	0.348	53.3	--	--	--	--	--	0.071	0.000
ROM B	208	38.3	0.0	0.000	725	0.151	8.3	0.368	55.3	1.00	0.80	1.07	0.95	1.876	0.070	0.000
ROM C	137	69.6	0.3	0.888	116	0.261	--	--	27.8	0.95	0.80	1.10	0.95	1.783	0.122	0.009
Fiber	127	25.6	1.3	0.576	1730	0.352	372	0.244	44.1	0.95	0.80	1.10	0.95	1.584	0.087	0.000

We also enforced the constraints 3.40 and 3.41 via the penalty method for this rule of mixtures model. The mean value of the *error* was 0.084 for the four vessels considered (Table 3.3), which provided a worse fit than the *ROM A* without penalties (i.e., the four fiber-family model), but equally well as the Fung model; these findings are consistent across all vessels. The average *penalty* for these four vessels was 0.001; thus, the penalty criteria were nearly, but not completely, satisfied. Figure 3.3 is a stress-stretch plot of individual components as well as the total stress for a representative vessel illustrating that the model does indeed capture physiologic loading scenarios which are enforced by the penalty system.

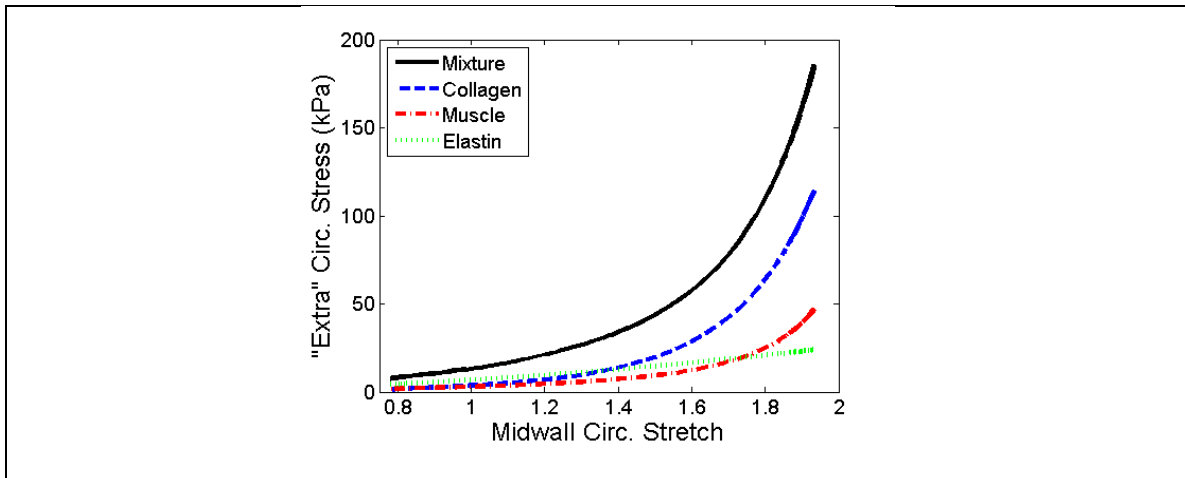


**Figure 3.3: The rule-of-mixtures model captures the individual components' physiological contributions of the total stress.** The circumferential stress-stretch behavior of the each component was calculated and plotted with the resulting graphing showing that the components contributed as expected with elastin bearing the majority of the load at low loading conditions and collagen at high loads.

ROM B. Non-uniform Four-Fiber: 1 Muscle Fiber, 3 Collagen Fibers (8 Material Parameters, 7 Structural Parameter): Next, consider the same functional form of the constitutive equation as in (*ROM A*), but let the material be non-uniform. That is, let  $(R^n)^e / R^n$ ,  $(R^n)^m / R^n$ ,  $(L_z^n)^e / L^n$ ,  $(L_z^n)^m / L^n$ ,  $\lambda_1^c|_h = \lambda_2^c|_h$ , and  $\omega^{c2}|_h$  be free (structural) that may be determined via non-linear regression along with the eight material parameters. Note that we set  $\omega^{c1}|_h = 0^\circ$  and  $\lambda_1^c|_h = \lambda_2^c|_h$ . First, we let the upper and lower limits for the structural parameters of elastin be  $(R^n)^e / R^n \in [0.8, 1.0]$  and  $(L^n)^e / L^n \in [0.8, 1.0]$ ; these regressions are referred to as *ROM B1*. The mean value of the *error* was 0.083 for the four vessels; the average *penalty* was 0.001. Thus, adding material non-uniformity provided little to no increase in the goodness of fit (see Figure 3.4 A&B). Notice, too, that several of the structural parameters obtained via regression were at, or very near, the upper or lower limits prescribed for the regression. Next, we set the upper and lower limits for the structural parameters of elastin as  $(R^n)^e / R^n \in [0.8, 0.95]$  and  $(L^n)^e / L^n \in [0.8, 0.95]$  (denoted *ROM B2*); thus, elastin is required to be in tension in the mixture reference state. The mean value of the *error* equaled 0.100 for the four vessels, and the average *penalty* was 0.002. Thus, by simply requiring that elastin be in tension, there was a significant reduction in the goodness of fit. Notice, too, that whereas  $\lambda_1^c|_h$  was at its upper limit of 1.876 for all four vessels in *ROM B1*, the average value for  $\lambda_1^c|_h$  was 1.46 in *ROM B2*.

ROM C. Non-uniform Four-Fiber: 1 Muscle Fiber, 3 Collagen Fibers (6 Material Parameters, 6 Structural Parameters): Here we consider the same non-uniform model at *ROM B*, but let  $b_1^{c1} = b_1^{c2}$  and  $b_2^{c1} = b_2^{c2}$ ; that is, we let the material properties of the fibers

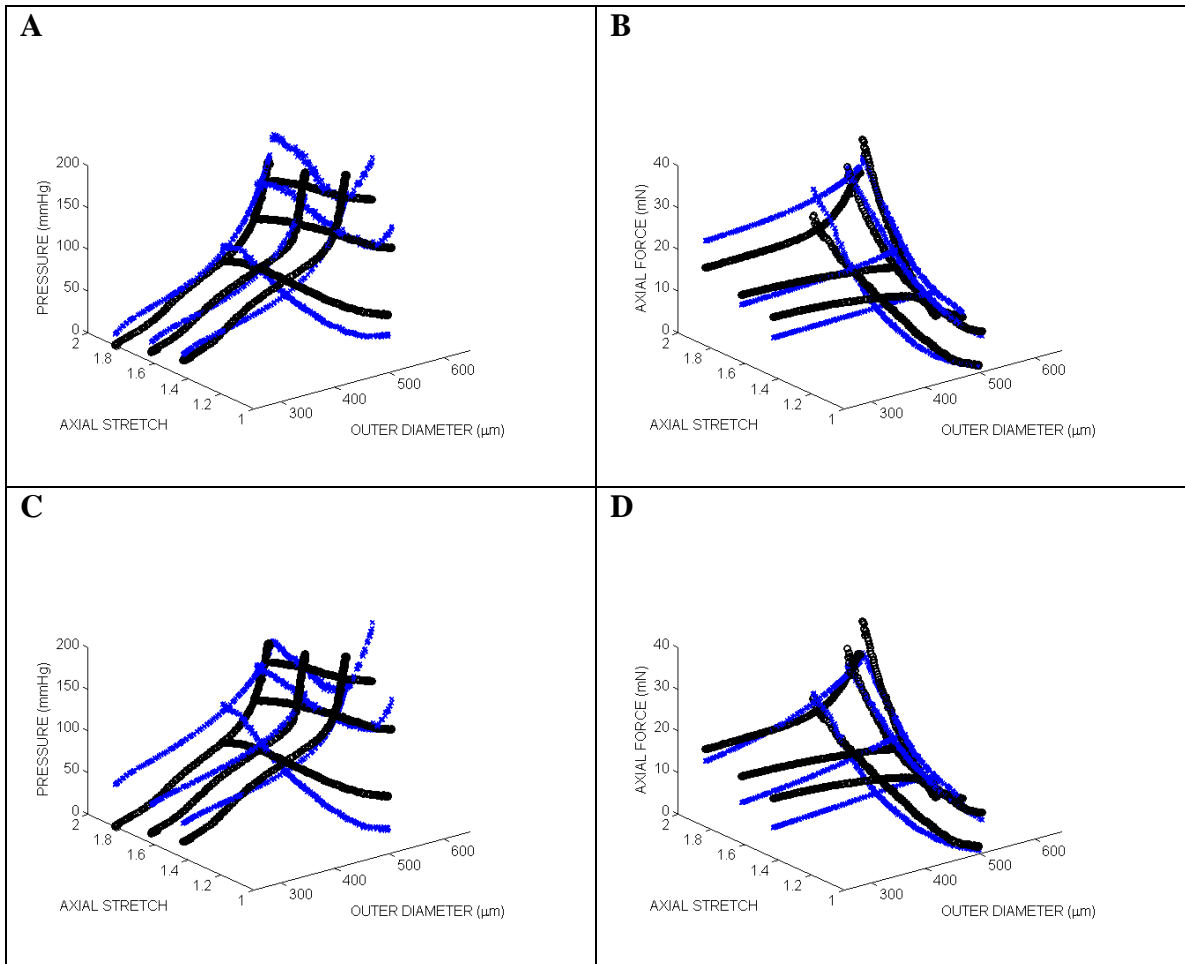


**Figure 3.4: Requiring collagen fibers to have the same material properties in all orientations decreases the goodness of fit.** Nonlinear regression techniques were used to calculate parameters for different variations on the rule-of-mixtures models. The results were then plotted with the data to visualize the goodness of fit. Open black circles represent experimental data and blue x's represent model predictions. Panels A and B show results of the pressure-diameter and force-length tests respectively for ROM B1. Panels C and D show the results for the variation ROM C. ROM C is the same as ROM B1 except that the material properties of the collagen fibers in the axial and off-axis are required to be the same. This constrain reduces the goodness of fit as observed both visually and with error values of 0.083 and 0.152 for ROM B and C respectively.

oriented in the  $\omega^{c1}|_h$  direction equal those oriented in the  $\pm\omega^{c2}|_h$  direction. The mean value of the *error* was 0.152 for the four vessels considered, and the average *penalty* was 0.006. Thus, requiring the collagen fibers in the axial and off-axis directions to have the same material parameters significantly reduced the goodness of fit and satisfaction of the penalty criteria (see Figure 3.4 C&D).

### 3.3.4 Rule of Mixtures Model: Distributed Fibers

For the fiber distribution model, let  $\bar{R}^e / R^n$ ,  $\bar{R}^m / R^n$ ,  $\bar{L}^e / L^n$ ,  $\bar{L}^m / L^n$ ,  $\bar{\lambda}^{c1}|_h = \bar{\lambda}^{c2}|_h$ , and  $\bar{\omega}^{c2}|_h$  be free (structural) parameters that may be determined via non-linear regression along with the eight material parameters and let  $b_1^{c1} \neq b_1^{c2}$  and  $b_2^{c1} \neq b_2^{c2}$ . We used the values from *ROM B2* as initial guesses for this fiber distribution. The mean value of the *error* equaled 0.098 for the four vessels, and the average *penalty* was 0.005. The addition of a distribution of fibers did not appear to greatly change the goodness of fit of the model as the error values for the model were similar to *ROM B2*, which had the same number of free parameters. In this analysis, we fixed the width of the distribution functions by prescribing  $\sigma_p$  and  $\Delta\Gamma$  for the collagen distribution and  $\Delta R^j$  and  $\Delta L^j$  for the elastin and muscle distribution. These parameters, however, could be adjusted to improve the goodness of fit. Ultimately, however, the utility of such microstructurally motivated model is to quantify the fiber distribution directly from data (c.f., (132, 133)), rather than prescribing the fiber distribution functions, as done in this aim.

## 3.4 Discussion

Mechanotransduction of mechanical signals to cellular responses plays a central role in maintaining tissue homeostasis, as well as the development of numerous

pathologies. Fundamental to quantifying a mechanosensitive biological response of a cell within a tissue is the quantification of the mechanical environment in a local neighborhood around that cell. When a good approximation of the local mechanical environment (e.g., in terms of stress and strain) is made, only then can a correlation be rightfully made between local mechanical stimuli and local biological response. Thus, there is a pressing need to better quantify the local mechanical environment in blood vessels and how this local mechanical environment evolves as the tissue grows and remodels. Towards this end, we have quantified material and structural parameters for several constitutive models for mouse carotid arteries exposed to altered axial extension in organ culture.

We found that the model of Chuong and Fung (122) provided a good fit to data. However, motivated by the fact that blood vessels have smooth muscle cells oriented circumferentially and collagen fibers oriented axially and distributed at off-axis angles, we considered a microstructurally-motivated four fiber-family model. In all cases the four fiber model provided a better fit to data than did the model of Chuong and Fung. Indeed, even two fiber-family models, with fibers oriented at  $\pm\alpha$ , have been shown to provide good agreement with data (118). A four fiber-family model has been shown to provide a better fit to data from mouse vessels than a two fiber-family and a slightly better fit than a three fiber-family model (134), at the cost of additional material parameters. For the sake of improving the fit, the cost of additional parameters when using a four fiber-family over a two or three fiber-family model may not be well justified. However, when attempting to ascribe physical meaning to each fiber-family (e.g., by allowing one fiber-family to represent smooth muscle, another to represent axially oriented collagen, and others to

represent collagen oriented off axis), the number of fiber families should be chosen based on observations of the microstructure.

Although our goal in considering a four fiber-family model was to ascribe each fiber family to a key structural constituent observed via microscopy, we found that simply performing non-linear regression did not ensure that each fiber family (i.e., structural constituent) contributed significantly to the mechanical response. Rather, it was necessary to employ a penalty method to ensure that each constituent had a significant contribution. Since the classic paper by Roach and Burton (127) it has been thought that elastin plays a key role in the mechanical behavior over low loads and collagen dominates the mechanical behavior over high loads. Brankov et al. (116) also suggests that elastin is under a higher strain *in vivo* than collagen. Based on these observations, we imposed penalties and upper and lower limits on structural parameters that enforced these general observations. Although these penalties reduced the goodness of fit compared to the non-penalized fits, the overall goodness of fit with the penalties included was, in many cases, still equal to the fits obtained via the model of Chuong and Fung; thus, fits that required each constituent be structurally significant still produced a model with reasonable agreement with data. We also submit that such criteria are critical when assigning physical meaning to material and structural parameters.

We also found that allowing the stress free states (or homeostatic stretches) of each constituent to be structural parameters that are solved via regression did not significantly improve model fits. Importantly, however, although this material non-uniformity did not play a significant role in improving the fit of data to our models, tracking the evolution of stress-free states of individual constituents plays a key role in

quantifying microstructurally motivated models for tissue growth and remodeling (130, 135, 136).

Limitations of the constitutive modeling originate from the adopted assumptions. First, we modeled the mouse carotid artery as a homogeneous mixture. It is clear, however, that these vessels have a thin intima consisting of an endothelial cell monolayer on a basement membrane, a media consisting of smooth muscle, elastin, and collagen, and an adventitia dominated by fibroblasts and collagen; thus vessels are heterogeneous. Unfortunately, sufficient data is not available on the distribution of the key structural constituents and how the content and organization of these constituents evolve during remodeling to various changes stimuli. Although these data are not currently available, as data becomes available, the structurally motivated models are capable of accounting for vessel heterogeneity by incorporating experimentally observable spatial and temporal variations in structural parameters. Second, because the opening angle was not measured in Gleason et al., which was the data set used for the model development, (120) we assumed that the strain was uniform across the wall in the *in vivo* configuration; this assumption may be tested as data on the evolution of opening angle during remodeling become available. Third, and more fundamental, is the assumption that the overall stress is given as the sum of the stresses borne by the individual constituents in the fiber-family and rule of mixtures models, thus, excluding the contribution of constituent-to-constituent interactions. Ultimately, incorporation of such interactions will provide important insights toward mechano-biology; however, sufficient data are not yet available to motivate reasonable functional forms for such constitutive equations. Finally, we model the tissue as a constrained mixture; thus, each constituent is constrained to follow the

motion of the tissue on the whole; this need not be (and likely is not) the case. To overcome all of these limitations, there is a need for data that quantifies the spatial and temporal variations of constituent content and organization with remodeling and mechanical loading.

In conclusion, we have identified material (and structural) parameters for phenomenological and microstructural models of mouse common carotid arteries exposed to altered axial extension, *ex vivo*. We have identified models with parameters that provide good agreement with data, while ascribing physical and microstructural meaning to fiber families that are associated with the underlying microstructural content and organization of the tissue. Although we made several assumptions (e.g., homogeneity, uniform strain *in vivo*, etc.), as data becomes available these assumptions may be relaxed. Through the application of new imaging strategies, experimental quantification of spatial and temporal variations in microstructural parameters promises to yield models with broader capabilities to predict the evolution of mechanical behavior during growth and remodeling associated with physiological and pathophysiological processes.

## CHAPTER 4

### **Specific Aim 2: Characterize the mechanical behavior, microstructure, protease activity, and ECM gene expression of arteries from an HIV-1 transgenic mouse model.**

#### **4.1 Introduction**

Due to the success of highly active antiretroviral therapy (HAART), HIV infection has been transformed from a terminal diagnosis to a manageable chronic disease. HIV patients, however, have an elevated incidence of dyslipidemia, lipodystrophy, insulin resistance, diabetes mellitus, and cardiovascular disease (CVD); the latter includes an elevated risk of myocardial infarction (2-4) and higher prevalence of atherosclerotic lesions (5-7), as well as increases in markers of subclinical atherosclerosis including increased carotid artery intima-media thickness (8-13), increased arterial stiffness (8, 14, 15) and impaired flow-mediated brachial artery dilation, an indicator of endothelial dysfunction (8, 9, 14, 16-20).

HAART drugs, particularly protease inhibitors (137-141), but also other drug classes (16, 142-144), are often implicated as a mediator of early on-set cardiovascular disease. Data, however, also suggests that HIV, independent of HAART, can induce CVD (9, 13, 145). Specifically, carotid intima-media thickness (c-IMT) and impaired flow mediated dilation (FMD) have been observed in HIV positive, HAART naïve patients (9). Similarly, exposure of endothelial cells *in vitro* to various HIV proteins decreases nitric oxide synthase, increases cell adhesion molecules, endothelial permeability, cell proliferation, cytokine signals, apoptosis, and oxidative stress (81, 84, 85); these mechanisms are all implicated in the development of atherosclerosis. Thus,

there remains a need to investigate the effect of the viral proteins, independent of viral infection and HAART, on the vasculature in an *in vivo* model.

The purpose of this aim is to characterize the effect of HIV proteins on mechanical behavior, microstructure, protease activity, and ECM gene expression of arteries using an HIV-1 transgenic mouse model. The NL4-3Δ *gag/pol* transgenic mouse (HIV-Tg) is a non-infectious model with a 7.4 kb transgene that contains the genetic sequence for the HIV-1 proteins *env*, *tat*, *nef*, *rev*, *vif*, *vpr*, and *vpu*, but lacks the *gag* and *pol* genes and is thus unable to replicate (146). The clinical markers of atherosclerosis, arterial stiffening and thickening, will be measured through biaxial mechanical tests, histology, and confocal imaging. Additional markers of vascular remodeling quantified were collagen and elastin content and cathepsin activity. Vascular remodeling due to synthesis, proteolytic degradation, and remodeling of key structural components of the arterial wall (e.g., elastin and collagen) lead to changes the biomechanical properties of the artery (e.g., arterial stiffness). Specifically, ECM content differs in healthy and atherosclerotic vessels and the cathepsins family of proteases is unregulated in diseased vessels as well. (147-149).

## **4.2 Methods**

### **4.2.1 HIV-Transgenic Mouse Model**

The NL4-3Δ *gag/pol* transgenic mouse strain was used. 10-12 week old male hemizygous and wild-type littermates (FVB/N) were used. Homozygous HIV-1 Tg mice are smaller at birth, have decreased food intake compared to wild-type mice, and usually die within 40 days postnatal; thus, homozygous mice were not included in this study (146). The hemizygous mice appear normal at birth but develop signs of disease,

specifically renal failure known as HIV-associated nephropathy (146). All animals work was conducted under the regulation of Georgia Institute of Technology's and Atlanta VA Medical Center's Institutional Animal Care and Use Committee (IACUC).

#### **4.2.2 Common Carotid Artery and Aorta Preparation**

Mice were euthanized with CO<sub>2</sub> and the right and left common carotids arteries and the aorta were removed. Briefly, the ventral side of the mouse was cleaned with alcohol and an incision was made from the groin to jaw. Tissue was dissected and removed to expose both common carotid arteries and the aorta from the aortic arch to the iliac bifurcation. Right and left common carotid arteries and the aorta were excised and cleaned free of any remaining perivascular tissue.

#### **4.2.3 Biomechanical Measurements: Cylindrical Biaxial Testing, Arterial Stiffness, and Opening Angle**

Cylindrical Biaxial Testing: Cylindrical biaxial biomechanical tests of the arteries were performed as previously described to characterize the biomechanical behavior of these arteries (150). During the experiment the excised common carotid arteries and aortas were maintained in culture medium [Dulbecco's modified Eagles medium (DMEM, Invitrogen, Inc.) containing 4.5g/L glucose and sodium pyruvate and without L-glutamine and phenol red]. For the aorta, branches within the suprarenal region were ligated using 10-0 silk sutures, and 8-0 suture was used to mount the arteries on two glass cannulae on a custom biaxial mechanical testing device (150). The vessel and cannulae were suspended in a bath on the device, which was filled with media containing sodium nitroprusside (SNP) to ensure that the arteries were fully dilated during the mechanical tests. Perfusion of the vessel through the two glass cannulae allows for careful control of

the luminal pressure. The mounting cannulae are attached to computer controlled actuators that allow for precise control of the vessel length and a force transducer vessel during testing. Thus, this computer-controlled device has the capability of maintaining precise luminal pressure and axial length of the vessel, while recording the outer diameter and axial force during the testing.

Following preconditioning, fixed length pressure-diameter tests and fixed pressure force-length tests were performed under quasistatic loading conditions (150). During the pressure-diameter tests, vessels were inflated to 160 mmHg at a series of fixed axial stretches of  $\lambda=1.3, 1.4, 1.5, 1.6, 1.7, 1.8,$  and  $1.9$  ( $\lambda$  is the loaded vessel length/unloaded vessel length), with three loading/unloading cycles for each axial stretch. During the force-length tests the vessels were held at constant pressures of 0, 40, 60, 80, 100, and 120 mmHg and stretched to an axial load of 1 gram (for common carotid arteries) or 3 grams (for the aorta) with three loading/unloading cycles at each pressure.

Arterial Stiffness: The Peterson's modulus ( $E_p$ ), a common measure of arterial stiffness, was calculated as the slope of the pressure-outer diameter curve ( $\Delta P/\Delta D$ ) at a given pressure normalized to the outer diameter ( $D$ ) at that pressure; namely,  $E_p = \Delta P/(\Delta D/D)$ .

Opening Angles: Following testing or microscopy imaging (described below), ring sectors were cut from the arteries to obtain their stress free configuration. Opening angle measurements were taken to quantify the residual stress in the unloaded configuration (151). A 14% gelatin mixture was injected into the vessel and allowed to solidify. Then the artery was cut into a series of segments and placed in phosphate buffered saline (PBS) (152). A single radial cut was then made in each of these segments

and the open sectors were allowed to equilibrate for 30 minutes. A dissection microscope and camera were used to take pictures of the cross-section of the sectors and an image processing script in MatLab (MathWorks) was used to find the vessel wall area  $A$ , inner arc length  $L_i$ , and outer arc length  $L_o$ . The opening angle can then be calculated using the following equations.

$$A = \frac{H(L_o + L_i)}{2} \quad \theta = \frac{L_o + L_i}{2H} \quad (4.1)$$

Note, that  $\theta$  is the half of the central angle of the stress free sector; thus, the traditional opening angle is  $180 - \theta$  (151).

#### 4.2.4 Intima-Media Thickness Measurements

The vessel wall thickness was quantified by two methods: confocal imaging of live arteries mounted on the biomechanical testing device was used to quantify the intima-media thickness and adventitia thickness, and standard histology of fixed, sectioned, and stained vessels was used as an additional measure to quantify intima-media thickness.

Confocal Microscopy: The custom biomechanical testing device fits on a LSM 510 META inverted confocal microscope (Zeiss) to visualize the microstructure across the entire wall of live, unfixed mouse arteries (150). Collagen and elastin were imaged using their autofluorescent properties. The isolated vessel, maintained in PBS, was excited with a 800 nm two-photon laser, collagen was visualized by detecting its second harmonic generation around 400 nm, and elastin emissions were detected by setting the META filter to a 480-560 nm bandpass configuration (153). Using the device, z-stacks were collected at a variety of loading conditions including physiologic pressure and stretch. Orthogonal views of these z-stacks were then used to calculate the thickness of

the adventitial layer (collagen images) and intima-media layer (elastin images) of the arteries. Note that while the media is thought to contain some collagen, the amount and fibrils in the mouse media is too small to detect using the established confocal methods; thus the images containing only collagen or only elastin are considered to be the adventia and media layers respectively.

Histology: Vessels were fixed in their unloaded state in 10% buffered formalin, immersed in 30% sucrose overnight, embedded in optimal cutting temperature medium, and frozen. The arteries were cut into 7  $\mu\text{m}$  thick slices, mounted on slides, and stained with hematoxylin and eosin. The images were analyzed using ImageJ (NIH) to quantify the thickness of the arteries.

#### **4.2.5 Other Microstructure Analysis**

Collagen Fiber Analysis: The confocal microscopy images were also used to quantify the angular distribution of fibers within the arterial wall. The angles of fibers in each slice of the z-stack were quantified using a fast Fourier series algorithm program in a MATLAB script as established previously. (154-156) Briefly, the initial processing included a low-pass filter, conversion to binary, and windowing with a 2D Tukey window. A fast Fourier transform of the preprocessed image generated a power spectrum. A histogram of the frequency of intensities between -90 and 90 degrees with 4 degree bins was created from the spectrum. This process was repeated for each slice within the z-stack to generate a distribution of fibers across the wall for each vessel. The thickness and relative wall location were normalized and the corresponding distributions in each vessel were averaged to create a surface which represented the fiber angle distributions through the wall for both groups.

Quantification of elastin breaks: Additional slides were prepared using the same protocols for the histological thickness measurements. These slides were stained with Verhoeff-Van Gieson elastin stain, which specifically stains the elastin fibers black. The Verhoeff-Van Gieson slides were used to quantify potential elastin breaks in the lamellae

#### **4.2.6 Collagen and Elastin Content Measurements**

Pairs of carotid arteries from a single mouse or a single suprarenal aorta were dried in a vacuum oven at 37°C for 2 days. The dry weight of the vessels was recorded for normalizing to protein content. In the samples for collagen analysis, the collagen was solublized by placing the vessel in 0.5 mL of 0.5 M acetic acid containing pepsin in a 1:3 ratio of enzyme to tissue weight. The tubes containing the vessels were placed in a 37°C water bath for 48 hours with occasional agitation. Sirius red dye solution (0.3 mg/mL direct 80 Sirius red in 0.5 M acetic acid) was added to each tube and the solution was incubated at room temperature for 30 min. The supernatant was removed following centrifuging, and 0.1 M HCl was added, and the sample was centrifuged again. Finally, 0.5 M NaOH was added and the samples were vortexed to release the dye. The collagen content was then determined by measuring the absorbance of each sample at a wavelength of 540 nm.

The elastin content of the arteries was quantified using the Fastin Elastin Assay (Biocolor). First, elastin from the dried arteries was solublized by boiling in 0.25 M oxalic acid for 5 hours. Elastin in the sample solutions was then precipitated using the manufacturer's precipitating agent. After 10 minutes the samples were centrifuged, and the supernatant was removed. The Fastin dye solution was then added to the tubes and allowed to bind with the precipitated elastin for 90 minutes. The samples were

centrifuged again, and the unbound dye in the supernatant was removed. A dye dissociating solution was added to release the dye from the walls of the tube. The absorbance at 513 nm of the resulting solution was used to quantify the elastin content of the arteries.

#### **4.2.7 Cathepsin Expression and Activity Measurements**

Gelatin zymography: Cathepsin activity was quantified by gelatin zymography. Excised suprarenal aortas or two pairs of carotids (4 arteries) were stored on ice and placed in 50  $\mu$ l of lysis buffer (20 mM Tris-HCl [pH 7.5], 5 mM ethyleneglycoltetraacetic acid [EGTA], 150 mM NaCl, 20 mM  $\beta$ -glycerol phosphate, 10 mM NaF, 1 mM sodium orthovanadate, 1% Triton X-100, and 0.1% Tween 20) with 0.1 mM leupeptin freshly added to stabilize enzymes during electrophoresis. The arteries were homogenized using disposable sample grinders (GE Healthcare), and protein concentrations were obtained by the bisinchoninic acid (BCA) assay (Pierce). Cathepsin zymography was performed as described previously (157, 158). 5X non-reducing loading buffer (0.05% bromophenol blue, 10% SDS, 1.5 M Tris, 50% glycerol) was added to all samples prior to loading. Equal amounts of protein were resolved by 12.5% SDS-polyacrylamide gels containing 0.2% gelatin at 4°C. Gels were removed and enzymes renatured in 65 mM Tris buffer, pH 7.4 with 20% glycerol for 3 washes at 10 minutes each. Gels were then incubated in activity buffer (0.1 M sodium phosphate buffer, pH 6.0, 1 mM EDTA, and 2 mM DTT freshly added) for 30 minutes at room temperature. Then this activity buffer was exchanged for fresh activity buffer and incubated for 18-24 hours (overnight) incubation at 37°C. The gels were rinsed twice with deionized water and incubated for one hour in Coomassie stain (10% acetic acid, 25% isopropanol, 4.5% Coomassie Blue) followed by

destaining (10% isopropanol and 10% acetic acid ). Gels were scanned using an Imagequant 4010 (GE Healthcare). Images were inverted in Adobe Photoshop and densitometry performed using Scion Image (Scion Corporation).

#### **4.2.8 Statistical Analysis**

All data presented is mean plus or minus standard error mean ( $\pm$ SEM). Means between groups were compared using unpaired student t tests with significance at  $p < 0.05$ . All statistics were performed in either Excel (Microsoft) or GraphPad Prism (GraphPad software).

## **4.2 Results**

### **4.2.1 Mice expressing HIV proteins exhibit increased arterial stiffness and altered biomechanics**

Cylindrical biaxial biomechanical testing revealed that the common carotid arteries from the HIV Tg mice have a smaller diameter for a given pressure, with statistically significant differences at pressures between 60 and 100 mm Hg ( $p < 0.05$ ) for the *in vivo* axial stretch of  $\lambda = 1.7$  (Figure 4.1 A) and subphysiological stretch of  $\lambda = 1.4$  as well (Figure A.1 in appendix). No differences were observed in aortic diameters (Figure 4.1 C). Peterson's modulus, a common measure of arterial stiffness, revealed that the HIV Tg arteries exhibited elevated arterial stiffness, compared to wildtype arteries. Statistical differences were seen at pressures for common carotid arteries at the *in vivo* axial stretch ( $\lambda = 1.7$ ; Figure 4.1 B), as well as at subphysiological ( $\lambda = 1.4$ ) and superphysiological ( $\lambda = 1.9$ ) stretches (Figure A.2 in appendix). Similarly, statistical differences were seen in aortas of HIV Tg at pressures of 20 to 40 mm Hg for the *in vivo*

axial stretch ( $\lambda=1.7$ ) (Figure 4.1 D), and at subphysiological ( $\lambda=1.4$ ) and superphysiological ( $\lambda=1.9$ ) stretches (Figure A.3 in appendix).

No differences were observed in the axial force during fixed length pressure-diameter tests over physiologically-relevant loads; significant differences were observed under very low loads (Figure A.4 A in appendix). No significant differences were

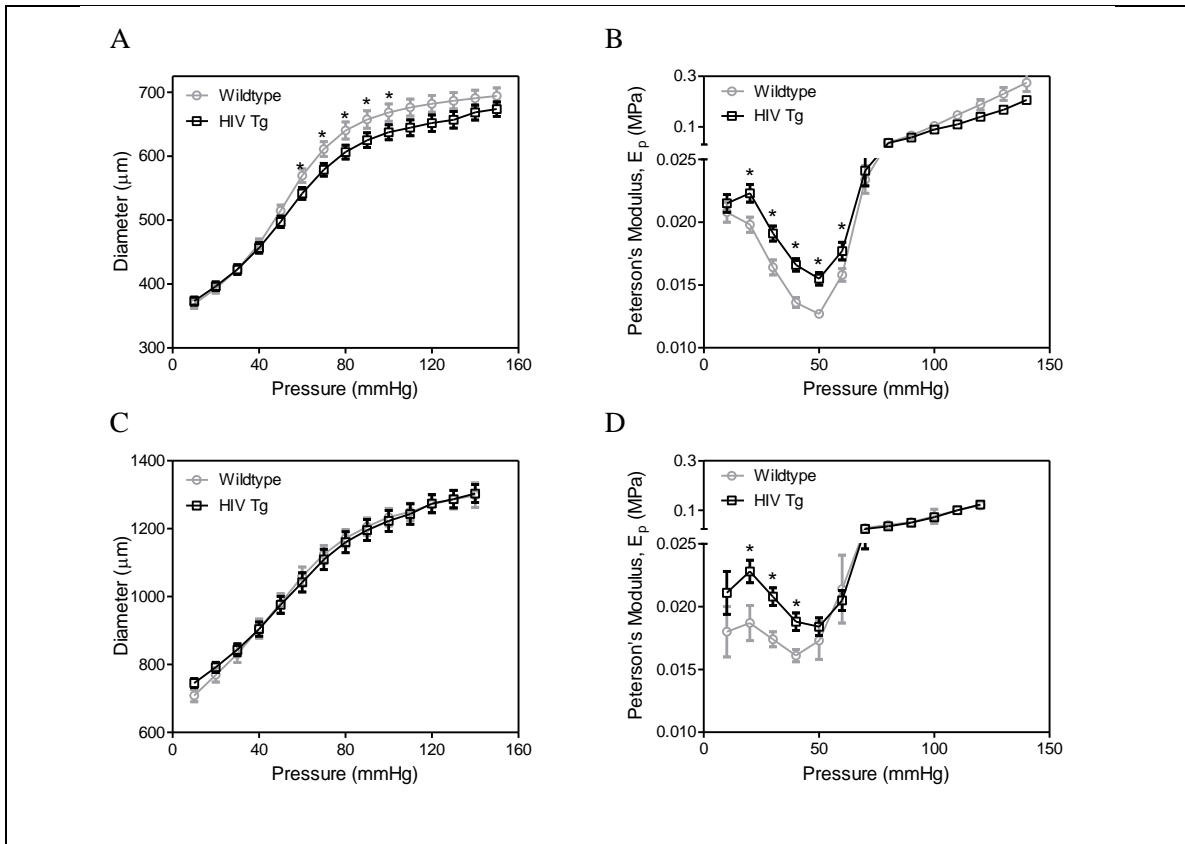
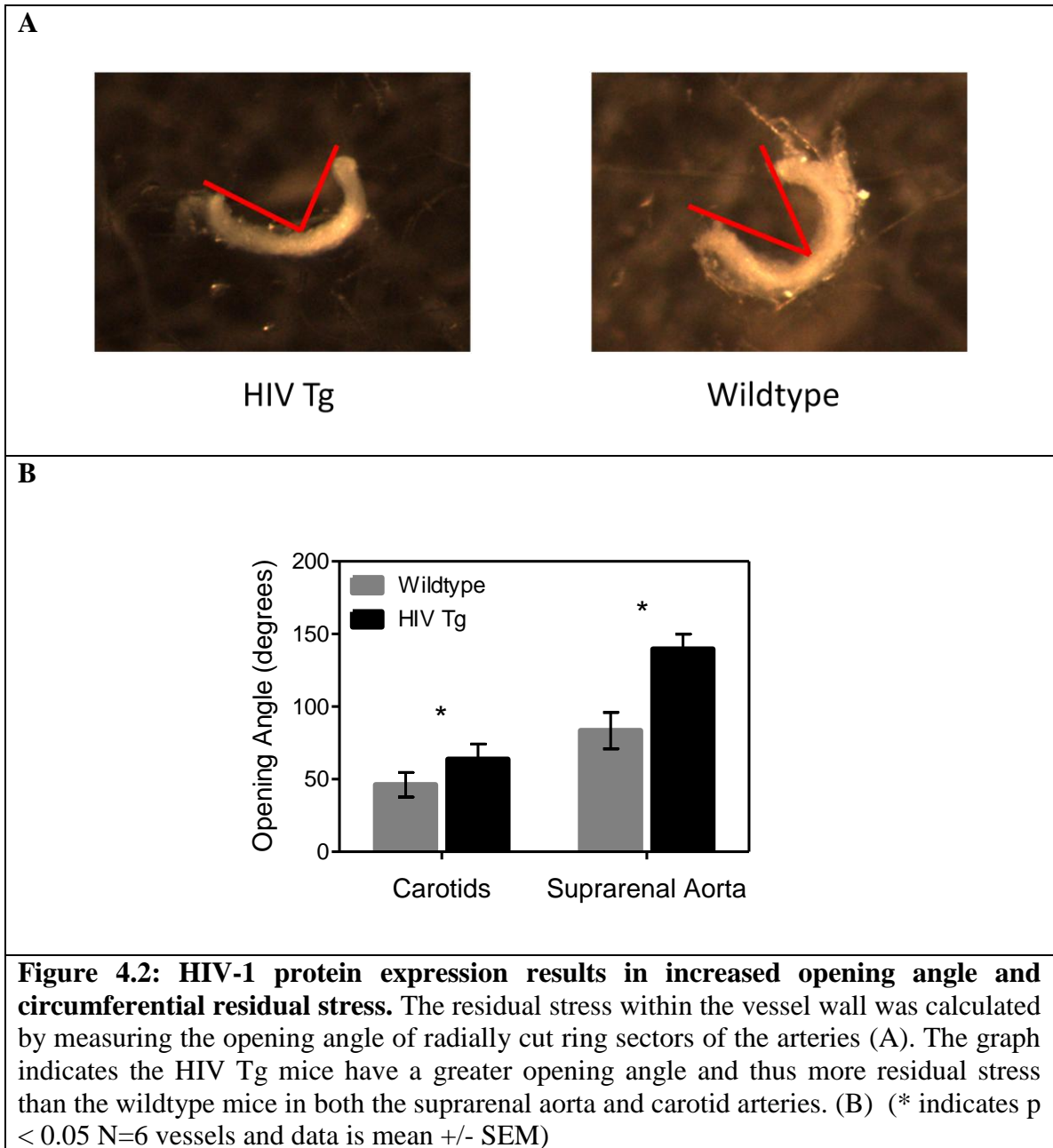


**Figure 4.1: HIV-1 protein expression increases arterial stiffness.** Mechanical testing was used to investigate the biomechanics of carotid arteries (A, B) and aortas (C, D). Pressure-diameter mechanical tests (A & C) were performed at a series of fixed stretches. Peterson's modulus,  $E_p$ , of the vessels was used to normalize for differences in vessel geometry (B & D, \* indicates  $p < 0.05$ ,  $N=9$ , and data is mean  $\pm$  SEM)



observed in the *in vivo* axial stretch across groups. There was no significant difference in the axial force-length behavior of the vessels over physiologically relevant loads; for the carotids significant differences in the axial force length response were observed at the low stretches and low pressures (Figure A.4 B in appendix). No significant differences in the axial behavior of the aortas were observed at any loading conditions. Both the carotids and suprarenal aortas from HIV Tg mice had larger opening angles compared vessels from wildtype mice (Figure 4.2). The increased opening angle in the HIV Tg mice indicated there was a greater residual stress in the vessel wall in the unloaded state, which suggests that cells within wall have remodeled as an adaption to changes to maintain local stress in the loaded state.

#### **4.2.2 Mice expressing HIV proteins have increased carotid intima-media thickness**

HIV Tg mice showed increased intima-media thickness compared to control mice, confirmed by both the histological and confocal microscopy methods (Figure 4.4). Confocal microscopy images of the arteries in their physiological state (pressure=100 mmHg and  $\lambda=1.7$ ) (Figure 4.3) revealed an increased medial thickness in the HIV Tg mice for both the suprarenal aorta and carotids. Additionally, the carotids in the HIV Tg mice had adventitial thickening. (Figure 4.4 A) Histological slides stained with H&E also showed intima-media thickening in the HIV Tg mice for both vessels in their unloaded state (Figure 4.4 B). Note that the values of mean intima-media thicknesses measured from the confocal images were smaller than the values measured with histology as the confocal measurements were collected in a physiological (loaded) state in which the vessel would have thinned while histological slides were unloaded vessels.

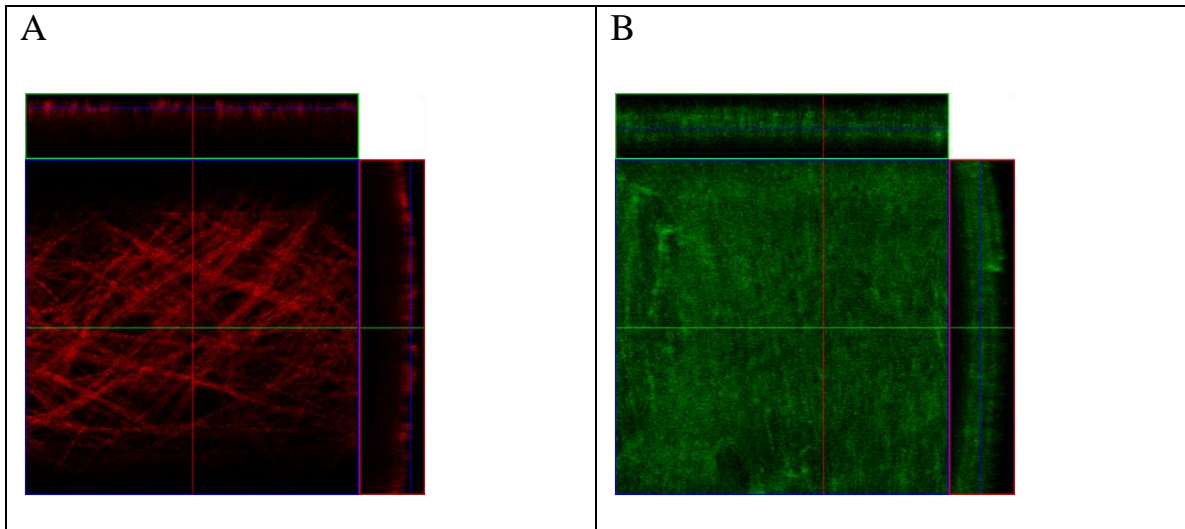


**Figure 4.3: Confocal images can be used to quantify thickness and collagen fiber distribution.** Confocal microscopy techniques were used to collect z-stacks of the collagen (A) and elastin (B) in a loaded physiological state (pressure=100 mmHg and  $\lambda=1.7$ ).

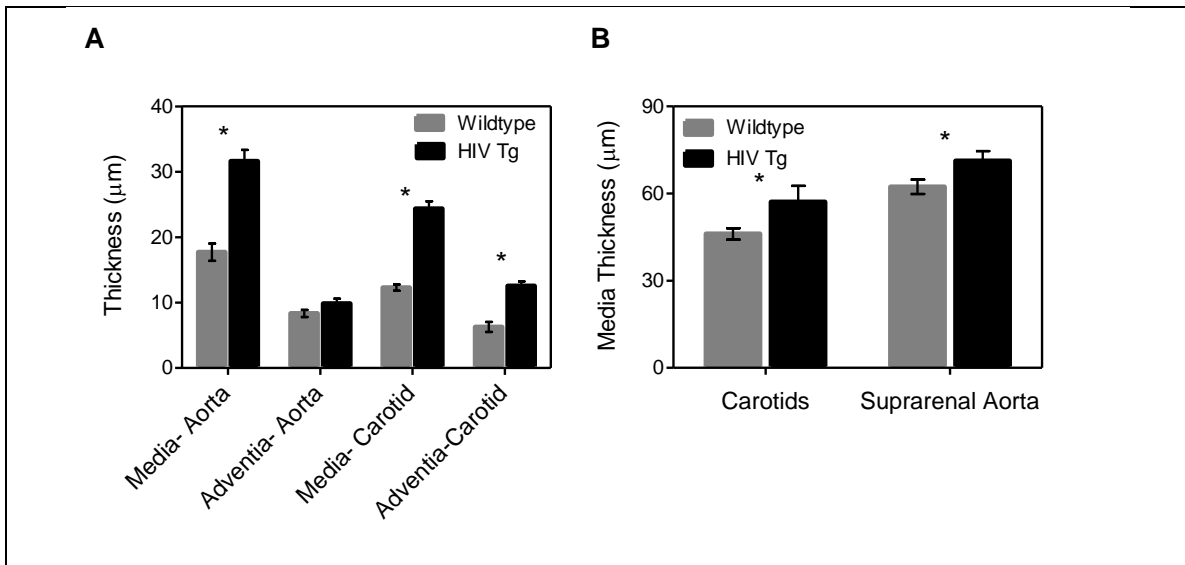


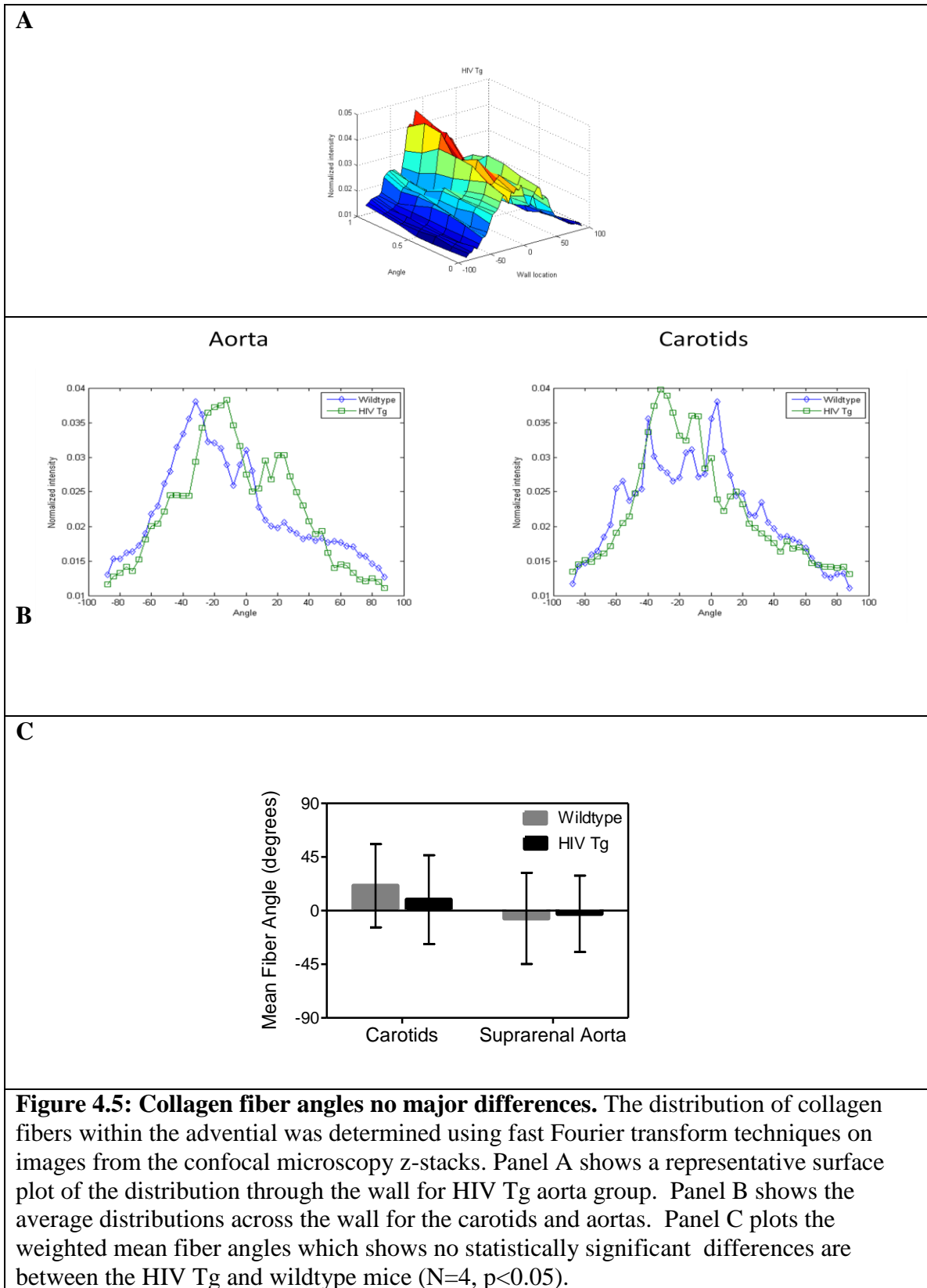
**Figure 4.4: HIV-1 protein expression increases intima-media thickness.** Thickness of the arteries was calculated using cross-sectional views from confocal microscopy stacks of collagen and elastin autofluorescence and histology cross-sections. Panel A shows the thickness values calculated from cross-sectional views of confocal microscopy image stacks of the arteries under a physiological load (pressure=100 mmHg and  $\lambda=1.7$ ). The intima-media thickness in the HIV Tg mice was increased for both arteries, and the carotids also had an adventitial thickening. Panel B shows the intima-media thickness calculated from fixed/frozen histological slides stained with H&E and thickness was calculated using ImageJ. (\* indicates  $p < 0.05$ ,  $N=6$ , data is mean  $\pm$  SEM)

### **4.2.3 Collagen Fiber Angles are similar between groups**

The distribution of the collagen fiber angles in the adventia was also quantified as collagen fibers contribute significantly to the mechanical behavior of the arterial wall and changes in orientation could possibly play a role in describing differences in that behavior. Thus a fiber angle distribution was calculated using fast Fourier transform techniques for each image in the confocal microscopy z-stacks. These distributions were used to create surfaces of the fiber angle distribution through the wall as shown in figure 4.5 A. The average of the distributions through the wall was calculated (figure 4.5 B) but the weighted mean fiber angles for the vessels (a measure of the peak) showed no significant differences in distribution (figure 4.5 C).

### **4.2.4 Elastin breaks**

A set of histological slides were stained with Verhoeff-Van Gieson stain which stained the elastin fibers black. The slides were then inspected for breaks in the elastic lamellae, but no distinguishable breaks were seen in either the HIV Tg or control mice.

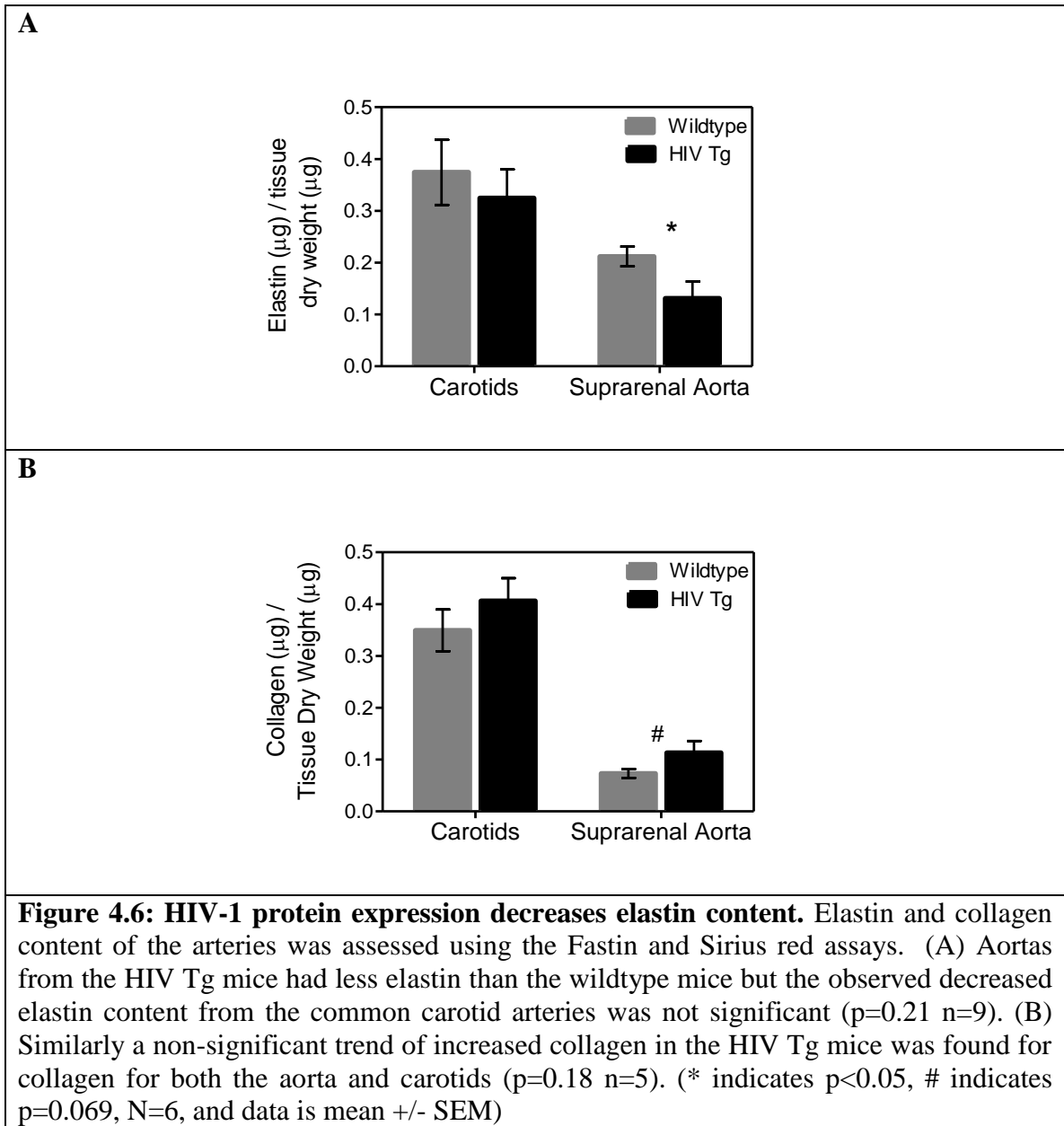


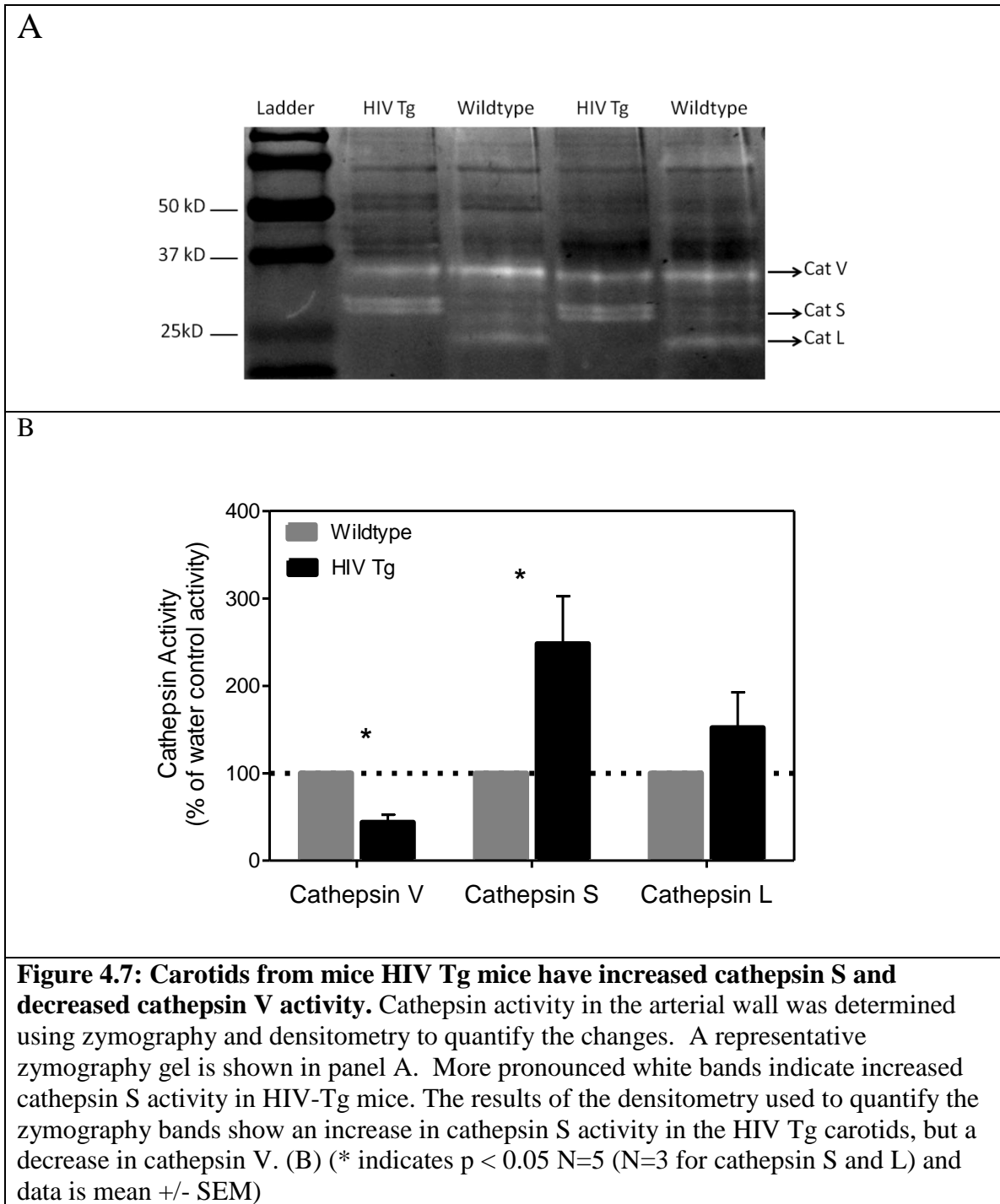
#### **4.2.5 Aortas from mice expressing HIV proteins have lower elastin content**

The normalized elastin content of the suprarenal aortas and carotids was determined using the Fastin assay (Biocolor). The HIV Tg aorta had significantly less elastin than the wildtype (HIV Tg = 0.21  $\mu\text{g}$  elastin/  $\mu\text{g}$  dry tissue and wildtype= 0.13  $\mu\text{g}$  elastin/  $\mu\text{g}$  dry tissue). The elastin content of the carotids was not significantly different but had values of 0.32 and 0.37  $\mu\text{g}$  elastin/  $\mu\text{g}$  dry tissue for HIV Tg and wildtype respectively (p=0.21 n=9). (Figure 4.6 A) Collagen content was also assessed using Sirius red staining as shown in Figure 4.6 B. The HIV Tg mice had a non-significant trend of more collagen for both the aorta and carotids (p=0.069 n=6 and p=0.18 n=5 respectively). The decrease in elastin content and trend in increased collagen content aligns well with the finding that vessels from HIV Tg have increased arterial stiffening.

#### **4.2.6 Aorta from mice over-expressing HIV proteins exhibit increased cathepsin K and S activity.**

Cathepsins K, S, and V are potent elastases. Zymographic analysis of homogenized carotids from HIV-Tg and wildtype mice show an almost 2.5 fold increase in the activity of cathepsin S (n=3 p<0.05). Cathepsin V, however, decreased in the HIV Tg carotids as compared to the wildtype controls (n=5 p<0.05) (Figure 4.7). These results are in agreement with similar results by my collaborators who found increases in cathepsin K and S as well as the decrease in cathepsin V in the HIV Tg suprarenal aortas (Figure A.5 in appendix). Increased proteolytic activity by cathepsins supports the finding of decreased elastin in the HIV Tg arteries. While this decrease in elastin is only significant in the aortas, the method used to quantify elastin determines with the total content without regard to cross-linking or damage so the cathepsin activity may still be





degrading the elastin but the protein has not yet been removed from the tissue and the assay lacks the sensitivity to detect very small changes.

#### **4.4 Discussion**

Clinical data clearly show endothelial dysfunction (8, 9, 14, 19, 20), increased arterial stiffness (8, 77, 137, 159-161), and increased c-IMT (8-13) in HIV patients, which have been attributed both to HAART treatment and HIV infection (162). This aim corroborates these findings in HIV-Tg mice, suggesting that HIV-1 proteins alone, independent of HAART treatment or HIV infection, may play a role in cellular and tissue level remodeling associated with atherosclerosis.

Lorenz et al., suggest that HIV-1 and HAART are independent mediators of carotid intima-media thickening. These studies found that the intima-media thickness of the carotid bifurcation was 24.8% higher in HIV-1 positive/HAART-naïve patients compared to uninfected controls, but they observed significantly greater intima-media thickness of the carotid bifurcation and the common carotid artery due to HAART treatment in HIV-1 positive subjects, compared to HIV-positive / HAART naïve subjects (163). Arteries from the HIV-1 Tg mouse exhibited increased intima-media thickness. Additionally, we did find an increase in adventitial thickness in the HIV Tg carotids as well, though this is not a clinically measurable parameter. These findings indicate that HIV-1 proteins alone may play a role in cellular and tissue level remodeling associated with atherosclerosis.

Arterial stiffening is an important clinical marker of cardiovascular disease; indeed, arterial stiffening is a key predictor of future cardiovascular events (164). Vascular ultrasound studies have shown increased stiffness in carotid and femoral

arteries, and pulse wave analysis and pulse wave velocity studies suggested elevated aortic stiffness from HIV-1 patients regardless of HAART treatment (8, 77, 137, 159-161). Rigorous mechanical tests on aorta and common carotid arteries from the HIV-TG and wild-type mice revealed that arteries were stiffer in HIV-Tg mice, indicating the HIV proteins alone may play a role in the increased stiffness that is observed clinically. Although HIV-associated immune dysfunction is known to play a role in atherosclerotic development (165) and has been associated with arterial stiffness in HIV-infected subjects (159), this mouse model lacks infected immune cells; however, the results suggest that changes in response to the proteins themselves may mediate the arterial stiffening in this mouse model through mechanisms that are yet to be determined.

In addition to corroborating clinical observations in HIV-patient populations and isolating the role of a single mediator (e.g., HIV proteins) on disease progression, one of the key advantages of animal models is the ability to collect measurements that cannot be obtained from human subjects. Biomechanical analysis revealed several important findings that are not experimentally tractable in patients. First, although differences were observed in the circumferential mechanical response of arteries, there were few mechanical differences in the axial direction. Also, observed differences in the opening angle suggest differences in the local, *in vivo* mechanical environment (i.e., the local stresses) under physiological loads at different locations across the vessel wall. Such differences in the local circumferential mechanical environment may provide insights into local differences in mechanically-mediated biological responses.

Vascular remodeling occurs in part by synthesis, proteolytic degradation, and remodeling of key structural components of the arterial wall (e.g., elastin and collagen)

and changes in vascular functional (e.g., endothelial dysfunction), which can lead to changes geometric, and biomechanical properties of the artery (e.g., c-IMT, and arterial stiffness, respectively). While the differences in collagen were not statistically significant, aortas from HIV Tg mice had significantly less elastin. Loss of functional elastin is often attributed with arterial stiffening and is common with aging, aneurysm development, and atherosclerosis (166, 167). Thus, the observed decrease in elastin supports the observed increases in arterial stiffness in HIV-Tg mice.

Upregulation of the cysteine cathepsin family of proteases in humans and mouse models of atherosclerosis are known to play a key role in vascular remodeling (147-149); cathepsin activity is upregulated in atheroprone regions of the vasculature (168). Zymography revealed cathepsin S activity in the arterial wall was increased two-and-a-half-fold in the presence of HIV proteins. These changes in cathepsin levels (Figure 4.7) may occur as the result of impaired nitric oxide production and bioavailability and/or pro-inflammatory viral proteins, thereby increasing elastolytic activity and degrading elastin in the arterial wall (Figure 4.6), leading to maladaptive remodeling that increases arterial stiffness (Figure 4.1), opening angle (Figure 4.2), and c-IMT (Figure 4.3).

This aim presents observational results that expression of HIV proteins leads to geometric, functional, and biomechanical changes that are consistent with clinical observations in HIV populations. The mechanisms by which HIV proteins lead to such changes, however, remain unknown. HIV-1 has not been shown to infect vascular endothelial cells *in vivo*; however, it is postulated that in HIV-infected populations endothelial dysfunction may be caused by exposure to circulating infected CD4+ T cells and monocytes as well as viral proteins that have been released into the blood (81, 84,

85). The *tat* protein, which is actively secreted by infected cells, has been found to have a variety of negative effects on the vasculature. Namely, *tat* has been shown to decrease the ability of pig coronary arteries to dilate by the inhibiting the expression of nitric oxide synthase (NOS) and thus nitric oxide availability (84). Exposure of endothelial cells to *tat* also causes them to release monocyte chemoattractant protein-1 (MCP-1), which increases adhesion to the endothelium and transendothelial migration of circulating mononuclear cells into the vascular wall (85). Numerous other studies have found various other effects of *tat*, *gp120*, *vpu*, and *nef* proteins on endothelial cells including expression of several cell adhesion molecules, increasing endothelial permeability, cell proliferation, cytokine signals, apoptosis, and oxidative stress (81). In this study, a transgenic mouse model (NL4-3Δ *gag/pol*) was employed to investigate the effects of HIV proteins and while a non-infectious mouse model, the mice have a similar phenotype to the altered signaling and function that has been observed in vascular endothelial cells exposed to HIV-1 proteins.

While there are compelling arguments to suggest that the observed vascular changes may be a direct result of HIV-1 proteins on vascular cells, there are also compelling arguments to suggest that these observations are a secondary effect of other systemic changes, such as end-stage organ disease, dyslipidemia, hypertension, and/or inflammation. For example, Kopp et al. reported that the NL4-3Δ *gag/pol* transgenic hemizygous mice develop proteinuria by 4 weeks of age and end-stage renal disease by 14 weeks (Kopp et al 1992). Such renal disease and associated hypertension could lead to some of the observed vascular changes reported here. Given that such secondary complications (e.g., neuropathy) also occur in HIV-patients, we submit that (whether the

underlying mechanisms are a direct affect of HIV-1 proteins or a downstream affect of other systemic changes) this model captures many of the salient features of HIV-associated cardiovascular disease and provides a platform to study the underlying mechanisms of HIV-1 protein mediated mechanisms of atherosclerosis.

In summary, the HIV-Tg mice did exhibit several characteristics that are indicative of preclinical atherosclerosis. The HIV-Tg mouse model offers the advantage of isolating the effects of the viral proteins not possible clinically. While data from clinical studies have found that HIV-1 positive patients exhibit early markers of atherosclerosis, some discrepancies still exist between studies due the inability to control other cardiovascular risk factors such as age, gender, weight, cholesterol levels, smoking, and hypertension in all patients as well the confounding effects from HAART therapy. This study isolates the *in vivo* effects of the HIV-1 proteins without these confounding factors. Whereas *in vitro* studies have observed some effects such as endothelial dysfunction and monocyte adhesion (81, 84-86), those *in vitro* models do not allow for the study of clinically observed characteristics such as arterial stiffening and thickening. These findings support the further use of this animal model to study mechanisms involved in the progression of HIV-associated atherosclerosis.

## CHAPTER 5

### **Specific Aim 3: Characterize the mechanical behavior, microstructure, protease activity, and ECM gene expression of arteries from wild type mice given the antiretroviral medication AZT.**

#### **5.1 Introduction**

The development and widespread use of HAART has increased the life expectancy of HIV patients in recent years. However, the drugs have been implicated in the early on-set and increased risk of numerous co-morbidities, including cancers, pulmonary disease, renal disease, hepatic disease, diabetes, and cardiovascular disease. The latter includes increased myocardial infarction (65, 66, 169) and atherosclerotic lesions (67, 170). Additionally, an increase in a number of preclinical signs of atherosclerosis including increased carotid intima-media thickness (c-IMT) (8, 72, 171), arterial stiffening (8, 78, 79), and impaired flow mediated dilation (FMD), an indicator of endothelial dysfunction (78, 90, 91) is seen in HIV patients on HAART.

The role of specific HAART drugs in these symptoms remains unclear. While some studies have suggested that viral infection itself plays a significant role (73, 76, 172), many studies have implicated HAART as playing a significant role in atherosclerotic development (87, 88). Specifically, the nucleoside reverse transcriptase inhibitors (NRTIs), which include azidothymidine (AZT), and protease inhibitors (PIs) have been shown to cause changes that might be implicated in endothelial dysfunction. (81, 173) These two classes of drugs have widespread use and are included in most HAART regimens and thus have been implicated in the development of atherosclerosis.

(66, 174) Herbert et al. found that AZT caused significant decreases in cellular respiration, a marker for mitochondrial activity.(95) Administration of the drugs also increased cell death in endothelial cells and increased vascular smooth cells replication, both of which disturb healthy vascular function. Another study with AZT found that treatment of healthy mice with AZT for 35 days reduced the endothelial-dependent dilation of the aorta when exposed to acetylcholine. Additionally, the vessels had significantly increased superoxide levels. (96)

The purpose of this aim was to investigate the effects of AZT treatment on arteries from healthy mice specifically with respect to the other subclinical markers such as arterial stiffening and intima-media thickening. The use of a healthy mouse model in the study allowed us to isolate the effects of a specific HAART drug on the artery without the influence of the HIV virus or the confounding factors in human studies, while also allowing us to investigate tissue level changes to the vasculature (structure and mechanical behavior) not studied in the previous *in vitro* studies. Potential arterial stiffening and overall mechanical behavior of the vessels was determined with cylindrical biaxial mechanical tests and opening angle measurements. Changes to the vessel geometry and microstructure, including intima-media and adventitia thickness, collagen fiber angle distribution, and elastin breakage were determined via confocal microscopy and histology. We also quantified of collagen and elastin content and measured protease activity (specifically cathepsins) through zymography. Additional, physiological factors such as blood pressure and plasma lipid levels were also quantified.

## **5.2 Methods**

### **5.2.1 Animal Model**

The animal model used for this study was healthy adult male FVB/N mice (Jackson Labs) (FVB/N is also the background strain of the mice in aim 2). The HAART drug selected for the study was AZT (azidothymidine), which is one of the common NRTIs. AZT was administered via oral gavage for 35 days at a dosage of 100 mg/kg AZT in 0.25mL water. The control mice were given 0.25 mL of water via oral gavage for 35 days. Treatment was initiated at 5 weeks of age and thus the average age of the mice at the end point was 10-11 weeks as with the previous aim.

### **5.2.2 Blood Pressure Measurements**

The blood pressure of the mice was monitored periodically throughout the time course of the treatment. Columbus Instrument's non-invasive blood pressure monitoring system was used to record the blood pressure and heart rate via a tail cuff system. The testing methods were followed as prescribed in the user's manual. To obtain accurate blood pressure measurements and acclimate mice to the restrainer chamber, mice were placed in the chamber for 30 minutes once a day for 3 days prior to actually collecting the data. The chamber was provided with the system and is a clear plastic tube with an adjustable endcap with a hole for the tail that was adjusted to fit snugly over the base of the tail preventing movement of the mouse. This is necessary because the tail must be held still in the sensor and occlusion cuff for accurate and noise-free measurements. To collect the data, the sensor and occlusion cuffs were threaded on the tail and positioned as close to the base as possible. Once restrained the heating unit was placed above the mouse's tail and heat was applied from 15-20 minutes until the unit's sensor reached a

temp of 37-39 degrees Celsius. Heating was done to improve blood flow in the tail but once the temperature was reached, the heating unit was turned off for the actual data collection. Once the tail was preheated, data was collected by starting a continuous scan, which inflated the occlusion and sensor cuffs to collect systolic, diastolic, and mean blood pressure as well as heart rate. Each collection cycle was repeated for 20 minutes and the average values of measurements were used for analysis. Blood pressure measurements were taken at the start of treatment, 2.5 weeks after treatment initiation, and 5 week after treatment initiation, just before the end of the treatment.

### **5.2.3 Common Carotid Artery and Aorta Preparation**

At the end of 35 days of treatment mice were euthanized with an intraperitoneal injection of sodium pentobarbital. Prior to opening of the chest cavity blood was collected via cardiac puncture. Briefly a 26 gauge needle was inserted at approximately a 30° angle just below the sternum, and the plunger was slowly withdrawn to collect 0.5-0.8 mL of blood. Following blood collection, the chest and abdomen were opened and both common carotids arteries and the aorta were removed and cleaned as in aim 2.

### **5.2.4 Lipid Studies**

The blood collected via cardiac puncture was immediately transferred to heparin coated tubes and centrifuged to separate the components. The plasma was removed and frozen for analysis of the blood lipid levels specifically cholesterol and triglycerides. The cholesterol levels were determined using an assay kit from Abnova, which detects both cholesteryl esters and free cholesterol by hydrolyzing the esters with the included esterase enzyme. The cholesterol is then oxidized and the resulting hydrogen peroxide is detected by ADHP (10-acetyl-3,7-dihydroxyphenoxazine), which reacts with horseradish

peroxidase to produce a detectable fluorescent compound. Briefly, a 1:400 diluted plasma sample in the assay buffer was pipetted into a 96 well plate and the assay cocktail mixture was added. The assay cocktail included assay buffer, the cholesterol detector (ADHP), horseradish peroxidase, cholesterol oxidase, and cholesterol esterase. The plate was then covered and incubated for 30 minutes and the cholesterol was detected using fluorescence with excitation wavelengths between 530-580 nm and emission from 585-595 nm.

Plasma triglyceride levels were determined using a colorimetric kit by Abnova. Briefly, the samples were pipette into a 96 well plate with the provided assay buffer. Lipase was added to the wells and incubated for 20 minutes at room temperature to convert all of the triglycerides to glycerol and fatty acids. Next, a reaction mix of assay buffer, a triglyceride probe, and a triglyceride enzyme mix was added to the wells and incubated for 30-60 minutes. Following, incubation the plate was read for absorbance at 570 nm.

### **5.2.5 Biomechanical Measurements: Cylindrical Biaxial Testing, Arterial Stiffness, and Opening Angle**

Cylindrical Biaxial Testing: As in aim 2, cylindrical biaxial biomechanical tests of the arteries were performed as previously described to characterize the biomechanical behavior of these arteries (150). Briefly, the cleaned arteries were cannulated on our custom built device and following preconditioning both pressure-diameter and force-length testing protocols were performed.

Arterial Stiffness: The Peterson's modulus ( $E_p$ ), a common measure of arterial stiffness, was calculated as the slope of the pressure-outer diameter curve ( $\Delta P/\Delta D$ ) at a

given pressure normalized to the outer diameter ( $D$ ) at that pressure; namely,  $E_p = \Delta P / (\Delta D / D)$ .

Opening Angles: Following testing or microscopy imaging (described below), ring sectors were cut from the arteries to obtain their stress free configuration. Opening angle measurements were taken to quantify the residual stress in the unloaded configuration following the same procedures described in aim 2.

### **5.2.6 Intima-Media Thickness Measurements**

The vessel wall thickness was quantified by two methods: confocal imaging of live arteries mounted on the biomechanical testing device was used to quantify the intima-media thickness and adventitia thickness, and standard histology of fixed, sectioned, and stained vessels was used as an additional measure to quantify intima-media thickness.

Confocal Microscopy: The custom biomechanical testing device fits on a LSM 510 META inverted confocal microscope (Zeiss) to visualize the microstructure across the entire wall of live, unfixed mouse arteries (150). Collagen and elastin were imaged using their autofluorescent properties as described in aim 2.

Histology: The same histological methods as aim 2 were employed with vessels were fixed in their unloaded state, frozen for sectioning, and stained with hematoxylin and eosin. The images were analyzed using ImageJ (NIH) to quantify the thickness of the arteries.

### **5.2.7 Other Microstructure Analysis**

Collagen Fiber Analysis: The confocal microscopy images were also used to quantify the angular distribution of fibers within the arterial wall using the fast Fourier

transform method described in aim 2. The thickness and relative wall location were normalized and the corresponding distributions in each vessel were averaged to create a surface which represented the fiber angle distributions through the wall for both groups.

Elastin breaks visualization: As in aim 2, slides were prepared using the same protocols for the histological thickness measurements. These slides were stained with Verhoeff-Van Gieson elastin stain to quantify potential elastin breaks.

### **5.2.8 Collagen and Elastin Content Measurements**

The Fastin assay (Biocolor) and Sirius red assay were used to quantify the elastin and collagen content of the dried arteries using the same methodology more thoroughly explained in aim 2. The extract proteins for were measured on a plate reader and the values were normalized to the tissue dry weight for analysis.

### **5.2.9 Cathepsin Expression and Activity Measurements**

Gelatin zymography was used to quantify the activity of cathepsins in the arterial walls. As in aim 2, the tissues (1 aorta or 2 pairs of carotids) were homogenized, protein concentration was determined and the samples were loaded in a SDS-page gel containing gelatin and were separated using electrophoresis. The enzymes were then renatured and activated using a series of buffers, and gels were stained for detection of the bands which remain light. Gels were then scanned and densitometry was performed to quantify activity.

### **5.2.11 Statistical Analysis**

All data presented is mean plus or minus standard error mean ( $\pm$ SEM). Means between groups were compared using unpaired student t tests with significance at  $p <$

0.05. All statistics were performed in either Excel (Microsoft) or GraphPad Prism (GraphPad software).

## **5.3 Results**

### **5.3.1 Mice treated with AZT do not have increased blood pressure**

Blood pressure was monitored at three time points (beginning, middle, and end) throughout the study using a tail-cuff measurement system. The results showed no difference in the diastolic or systolic blood pressure between the groups at both the start and end of treatment (Figure 5.1). A slight increase was observed with time but this is expected as the mice aged from 5 to 10 weeks.

### **5.3.2 Lipid profiles did not differ between treatment groups**

At the end of the 35 days of treatment blood was collect from the mice and the plasma was used to analyze the lipid profiles in the mice. No detectable differences in cholesterol and triglyceride levels were found between the mice (Figure 5.2).

### **5.3.3 Mice treated with AZT exhibit increased arterial stiffness and altered biomechanics**

Cylindrical biaxial tests revealed that treatment with AZT causes arterial stiffening. Figure 5.3 (A & C) show that the AZT diameter-pressure curve for the *in vivo* stretch ( $\lambda=1.7$ ) is shifted downward, meaning that for a given pressure the arteries from the AZT treated mice distended less. The carotids were significantly different at pressures of 10-60 mmHg (N=6,  $p<0.05$ ) while the aortas had statistically significant differences at 50-70 mmHg (N=8,  $p<0.05$ ). Additionally, the aortas for the AZT mice were significantly smaller at pressures of 10-90 mmHg at a subphysiological stretch (Figure B.1 in appendix). The Peterson's modulus ( $E_p$ ), a common measure of arterial

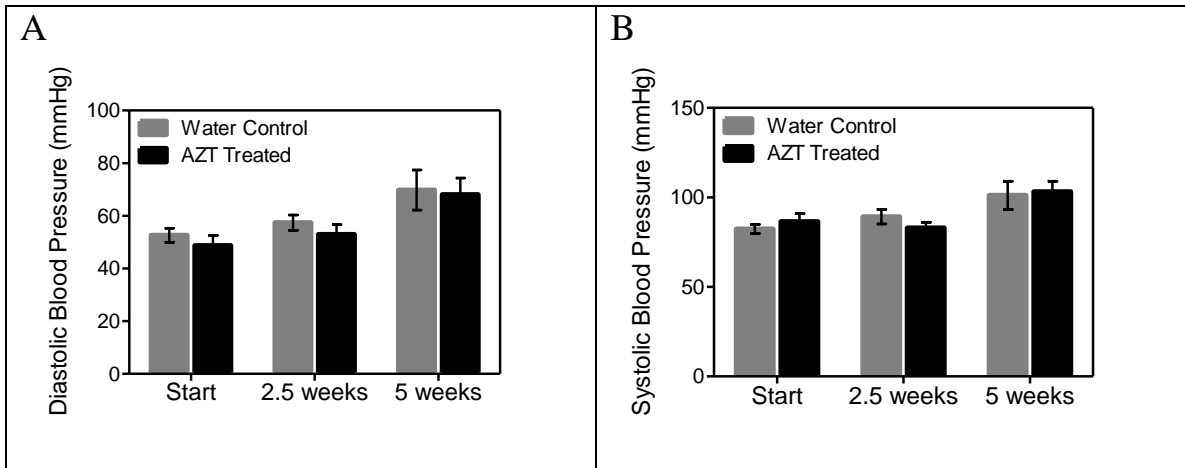


**Figure 5.1 Blood pressure does not differ between groups.** The blood pressure of the mice was determined using a tail-cuff blood pressure system. Both the diastolic (A) and systolic (B) pressures were measured at the initiation of treatment, 2.5 weeks after treatment initiation, and 5 weeks after the initiation of treatment (end of treatment). No differences were noted between groups at any time. (N=7)

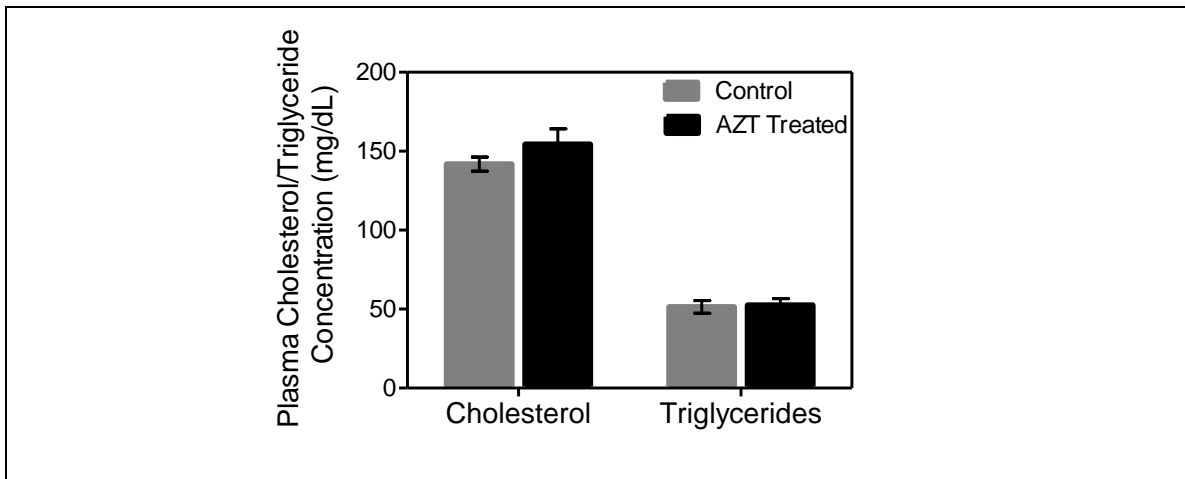


**Figure 5.2 AZT treatment did not alter lipid profiles.** Plasma lipid profiles were performed on blood collected from the mice at the end of the treatment. Specifically, cholesterol and triglyceride concentrations were quantified; however, no difference was found between the groups. (N=4 N=6, data is mean +/- SEM)

stiffness, was calculated as the slope of the pressure-outer diameter curve ( $\Delta P/\Delta D$ ) at a given pressure normalized to the outer diameter ( $D$ ) at that pressure; namely,  $E_p = \Delta P / (\Delta D / D)$ . Modulus results for the aorta showed an increased modulus for the AZT treated mice with statistically significant differences at pressures between 10-40 mmHg at the *in vivo* stretch (Figure 5.3 D) and 30- 60 mmHg at a subphysiological stretch (Figure B.2 in appendix). As with the mechanics results in chapter 4 (Figure 4.1), some of these statistically significant differences occur at pressures lower than physiological blood pressures. We hypothesize that differences at these slightly subphysiological pressure are due to removal of perivascular support when the arteries are excised from the mice, which would allow them to expand to diameter larger than those seen *in vivo* and we further hypothesize that the diameters at which the statistically significant differences occur are closer those experiences in the body while the pressures are lower in the constrained mechanical tests. Current studies in our lab have suggested this is the case for porcine coronaries but the hypothesis has not been tested in mice.

Axial force was also monitored during the pressure-diameter tests to study the pressure-force relationship. Analysis revealed that the AZT treated aortas had lower axial forces at pressure from 10-80 mmHg at the *in vivo* stretch and a subphysiological stretch and 10-70 mmHg at a superphysiological stretch (Figure 5.4) (N=8,  $p < 0.05$ ). Additionally, the axial behavior in the force-length tests does not have any major differences in both the carotids and aortas.

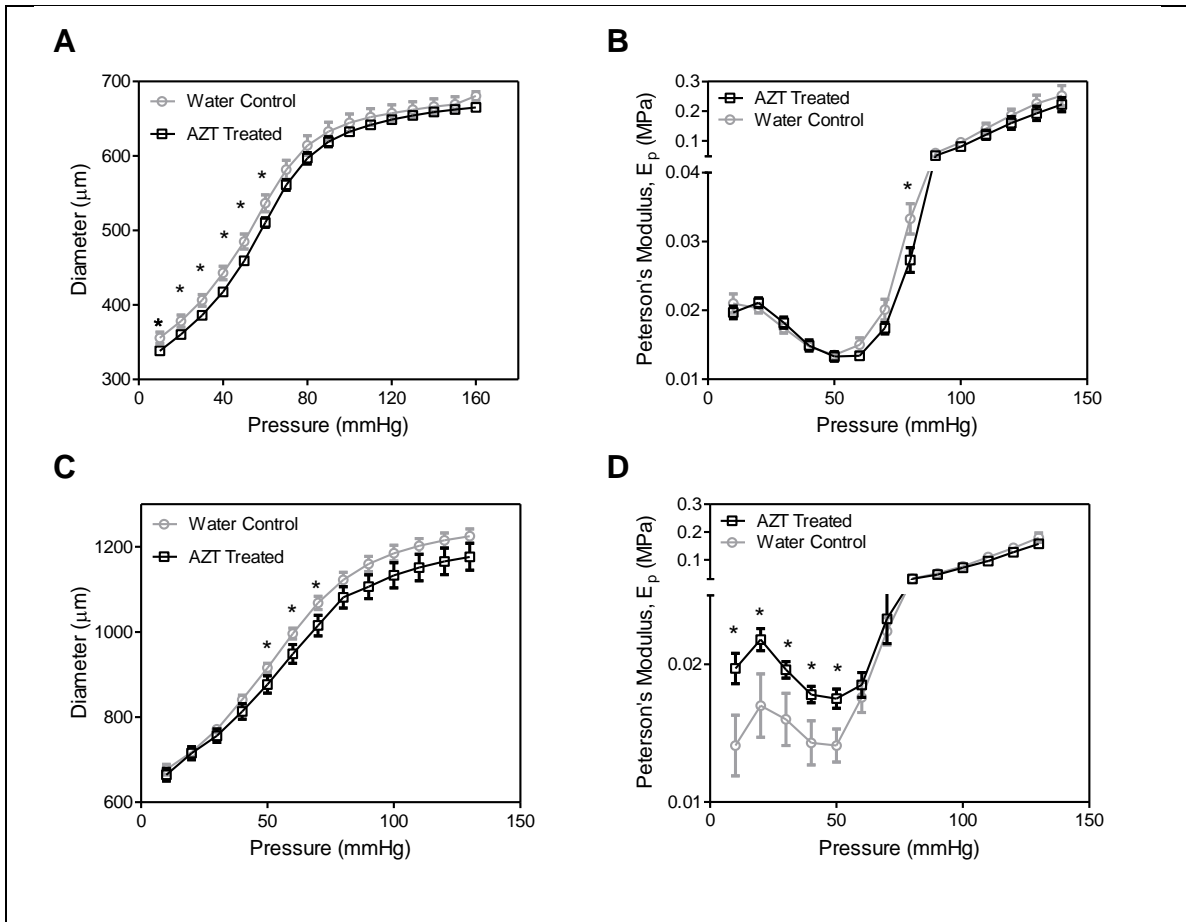


**Figure 5.3: AZT treatment increases arterial stiffness.** Mechanical testing was used to investigate the biomechanics of carotid arteries (A, B) and aortas (C, D). Pressure-diameter mechanical tests (A & C) were performed at a series of fixed stretches. Peterson's modulus,  $E_p$ , of the vessels was used to normalize for differences in vessel geometry (B & D, \* indicates  $p < 0.05$ ,  $N=9$ , and data is mean  $\pm$  SEM)

Opening angle, an indicator of residual stress, was also quantified though no significant changes were seen for both the carotids and aorta Figure 5.5.

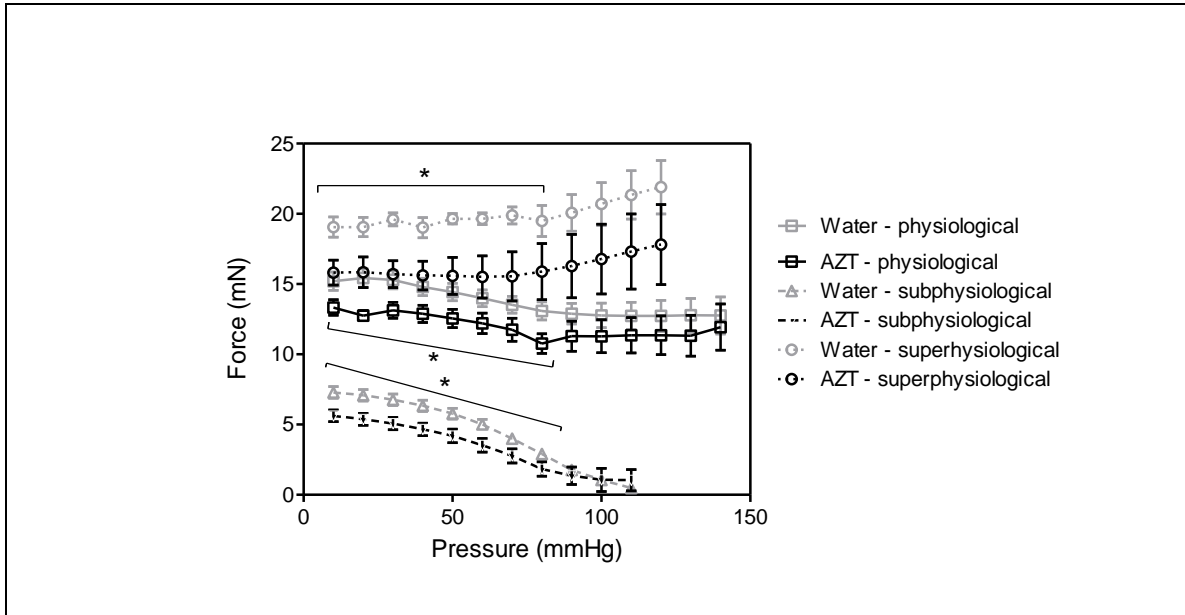


**Figure 5.4: AZT treatment decreases axial force during pressure-diameter tests.** Axial force was also measured during the pressure-diameter mechanical tests. Analysis of the axial force revealed that the AZT treated mice had significantly lower forces at pressures from 10-80 mmHg for the subphysiological and physiological stretch and from 10-70 mmHg for the superphysiological stretch. (■ is physiological stretch, ▲ is subphysiological stretch, and ● is superphysiological stretch, \* indicates  $p < 0.05$ ,  $N=9$ , and data is mean  $\pm$  SEM) No differences were found in the carotids.

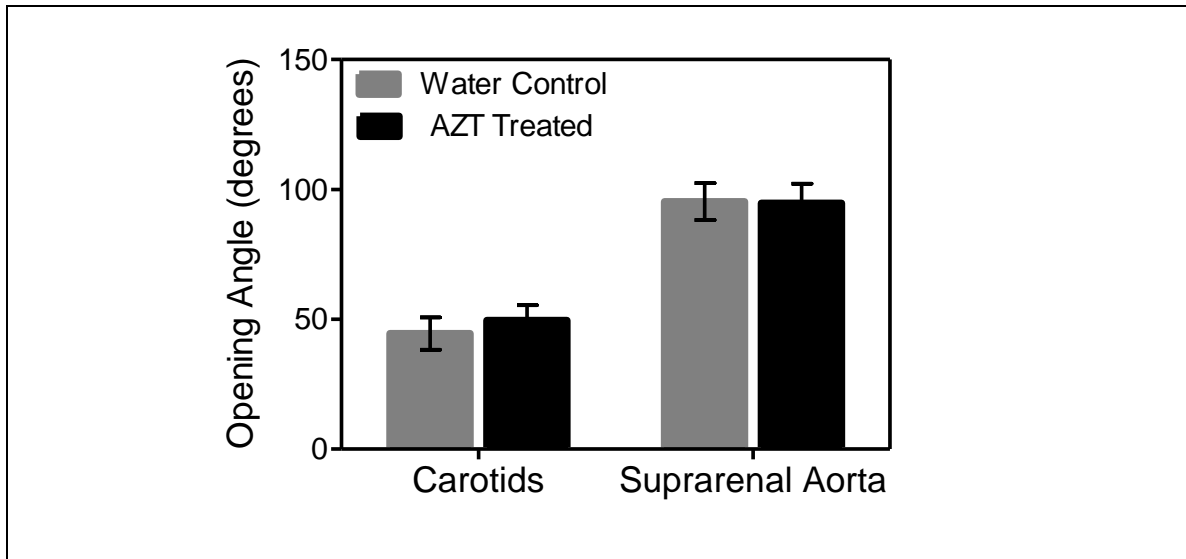


**Figure 5.5: AZT treatment did not result in opening angle differences.** The residual stress within the vessel wall was calculated by measuring the opening angle of radially cut ring sectors of the arteries. The graph indicates the AZT treated mice and water mice have the same opening angle and thus the treatment did not result in changes in residual stress between the groups. (N=6 vessels and data is mean +/- SEM)

### 5.3.4 Mice treated with AZT have increased carotid intima-media thickness

The wall thickness of both arteries was quantified using two different methods. Confocal microscopy techniques were used to quantify both the intima-media (elastin images) and adventia (collagen images) of the arteries in a physiological state (pressure = 100 mmHg and axial stretch  $\lambda=1.7$ ). The z-stacks of images showed increased media thickness (aorta N=6  $p<0.05$ ) while advential thickness decreased (N=6,  $p<0.05$ ) (Figure 5.6 A). The increase in intima-media thickness was also confirmed with the histological measurements from fixed and frozen unloaded vessels, see Figure 5.6 B. (N=6,  $p<0.05$ ) Notice, that the thickness values are slightly different between the confocal and

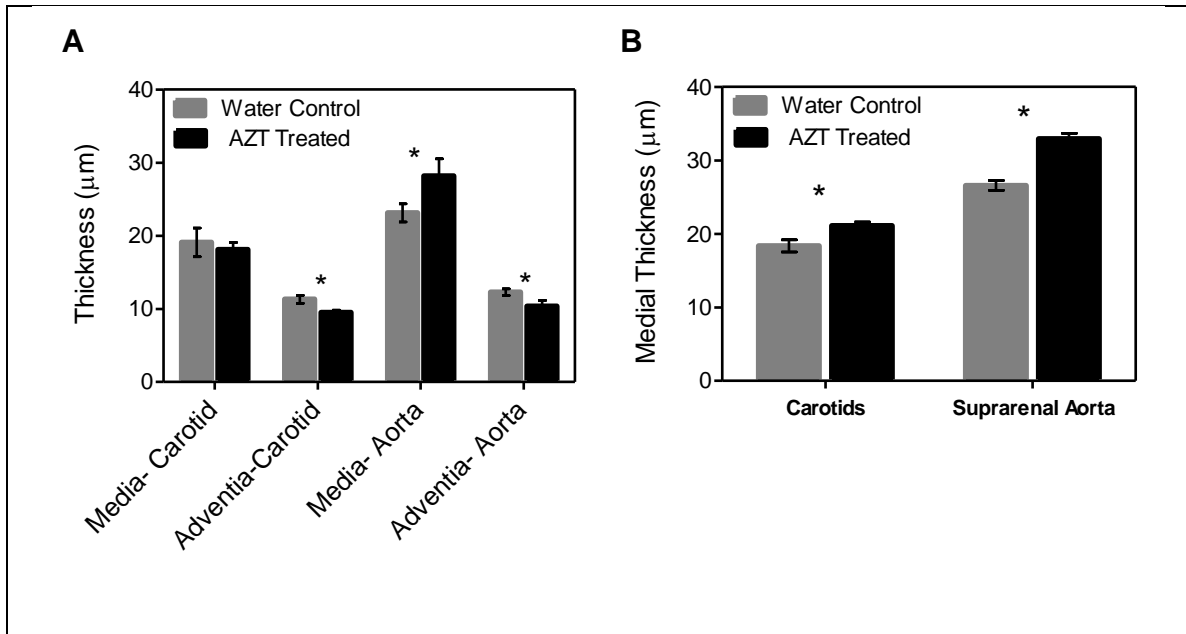


**Figure 5.6: AZT treatment increased intima-media thickness.** Thickness of the arteries was calculated using cross-sectional views from confocal microscopy stacks of arteries under a physiological load and histology cross-sections. (A) The intima-media thickness in the AZT treated mice increased in the aorta, but the adventia was decreased in both the aortas and carotids. (B) The intima-media thickness calculated from fixed/frozen histological slides stained with H&E also showed intima-media thickening for both carotids and aortas. (\* indicates  $p < 0.05$ ,  $N=6$ , data is mean  $\pm$  SEM)

histological techniques are slightly different, this discrepancy could be partially due to confocal measurements being taken at a loaded configuration and the histology is unloaded as well as processing to the histological samples.

### 5.3.5 Collagen fiber distributions are similar between groups

The confocal microscopy z-stacks were also used to quantify the angles of the collagen fibers in the physiological state. A fast Fourier transform routine produced a fiber distribution of collagen throughout the arterial wall. The normalized average of the distributions is shown in figure 5.7 A&B. The mean fiber angle was also calculated for

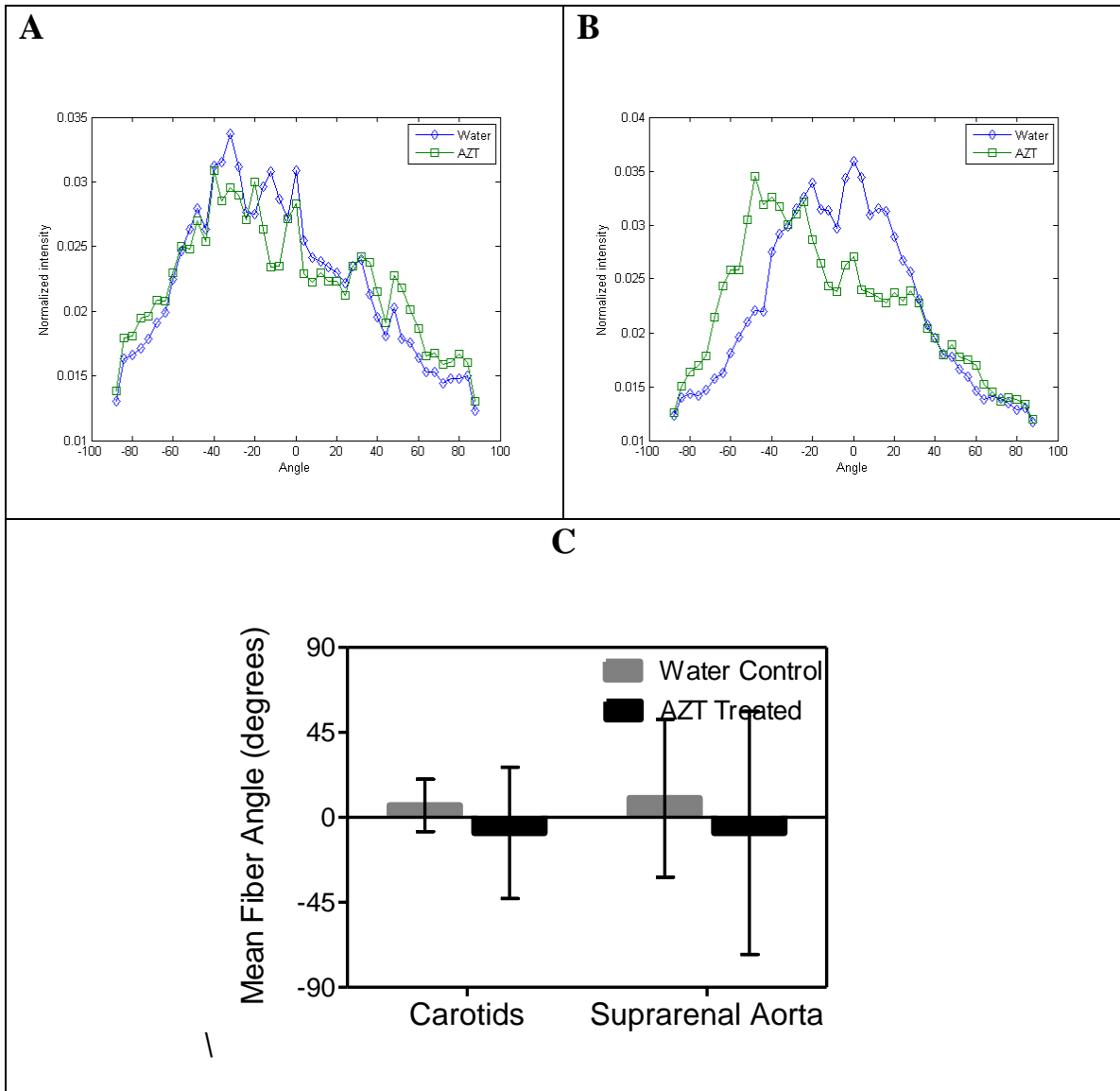


**Figure 5.7: Collagen fiber angles no significant differences.** The distribution of collagen fibers within the adventia was determined using fast Fourier transform techniques on images from the confocal microscopy z-stacks. Plots of the average distributions across the wall are shown in A for the carotids and B for the aortas.) The mean angle from each vessel was also calculated and no differences were found between groups (C). (N=6, data is mean +/- SEM,  $p < 0.05$ )

each groups' distribution and no differences between the arteries from the AZT and water treated mice were observed (Figure 4.6 C) (N=6).

### **5.3.6 Elastin breaks**

Histological slides were also stained with Verhoeff-Van Gieson elastin stain to better visualize the elastin. Inspection of the slides revealed intact elastic lamellae and no elastin breaks.

### **5.3.7 Carotids from AZT treated mice have lower elastin content**

The protein content of the major ECM components of the arteries was quantified for both the AZT and water treated mice. The Fastin assay (Biocolor) was used to quantify elastin content and the results showed a decrease in elastin for the carotids (N=6  $p<0.05$ ) (Figure 5.8 A). Note that the elastin content of the aortas is rather low (we would expect it to be the same or greater than the carotids) but this could possibly be due to incomplete extraction of the elastin as the same extraction procedure was performed on both the carotids and the aortas. However, following the same procedure in chapter 4 we were able to detect differences in the aortas (though the values are similar) while we did not see differences in the elastin values of the aortas in this chapter. The results of the collagen content assay (Figure 5.8 B) show no difference between the AZT treated and water treated mice.

### **5.2.8 Arteries from mice treated with AZT have differences in cathepsin activity.**

Cathepsins are a family of proteases with potent elastolytic and collagenase activity. Gelatin zymography was used to determine the cathepsin activity within the aortic and carotid walls. Densitometric analysis of the gels showed changes in expression between the AZT treated mice and the control mice. Specifically, the carotids from the

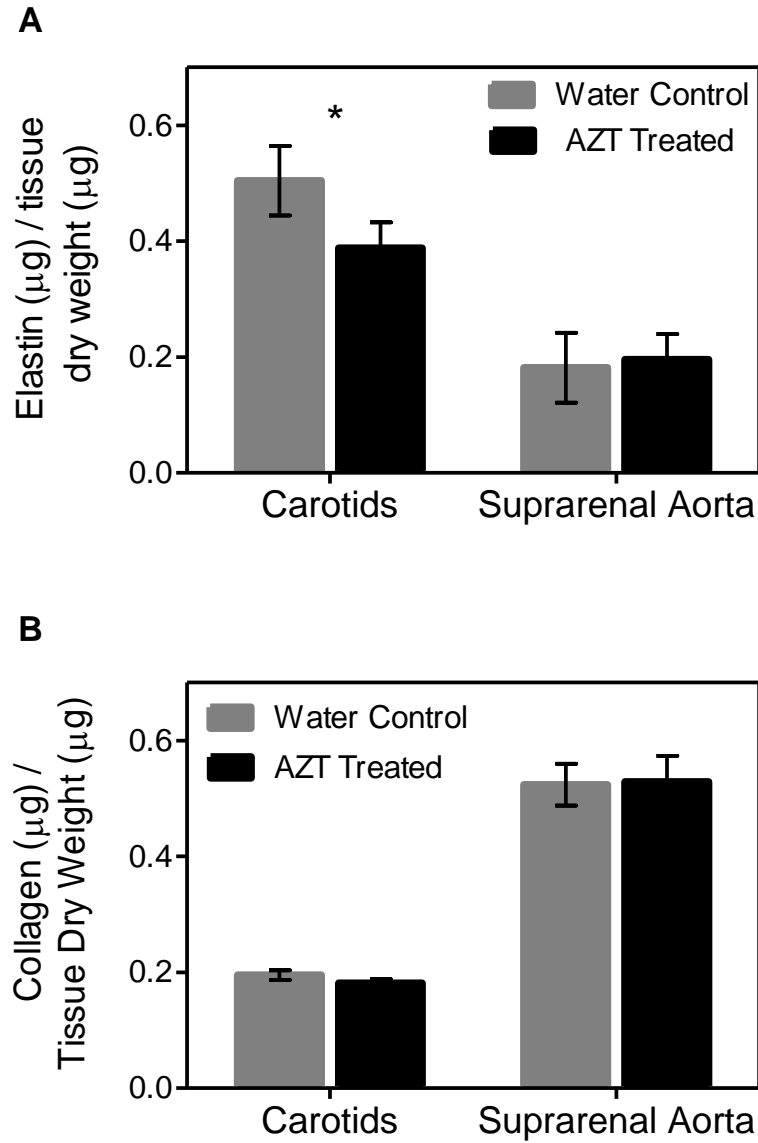
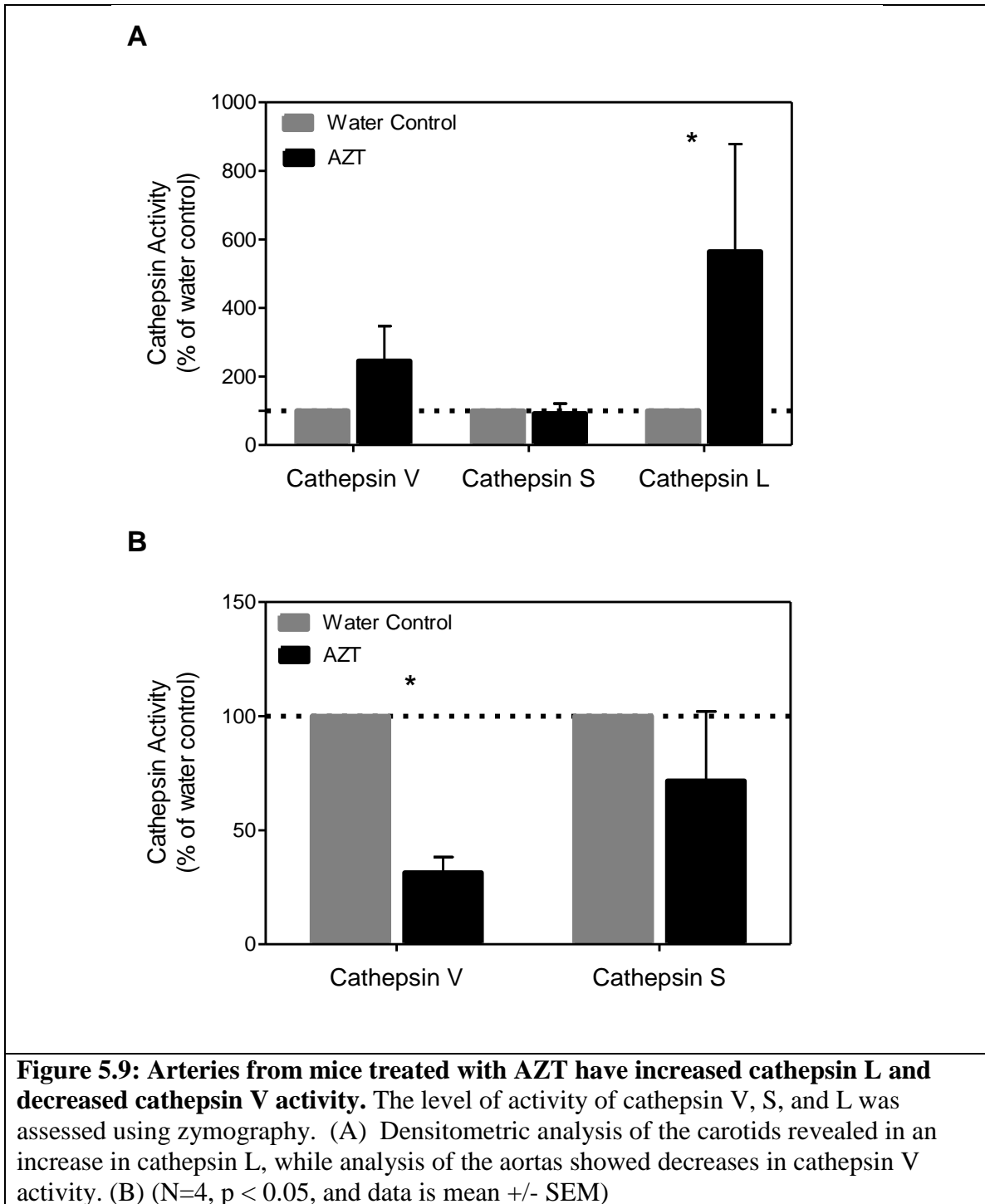


**Figure 5.8: AZT treatment decreases elastin content.** Elastin and collagen content of the arteries was assessed using the Fastin and Sirius red assays. (A) The carotids from AZT treated mice had less elastin than the water control mice. (\* indicates  $p < 0.05$ ,  $N=6$ , and data is mean  $\pm$  SEM). (B) No difference in the collagen content of the arteries was observed. ( $N=6$ , and data is mean  $\pm$  SEM)



AZT mice had over a 5-fold increase in cathepsin L activity compared the control mice (Figure 5.9 A). Additionally, in the aortas the cathepsin V activity in the AZT was decreased in comparison to the control mice (Figure 5.9 B).

#### **5.4 Discussion**

While clinical data has shown that patients with HIV-1 are more prone to atherosclerosis (66, 87, 88) and exhibit preclinical signs including endothelial dysfunction (78, 91), arterial stiffening (8, 78, 79), and increased intima-media thickness (8, 72, 75) and *in vitro* studies have shown that antiretroviral drugs specifically AZT have negative effects on vascular cells (95, 96) , the unique roles of the medication and virus remains unclear. This study investigated these effects using a mouse model to isolate the role of the antiretroviral drugs. In agreement with the clinical data we found the mice had both arterial stiffening and increased thickness. Additionally, we further investigated the structural changes occurring and found decreases in elastin mass fraction and changes in cathepsin activity both which supports the findings proatherogenic remodeling.

A study by van Vonderen et al. indicates that antiretroviral treatment may play a role in mechanical changes to the arteries (77). The study found significant decreases in femoral artery distensibility and compliance between ART-naïve and ART-exposed patients. Similarly, Charakida et al. also saw differences between treated and non-treated children with HIV with the treated group having a higher pulse wave velocity, a clinical measure of arterial stiffness. (175) In our study we saw similar results with mice treated with AZT having smaller diameter for a given pressure and a higher Peterson's modulus than the water treated control mice (Figure 5.3). Both of these are indicators of

arterial stiffening that we are able to rigorously quantify with our biaxial mechanical tests.

Increased carotid intima-media thickness (cIMT) is also a marker of subclinical atherosclerosis that has been observed in HIV positive patients. Lorenz et al. found that HIV positive patients had increased cIMT as compared to control patients matched for traditional risk factors, but also that HAART treated patients had a 24.8% larger value for the carotid bifurcation intima-media thickness than the HAART naïve patients.(70) The larger effect of HAART therapy in bifurcation region of the carotid is significant as this is the region most prone to atherosclerotic lesion formation. Additionally, the study found that NRTIs (such as AZT) had significant effects on the cIMT specifically with the carotid bifurcation 48.1% or 28% higher in patients who had been on an NRTI for less than 1 year or more than 2 years respectively as compared to patients who had never received an NRTI. As with arterial stiffening, our studies also showed increased intima-media thickness (IMT) in the AZT mice as compared to the control group (Figure 5.6). This finding was confirmed both with histological preparation of unloaded vessels and confocal microscopy of vessels in their loaded physiological state. The confocal images also let us quantify advential thickness, a parameter that is not able to be determined clinically. Interestingly, we observed advential thinning in the AZT mice for both the aortas and carotids. This change is the opposite of the advential thickening observed in aim 2 in the HIV Tg mice, indicating that while both the viral proteins and AZT have the same overall (and clinically observable effects) or arterial stiffening and intima-media thickening, the two groups may have different ECM and cellular level effects.

The use of a mouse model to study the effects of AZT allowed us to not only isolate the drug from the influence of HIV infection or other lifestyle and risk factors present in clinical studies, but we also were able to study a number of parameters that are not clinically tractable. Beyond analyzing the circumferential behavior, where we found arterial stiffening as observed clinically, our rigorous mechanical testing protocols also investigated the axial behavior. While carotids did not exhibit changes in axial behavior, the aortas from the AZT treated mice had lower axial forces at both *in vivo* and subphysiological stretches at pressures from 10-70 and 10-80 mmHg respectively (Figure 5.4). Differences in axial behavior are interesting to note since we know that vessels to respond to changes in axial loads. (103, 176, 177) Another mechanical property we characterized that cannot be determined clinically is opening angle as a measure of residual stress. Interestingly, we did not see differences in the opening angles between the two groups (Figure 5.5), indicating the vessels were able to maintain the same distribution of residual stress despite undergoing remodeling that resulted in changes in circumferential stiffness and intima-media thickness.

The vascular remodeling, which is responsible for the observed stiffening and thickening, is a complex process which involves both the synthesis and degradation of key ECM proteins specifically collagen and elastin. In our studies we found a decrease in elastin content in the carotids from the AZT treated mice (Figure 5.8). This decrease in elastin content is in agreement with the observed arterial stiffening. Additionally, loss of functional elastin is associated with a number of vascular diseases specifically aging, aneurysm development, and atherosclerosis. (166, 167) Zymography was used to determine the activity of proteases within the wall, specifically cathepsins. Changes in

cathepsin regulation have been associated with atherosclerosis. Cathepsins are potent elastases and collagenases and thus their activity can lead to degradation of the proteins within the wall and ECM remodeling. The observed upregulation of cathepsin L (Figure 5.9 A) in the carotids is in good agreement with literature where cathepsins were detected in atherosclerotic lesions (168). Additionally, we found a decrease in cathepsin V activity in the aortas, which we also saw in the HIV Tg mice in aim 1 (Figure 5.9 B and Figure 4.6). The reason for this downregulation is not clear from the literature but the observation in both the HIV Tg and AZT mice indicates that same sort of conserved signaling mechanism is causing this dysregulation of cathepsin activity. The effects of this decrease and possible mechanisms responsible merit further studies. However, the result does seem in-line with preliminary data collected by others in the lab analyzing cathepsin activity from monocytes in the blood of HIV patients, which seems to point to antiretroviral therapy potentially decreasing cathepsin activity.

In summary, the antiretroviral drug AZT (an NRTI) has a number proatherogenic effects on the vasculature including arterial stiffening and carotid intima-media thickening. While a number of antiretroviral drugs including NRTIs have been implicated in leading to the development of atherosclerosis (70, 76), determining the specific role that the medications or a specific medication plays in disease development is difficult since many patients have a number of confounding risk factors. Thus this aim used a mouse model to determine the isolated effects of AZT on otherwise healthy mice. We found that the mice did indeed exhibit the subclinical markers of atherosclerosis observed in patients, and additionally, we were able to study other changes that are not able to determined clinically. These included changes in advential thickness, elastin

quantity, and protease activity. Thus, the model serves as a good foundation for future studies to further investigate the AZT mitigated changes as well as to begin to investigate the changes due to the administration of one of the other drug classes.

## CHAPTER 6

### SUMMARY, LIMITATIONS, AND FUTURE CONSIDERATIONS

#### 6.1 Summary

The overall objective of this project was to characterize the mechanical behavior of murine arteries through the development of constitutive models that incorporate microstructure and a number of experimentally tractable parameters as well as to employ mouse models to characterize preclinical markers of atherosclerosis induced by HIV or antiretroviral drugs. While clinical data supported the hypotheses that both the virus and HAART drugs have proatherogenic effects, there still remained a need to isolate the effects of each in a controlled manner; thus this work used murine models to separately study the effects of the viral proteins or antiretroviral drug AZT on the arteries. The primary focus was on mechanical and structural changes specifically investigating stiffening and thickening, two subclinical markers of atherosclerosis.

The constituents that constitute arteries (e.g., collagen, elastin, smooth muscle cells), along with their geometry and applied loads, determine the local mechanical environment in which cells, the mediators of growth and remodeling, live. It is clear that cell-mediated tissue growth and remodeling occurs in response to changes in their local mechanical environment and, conversely, changes in microstructural content and organization, geometry, and applied loads change the local mechanical environment, thereby initiating tissue growth and remodeling. For example in Aims 2 and 3, we observed significant changes in the content and organization of collagen and elastin, in parallel with significant changes in geometry and the biomechanical response of common carotid arteries and aorta, in response to expression of HIV proteins or treatment with

AZT. The goal of Aim 1 was to develop microstructurally based constitutive models that integrate changes at the microstructural level with changes at the tissue level to describe and predict arterial behavior. We showed that the rule-of-mixtures models based on constrained mixture theory simulated the mechanical responses as good as phenomenological models and the implementation of the penalties ensured the constituent each had significant physiological contributions. Finally, the models developed in aim 1 will be able to incorporate some of the structural parameters from the last two aims in future work.

Aim 2 investigated the role of HIV proteins using a transgenic mouse model in which the mice contained transgene for the HIV-1 proteins *env*, *tat*, *nef*, *rev*, *vif*, *vpr*, and *vpu*. The effects of AZT, a NRTI antiretroviral, were studied in aim 3 by administering the drug to healthy mice via oral gavage. In both aims, we observed increased circumferential arterial stiffness in both the aortas and carotids for the HIV Tg and AZT treated mice. Similarly, both the HIV Tg and AZT treated mice had increased intima-media thickening as determined by both histology and confocal imaging. Thus, we conclude that both the HIV viral proteins and the antiretroviral AZT may contribute to the development of cardiovascular disease in patients as evidenced by the observed subclinical markers of atherosclerosis.

The use of an animal model allowed to us to further investigate the arterial changes to study aspects not clinically quantifiable. The biaxial mechanical tests included force measurements in addition to the pressure-diameter relations that were used to observe arterial stiffening. No differences were found in the axial behavior of the HIV Tg mice in aim 2 except at very low pressures or stretches never seen physiologically.

The aortas from the AZT treated mice in aim 3, however, did have differing axial behavior with the AZT mice having decreased axial forces at pressures of up to 80 mmHg during the pressure-diameter inflation tests. Additional, mechanics measurements also included quantifying residual stress by determining the opening angles of the vessels. The HIV Tg mice had greater opening angles than their wildtype littermates indicating greater residual stress, while the opening angles of the AZT mice were not different than the water control mice indicating residual stress was maintained during the arterial remodeling for that treatment.

In addition to the intima-media thickening, the confocal imaging techniques used in aims 2 and 3 allowed the quantification of the advential thickness as well. Interestingly we observed adventitial thickening in HIV Tg mice as compared to their controls while the adventia in the AZT mice was decreased compared to the control group. Thus, while the same clinically tractable trait of intima-media thickening was observed in both groups, the adventitial behavior was quite different. The confocal images of the collagen were also used to generate a distribution of fiber angles throughout the wall though no statically significant differences were observed in either of the two studies.

Vascular remodeling occurs as a result of the production and degradation of the proteins within the ECM which is comprised mainly of elastin and collagen. Thus upon observing remodeling at the mechanical and tissue structural level, we investigated the protein level changes in both aims 2 and 3 through the quantification of the collagen and elastin content as well as the protease activity. In both the HIV Tg and AZT treated mice we saw decreases in elastin content, providing further support to proatherogenic effects

by both stimuli. In the AZT mice the collagen content was not different than the control mice; however, in the HIV Tg mice there was a trend (albeit not significant at  $p < 0.05$ ) of increased collagen. This finding is particularly interesting as we also observed an increase in the advential thickness in these mice while the AZT mice had thinning.

Proteolytic degradation of the ECM components plays an important role in the vascular remodeling. This study focused on the cathepsin family of proteases, which have been implicated in atherosclerosis. In both aims 2 and 3 we saw changes in the activity levels of various proteins. In aim 2, we observed increases in cathepsin S activity and decreases in cathepsin V activity in the HIV Tg mice. While in aim 3, we observed increases in cathepsin L and once again decreases in cathepsin V. Thus while stimuli for the vascular changes are very different (viral proteins vs. an antiretroviral drug), protein level changes of decreased elastin and decreases cathepsin V activity are conserved. In general, the results from aims 2 and 3 showed the both HIV proteins and AZT have proatherogenic effects and likely contribute to cardiovascular disease in HIV patients.

## **6.2 Limitations**

While the incorporation of microstructure in the constitutive models in aim 1 improves upon previous work by providing more physical meaning to the parameters and allowing actual microstructural data to be incorporated into the model, the work of aim 1 does have a number of limitations due to various assumptions adopted when creating the models. First, the models assume a homogeneous mixture of the components (elastin, muscle, and collagen) throughout the wall, though we know that the arterial wall is composed of three distinct layers- intima, media, and adventia- with unique compositions in each. In particular we know that the adventia is primarily fibroblasts and

collagen and the media is concentric layers of smooth muscle cells and elastin with some collagen. The model however assumes these components are evenly distributed throughout the wall, but in the future as more data on the structural distribution is collected (i.e. collagen fiber angle distributions as in Aim 2 and 3) a heterogeneous model can be developed. Another fundamental assumption of the study was the use of a rule-of-mixtures approach which constrains the constituents must deform together and follow the motion of the tissue as a whole, though is not likely always entirely true. Additionally, the total stress of the vessel is modeled as the sum of the stresses of each individual constituent neglecting any interactions between constituents that may contribute to stress. It is very likely that the constituents do interact in ways that modulate stress, and as more mechanobiology studies quantify these interactions future work can incorporate them into the models. In general, since the model was developed prior to aims 2 and 3, the specific assumption of a homogeneous distribution within the wall limits the application of this model to the arteries studied in the last two aims as it is unable to incorporate the differential changes in layer thickness observed. While parameters could still be determined for these vessels, any conclusions drawn from the parameter values would be limited since they do not account for some of the known structural differences.

While the experimental work in the last two aims of this dissertation has provided many interesting insights into the isolated effects of HIV proteins and AZT on the arterial wall specifically demonstrating the clinically observed changes of arterial stiffening and increased intima-media thickening, the studies does have a number of limitations that must be kept in mind when drawing conclusions from the data. First, the mouse model used in aim 2 is non-infectious model of HIV. The HIV virus is specific to human cells

since it binds to the CD4 complex on the cell surface into order to enter the cells. The specificity of the virus makes infectious animal models difficult. Thus while the transgenic mouse used in aim 2 is non-infectious, it models the exposure of the vascular cells to viral proteins such as those circulating in the blood or released in by macrophages in the arterial wall. However, quantification of the levels of protein production (and thus exposure) in the vascular walls or blood of these mice would determine the exposure levels to the arteries. Bruggeman et al. showed that the transgene was expressed in high levels in muscle (likely skeletal muscle cells not vascular SMCs were used) but did not directly investigate arteries. (178) Additionally, the effects of HIV on the arteries are also thought to be associated with an inflammatory response causes by prolonged chronic infection by the virus. Thus, patients may have changes in immune cell counts and activation levels as well as higher levels of certain circulating cytokines and other inflammatory markers both of which are known to have negative effects on the vasculature. (72, 90) For example, circulating monocytes, one of the cell types that may be infected with the HIV virus in patients, are known to play an important role atherosclerotic plaque development through their adhesion and migration though the wall where they differentiate into macrophages and eventually foam cells. HIV infection and proteins activate the monocytes making them more susceptible to increased adhesion in addition to activating endothelial cells to express adhesion factors. (85, 86, 179) Histological analysis of the arteries in aim 2 however shows no evidence of monocyte adhesion or migration, thus indicating that the mouse model may not be replicating these inflammatory responses.

Another limitation was that the blood pressure of the HIV Tg mice in aim 2 was not measured during the study. However, Kopp et al. showed that the HIV Tg mice developed renal dysfunction and failure, which are both associated with hypertension, during a similar time course used in our study. (146) Therefore, there is a possibility that the HIV Tg mice might be hypertensive and the observed vascular remodeling may be response to that change rather than a direct effect of the proteins on the arterial wall. Currently, we are further evaluating the blood pressure and kidney function of the mice and comparison studies should be performed on the same transgenic model bred on a different background, which may have less pronounced changes in blood pressure and kidney function. However, regardless of whether the mechanisms behind the vascular changes we observed were due to direct effects of the viral proteins on vascular cells or systemic changes, the HIV Tg mice did have atherogenic changes due to the addition the viral proteins to otherwise healthy mice which implicates the virus's role the development of cardiovascular disease.

Aim 3 also had a number of limitations as well. First we only took the study out to 35 days, which is much shorter than both the duration that humans receive antiretroviral drugs as well the development of atherosclerosis in humans. However, a study by Shanker et al. showed endothelial dysfunction in only 4 weeks in healthy, HIV negative patients who were received the antiretroviral indinavir daily for that period, which is inline the time course of our study (91). Mice also have an accelerated normal lifespan compared to humans, reaching maturity around 6 weeks and living only a few years, making the time course of the study appropriate. Additionally, the dosage of AZT administered was approximately 10 times higher than the human dose. However, since

mice have a much higher metabolic rate compared to humans, a higher dosage is appropriate; specifically, the half life of AZT in the plasma of mice around 5 times less than that of humans (180). Additionally, the dosage and time course was previously published and thus our methods are in line with current work. (96, 181)

While our mice did exhibit subclinical markers of atherosclerosis in both of the second and third aims, the mice did not fully develop atherosclerosis and had no lesions. While we feel that the changes we observed were likely part of the disease development rather than some sort of healthy, adaptive remodeling, the observance of the accelerated development of actual atherosclerotic lesions would be insightful. Observing these changes, however, would likely require a change in the diet or mouse strain or both or much longer time course. Future work may include this, but the current work still revealed a number of pro-atherogenic changes in the mice while the control mice remained healthy.

Additionally, aim 3 only looked at one class of the antiretroviral drugs. Thus care should be taken to not over-generalize the results of the study to other drug class. However, NRTIs are included in almost all HAART regimens and have been implicated in CVD, which is why we focused this study on that class. Another possible limitation is that AZT is not commonly used in the United States today; however, the drug is still widely used in developing countries and thus still merits study. Careful, consideration must be given to discern whether the observed changes are specific to AZT or have wider implications to all NRTIs since they all prevent viral replication by the same mechanism.

### 6.3 Future Considerations

While the results of this dissertation are interesting in themselves, they also serve as a starting point for many more future studies. First, while the model developed in aim 1 does capture the microstructural behavior of the arteries, most of the structural measures and parameters are assumed or fit. However, using some of the techniques in the last two aims several of these structural measures could be measured and incorporated including collagen and elastin content and opening angles. Additionally, recent work in our lab has incorporated the average collagen fiber angles from the confocal images into the fiber distribution model. (156) Future models could take this one step further by implementing the different distributions throughout the arterial wall rather than an average distribution for the entire wall. Besides incorporating the differing collagen fiber angle distributions across the wall thickness, future models could also incorporate differing elastin and smooth muscle contents as well to create a more accurate heterozygous model of the wall. This heterozygous model would allow us to incorporate the changes we saw in the layer thickness (as determined by elastin and collagen confocal images) into the model and therefore determine more accurate and insightful parameters for the arteries in aims 2 and 3. A better understanding of the local stresses within the wall from a more accurate model could provide insight to help shape future experimental studies as well.

The agreement with clinical data, specifically arterial stiffening and thickening, helps to establish the two mouse models in aims 2 and 3 as good models for further study. Thus while this study focused mainly on several tissue level changes, the agreement with clinical data indicates their usefulness for future more biological and mechanistic studies.

One area that merits further investigation is smooth muscle cells. While we acknowledged that the primary structural components of muscle are collagen, elastin, and smooth muscle, the work focused primarily on the proteins, collagen and elastin. However, we know that smooth muscle cells play an important role in the arterial wall beyond structure and mechanics but in cell signaling and vascular remodeling as well. Specifically smooth muscle proliferation (e.g., intimal hyperplasia) is known to play a key role in the development of atherosclerosis (31, 165). Since the media layer is composed primarily of elastin and smooth muscle cells, the decrease in the elastin content but increase in intima-media thickness suggests that the increase in thickness might be attributed in part to increases in smooth muscle cell volume (not quantified). Further work should investigate changes to the smooth muscle cells in the tissue. A more careful histological analysis of smooth cells volume as a percentage of the total arterial wall will determine if there is an increase in smooth muscle cells. To determine if any changes are due to either proliferation versus hypertrophy, one possible study is measuring BrdU uptake in cells to determine if there are changes in smooth muscle cell proliferation in the HIV Tg or AZT treated mice.

While our studies observed some changes in cathepsin activity, the decrease in cathepsin V is a unique finding that merits further study. Previous studies have found that cathepsin S and K were found in the fibrous cap, foam cells, and adjacent to SMCs in atherosclerotic vessels (37, 38). Additionally, stimulation of smooth muscles cells with various cytokines induced cathepsin S production and degradation of elastin, and cathepsin S-deficient monocytes are not able to migrate through membranes containing an endothelial monolayer, collagen, and SMCs. (38, 39) Our findings did support these

studies with upregulation of cathepsin S and L; however, we also saw a decrease in cathepsin V in both the HIV Tg mice and AZT mice. This results is interesting since it appears to be counterintuitive compared to the current literature. However, some preliminary work by our lab investigating cathepsin activity in white blood cells in blood from patients on ART seems to support a decrease in cathepsin activity. Nevertheless, far less information on cathepsin V and atherosclerosis exists in literature, and thus this area deserves further investigation. Possible studies include *in vitro* work to try to determine the signaling mechanisms responsible for the changes in cathepsin V expression as well as the effects that decreased cathepsin V is having on the vascular cells. In addition to cathepsins, quantification of other proteases associated with atherosclerosis, specifically MMPs, would provide insight into the proteolytic remodeling in the arteries. These further investigations of the protease activity may provide insight into possible therapeutics to mitigate the effects of the HIV proteins and AZT.

Also, now that we have shown that the viral proteins and AZT have significant effects on the vasculature that lead to arterial stiffening and thickening, returning to *in vitro* cell work to investigate the signaling pathways and mechanisms might be useful to more closely investigate some of the changes observed in our mouse studies including cathepsin upregulation and changes in gene expression of various ECM proteins. Once more specific pathways for these changes have been determined the mouse models could be used as models to test potential therapeutics to try to either mitigate some of the negative effects of AZT (or other drugs) or prevent harm induced by the viral proteins.

Both the HIV Tg and AZT treated mice developed vascular changes consistent with subclinical atherosclerosis observed in patients. However, the studies performed did

not focus on capturing a number of other characteristics of HIV patients that may be associated with the development of the observed vascular remodeling. Specifically, HIV patients are known to have systemic chronic inflammation as evidenced by increases in a number of cytokines and inflammatory markers in the plasma. Future work could quantify these markers such as those in a study by Calmy et al. in the plasma from the mice. (90) Additionally, immune cells in the mice were not investigated, but future work could determine if the mice exhibit immune cell activation or senescence as observed in patients. Finally, while aim 3 briefly quantified a plasma cholesterol and triglyceride levels, future work could expand this investigation of dyslipidemia to both the HIV Tg and AZT mice, to quantify HDL and LDL levels, and to increase the sample size. All of this work will help to determine whether the mice exhibit systemic changes associated with HIV patients in addition to the vascular changes.

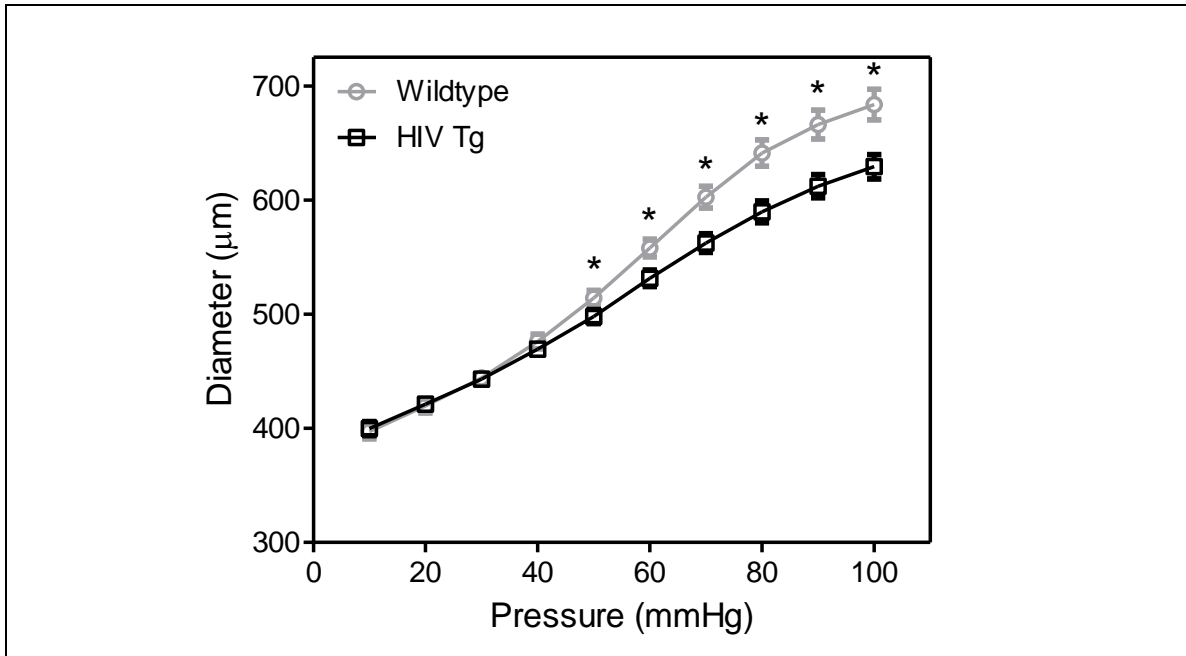
While the primary focus of this body of work was changes to the vasculature indicative of atherosclerosis, another interesting area of study would be related more to the cardiac function of CVD. Specifically studies that assess ventricular size and ejection fraction may be useful to assess heart health and potential problems mediated by either the HIV proteins or antiretroviral drugs. Additional interesting work might include assess the hearts recovery capability to induced simulated heart attacks, which may provide insight into whether HIV patients are not only more prone to myocardial infarctions but also have a poorer prognosis following the event.

As previously addressed one limitation to this study is that the mice did not fully develop vascular disease, specifically atherosclerotic plaques, in the time course of the study. This was likely due to the fact that they were on normal mouse feed diets rather

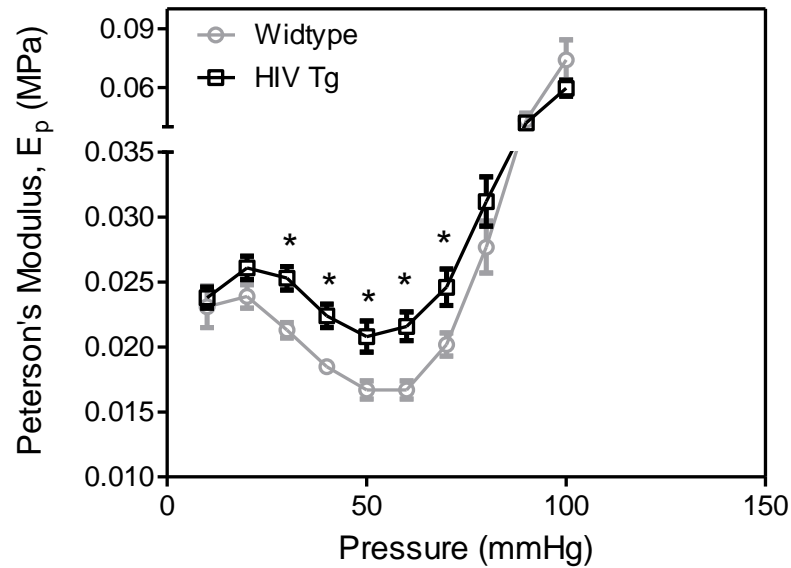
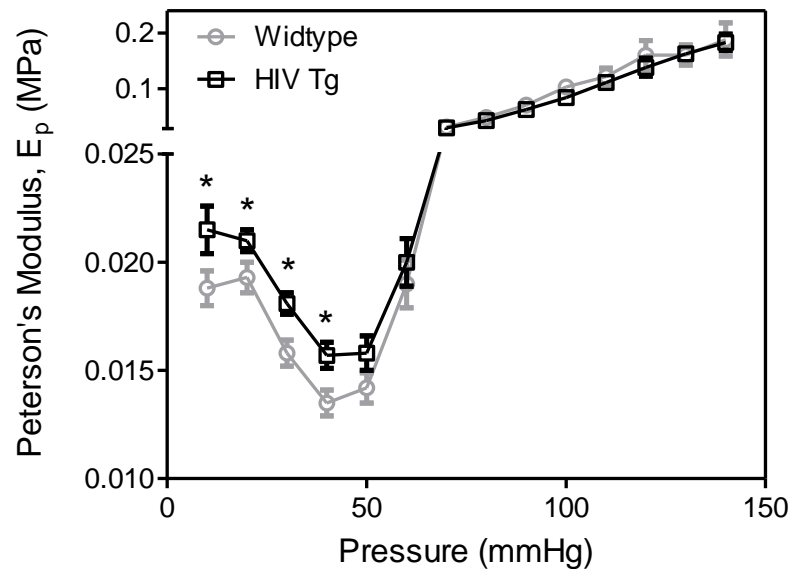
than a high fat diet which might more closely mimic diets of human patients that develop CVD. Thus future studies using these same mouse models but administering a high fat diet to the mice might induce the formation of atherosclerotic plaques and allow the study of the full progression of the disease and the roles of HIV proteins and AZT. Another option would be to conduct these tests in ApoE<sup>-/-</sup> mice. This knockout model is often used in atherosclerosis studies as the absence of the ApoE protein increases plasma cholesterol levels and leads to the development of fatty streaks and lesions.(182) Additional measurements that would be important to collect in these studies would be measurements of serum lipid levels including cholesterol and triglycerides. Dyslipidemia has been shown to occur in HIV patients and thus not only might these studies produce a more complete picture of plaque development but they may also provide insights into the roles that the viral proteins and drugs play in that syndrome.

The models and tests performed in this study might also be applied to investigate other classes of the antiretroviral drugs. This would be helpful in confirming and quantifying the suggestions in clinical literature that some classes of drugs have more deleterious effects on the vascular than others. The implications of this work are that if it is known that certain drug classes (or drugs in particular) are more harmful than others in terms of cardiovascular health, treatment regimens can be optimized to try to balance good control of HIV replication with maintaining cardiovascular health.

## APPENDIX A: CHAPTER 4 ADDITIONAL PLOTS



**Figure A.1: HIV-1 protein expression increases arterial stiffness in carotids at a subphysiological stretch.** Mechanical testing was used to investigate the biomechanics of carotid arteries. The results of the pressure-diameter mechanical tests at the subphysiological stretch of 1.4 show increased stiffness in the HIV Tg carotids in agreement with the results at physiological stretch in Figure 4.1. (\* indicates  $p < 0.05$ ,  $N=6$ , and data is mean  $\pm$  SEM)

**A****B**

**Figure A.2: HIV-1 protein expression increases modulus (stiffness) in carotids at subphysiological and superphysiological stretches.** Mechanical testing was used to investigate the biomechanics of carotid arteries. Peterson's modulus,  $E_p$ , of the vessels was used to normalize for differences in vessel geometry. The results at both subphysiological ( $\lambda=1.4$ ) and superphysiological ( $\lambda=1.9$ ) stretches show increased moduli in the HIV Tg carotids in agreement with the results at physiological stretch in Figure 4.1. (\* indicates  $p < 0.05$ ,  $N=9$ , and data is mean  $\pm$  SEM)

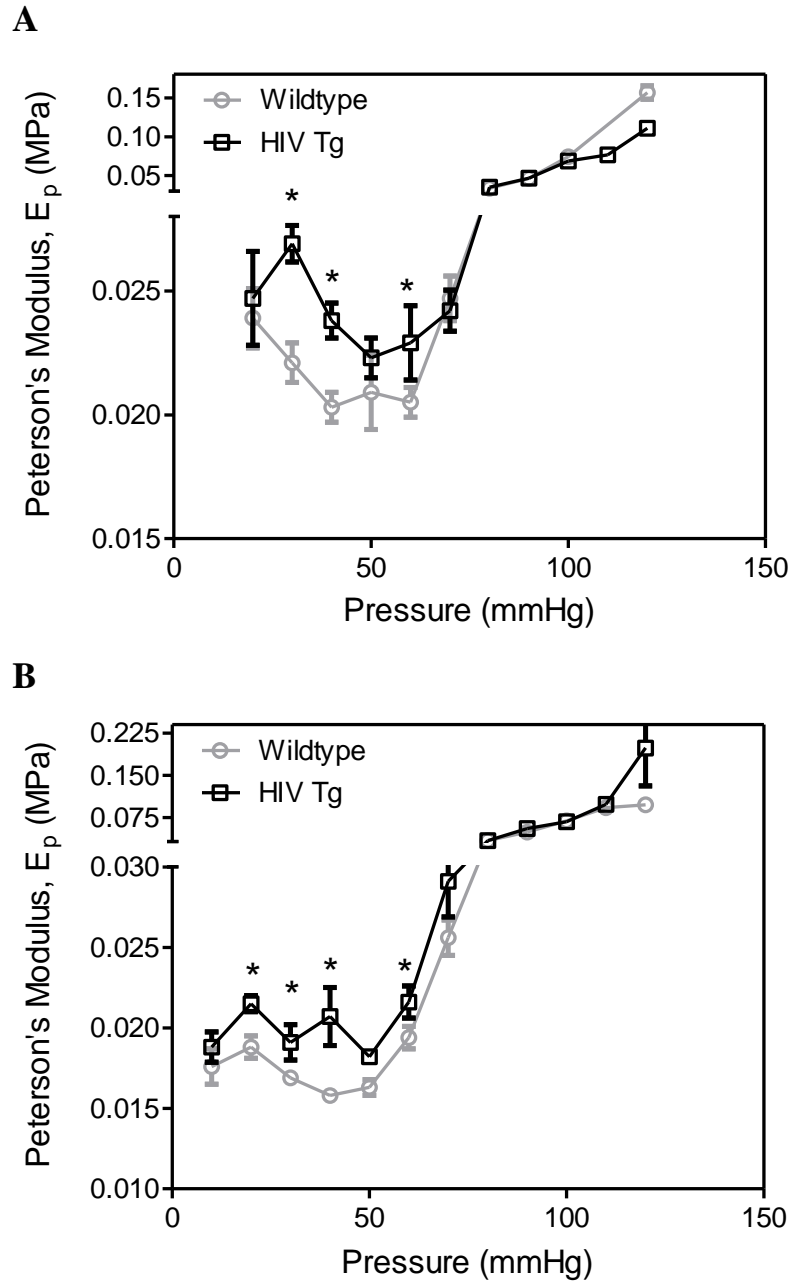


**Figure A.3: HIV-1 protein expression increases modulus (stiffness) in aortas at subphysiological and superphysiological stretches.** Mechanical testing was used to investigate the biomechanics of aortas arteries. Peterson's modulus,  $E_p$ , of the vessels was used to normalize for differences in vessel geometry. The results at both subphysiological ( $\lambda=1.4$ ) and superphysiological ( $\lambda=1.9$ ) stretches show increased moduli in the HIV Tg aortas in agreement with the results at physiological stretch in Figure 4.1. (\* indicates  $p < 0.05$ ,  $N=9$ , and data is mean  $\pm$  SEM)

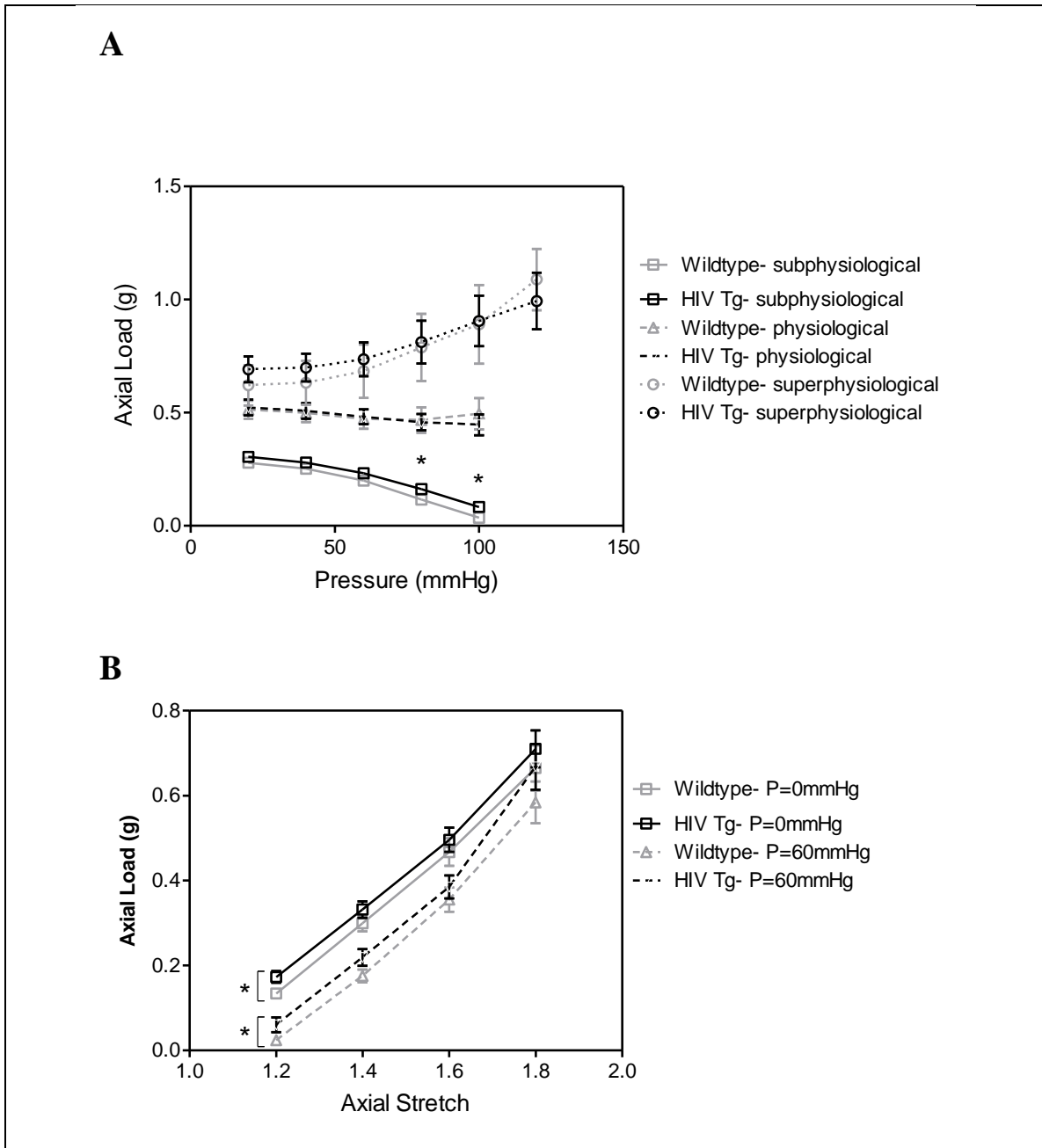


**Figure A.4: Axial behavior at physiologically relevant load is not different between carotids from HIV Tg and wildtype mice.** Mechanical testing was also used to investigate the axial biomechanics of carotid arteries. Panel A shows the axial loads during pressure-diameter tests and the only differences are observed at subphysiological stretches. Panel B is the results of the force-length tests with the only difference occur low stretches and low pressures. (\* indicates  $p < 0.05$ ,  $N=9$ , and data is mean  $\pm$  SEM)

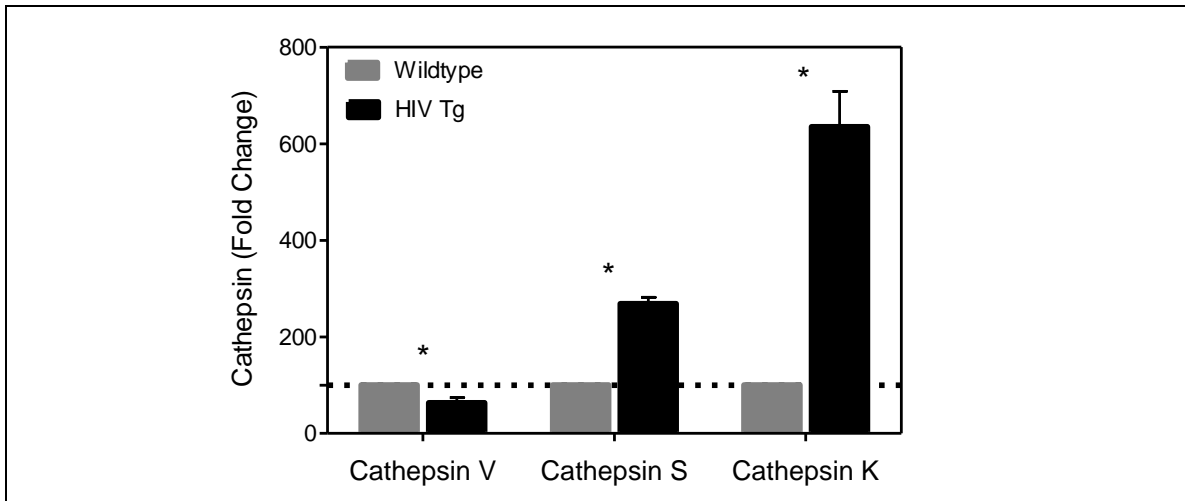


**Figure A.4: Aortas from mice HIV Tg mice have increased cathepsin S and K and decreased cathepsin V activity.** Cathepsin activity in the arterial wall was determined using zymography and densitometry to quantify the changes. The results of the densitometry found increases in cathepsin S and K activity in the HIV Tg aortas, but a decrease in cathepsin V. These results were similar to those of the carotids in figure 4.7. (\* indicates  $p < 0.05$   $N=5$  ( $N=3$  for cathepsin S and L) and data is mean  $\pm$  SEM) (Note: data was collected by Ivana Parker)

## APPENDIX B: CHAPTER 5 ADDITIONAL PLOTS

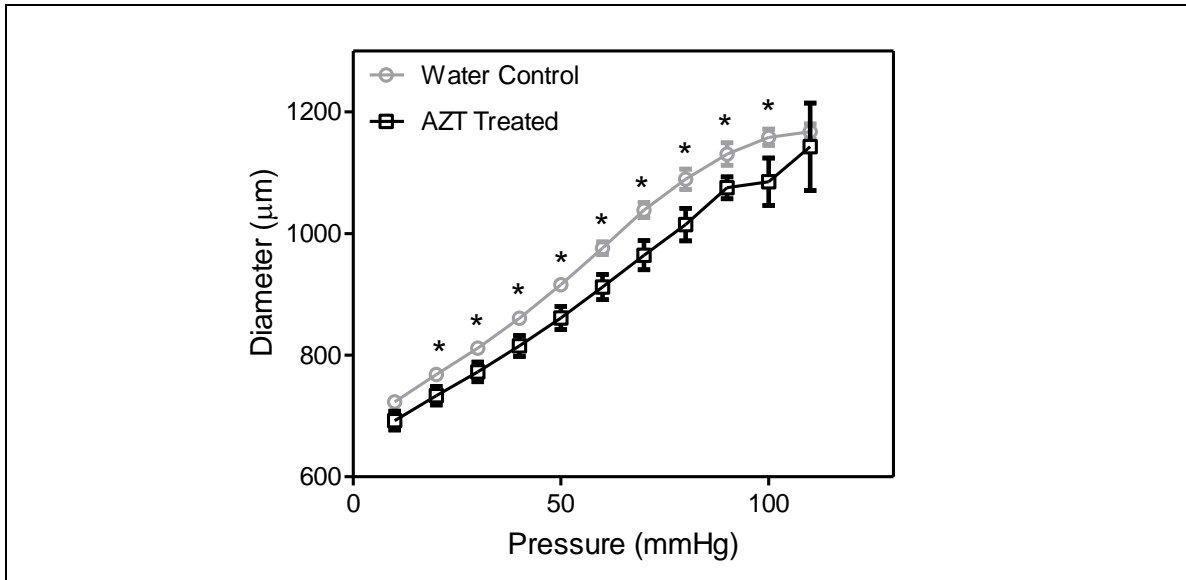


**Figure B.1: AZT treatment increases arterial stiffness in aortas at a subphysiological stretch.** Mechanical testing was used to investigate the biomechanics of aortas. The results of the pressure-diameter mechanical tests at the subphysiological stretch of 1.4 show increased stiffness in the AZT treated aortas in agreement with the results at physiological stretch in Figure 5.3. (\* indicates  $p < 0.05$ ,  $N=8$ , and data is mean  $\pm$  SEM)

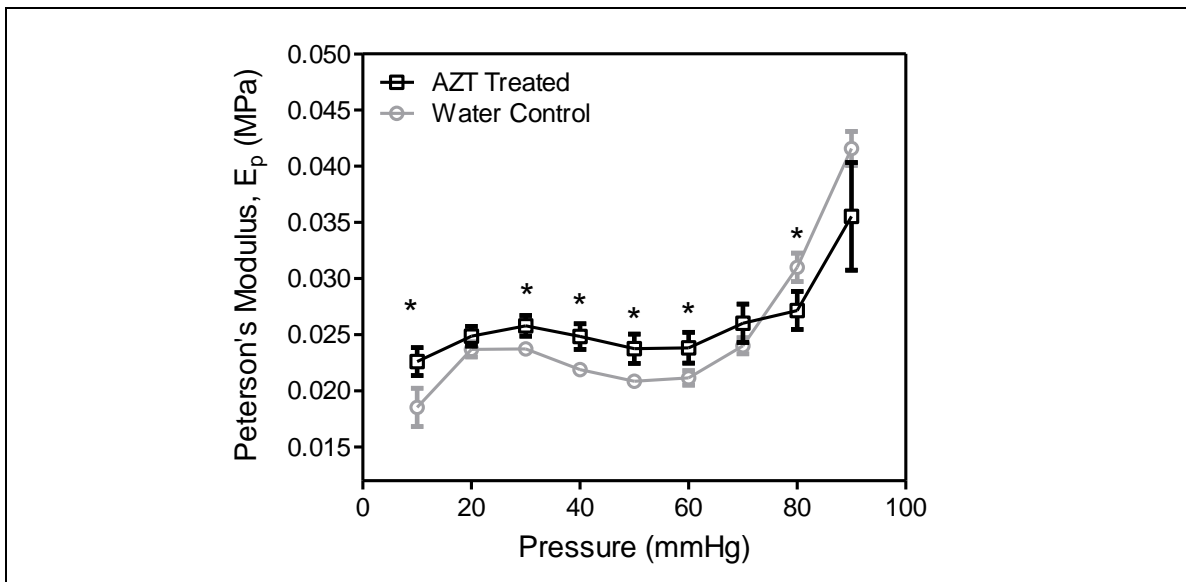


**Figure B.2: AZT treatment increases arterial stiffness in aortas at a subphysiological stretch.** Mechanical testing was used to investigate the biomechanics of aortas and Peterson's Modulus, a measure of arterial stiffness, was calculated from the pressure-diameter data. At subphysiological stretch of 1.4, the aortas in the AZT treated mice showed increased stiffness in agreement with the results at physiological stretch in Figure 5.3. (\* indicates  $p < 0.05$ ,  $N=8$ , and data is mean  $\pm$  SEM)

## REFERENCES

1. USAID. 2008 Report on the global AIDS epidemic. 2008.
2. Currier JS, Taylor A, Boyd F, Dezii CM, Kawabata H, Burtcel B, et al. Coronary heart disease in HIV-infected individuals. *J Acquir Immune Defic Syndr*. 2003;33(4):506-12.
3. Mary-Krause M, Cotte L, Simon A, Partisani M, Costagliola D. Increased risk of myocardial infarction with duration of protease inhibitor therapy in HIV-infected men. *AIDS*. 2003;17(17):2479-86.
4. Friis-Moller N, Sabin CA, Weber R, d'Arminio Monforte A, El-Sadr WM, Reiss P, et al. Combination antiretroviral therapy and the risk of myocardial infarction. *N Engl J Med*. 2003;349(21):1993-2003.
5. Maggi P, Lillo A, Perilli F, Maserati R, Chirianni A. Colour-Doppler ultrasonography of carotid vessels in patients treated with antiretroviral therapy: a comparative study. *AIDS*. 2004;18(7):1023-8.
6. Meng Q, Lima JA, Lai H, Vlahov D, Celentano DD, Strathdee SA, et al. Coronary artery calcification, atherogenic lipid changes, and increased erythrocyte volume in black injection drug users infected with human immunodeficiency virus-1 treated with protease inhibitors. *Am Heart J*. 2002;144(4):642-8.
7. Kaplan RC, Kingsley LA, Sharrett AR, Li X, Lazar J, Tien PC, et al. Ten-year predicted coronary heart disease risk in HIV-infected men and women. *Clin Infect Dis*. 2007;45(8):1074-81.
8. van Vonderen MGA, Hassink EAM, van Agtmael MA, Stehouwer CDA, Danner SA, Reiss P, et al. Increase in Carotid Artery Intima-Media Thickness and Arterial Stiffness but Improvement in Several Markers of Endothelial Function after Initiation of Antiretroviral Therapy. *J Infect Dis*. 2009;199(8):1186-94.
9. Oliviero U, Bonadies G, Apuzzi V, Foggia M, Bosso G, Nappa S, et al. Human immunodeficiency virus per se exerts atherogenic effects. *Atherosclerosis*. 2009;204(2):586-9.
10. Hsue PY, Lo JC, Franklin A, Bolger AF, Martin JN, Deeks SG, et al. Progression of atherosclerosis as assessed by carotid intima-media thickness in patients with HIV infection. *Circulation*. 2004;109(13):1603-8.
11. Mercie P, Thiebaut R, Aurillac-Lavignolle V, Pellegrin JL, Yvorra-Vives MC, Cipriano C, et al. Carotid intima-media thickness is slightly increased over time in HIV-1-infected patients. *HIV Med*. 2005;6(6):380-7.

12. McComsey GA, O'Riordan M, Hazen SL, El-Bejjani D, Bhatt S, Brennan ML, et al. Increased carotid intima media thickness and cardiac biomarkers in HIV infected children. *AIDS*. 2007;21(8):921-7.
13. Hsue PY, Hunt PW, Schnell A, Kalapus SC, Hoh R, Ganz P, et al. Role of viral replication, antiretroviral therapy, and immunodeficiency in HIV-associated atherosclerosis. *AIDS*. 2009;23(9):1059-67. PMID: 2691772.
14. Bonnet D, Aggoun Y, Szezepanski I, Bellal N, Blanche S. Arterial stiffness and endothelial dysfunction in HIV-infected children. *AIDS*. 2004;18(7):1037-41.
15. Sevastianova K, Sutinen J, Westerbacka J, Ristola M, Yki-Jarvinen H. Arterial stiffness in HIV-infected patients receiving highly active antiretroviral therapy. *Antivir Ther*. 2005;10(8):925-35.
16. Hsue PY, Hunt PW, Wu Y, Schnell A, Ho JE, Hatano H, et al. Association of abacavir and impaired endothelial function in treated and suppressed HIV-infected patients. *AIDS*. 2009;23(15):2021-7. PMID: 2785446.
17. Blanco JJ, Garcia IS, Cerezo JG, de Rivera JM, Anaya PM, Raya PG, et al. Endothelial function in HIV-infected patients with low or mild cardiovascular risk. *J Antimicrob Chemother*. 2006;58(1):133-9.
18. Grubb JR, Dejam A, Voell J, Blackwelder WC, Sklar PA, Kovacs JA, et al. Lopinavir-ritonavir: effects on endothelial cell function in healthy subjects. *J Infect Dis*. 2006;193(11):1516-9.
19. Torriani FJ, Komarow L, Parker RA, Cotter BR, Currier JS, Dube MP, et al. Endothelial function in human immunodeficiency virus-infected antiretroviral-naive subjects before and after starting potent antiretroviral therapy: The ACTG (AIDS Clinical Trials Group) Study 5152s. *J Am Coll Cardiol*. 2008;52(7):569-76. PMID: 2603599.
20. Teixeira HN, Mesquita ET, Ribeiro ML, Bazin AR, Mesquita CT, Teixeira MP, et al. Study of vascular reactivity in HIV patients whether or not receiving protease inhibitor. *Arq Bras Cardiol*. 2009;93(4):367-73, 0-6.
21. Chuong CJ, Fung YC. ON RESIDUAL-STRESSES IN ARTERIES. *J Biomech Eng-Trans ASME*. 1986;108(2):189-92.
22. Lanir Y. CONSTITUTIVE-EQUATIONS FOR FIBROUS CONNECTIVE TISSUES. *Journal of Biomechanics*. 1983;16(1):1-12.
23. Holzapfel GA, Gasser TC, Ogden RW. A new constitutive framework for arterial wall mechanics and a comparative study of material models. *Journal of Elasticity*. 2000;61(1-3):1-48.
24. Medical physiology : a cellular and molecular approach. 2nd ed., International ed. ed. Boron WF, Boulpaep EL, editors. Philadelphia, PA :: Saunders/Elsevier; 2009.

25. Humphrey J. Cardiovascular solid mechanics : cells, tissues, and organs. New York: Springer; 2002.
26. Members WG, Roger VL, Go AS, Lloyd-Jones DM, Benjamin EJ, Berry JD, et al. Heart Disease and Stroke Statistics—2012 Update. *Circulation*. 2012;125(1):e2-e220.
27. Libby P. Inflammation in atherosclerosis. *Nature*. 2002;420(6917):868-74.
28. Kadar A, Glasz T. Development of atherosclerosis and plaque biology. *Cardiovascular Surgery*. 2001;9(2):109-21.
29. Conway DE, Williams MR, Eskin SG, McIntire LV. Endothelial cell responses to atheroprone flow are driven by two separate flow components: low time-average shear stress and fluid flow reversal. *Am J Physiol-Heart Circul Physiol*. 2010;298(2):H367-H74.
30. Ku DN, Giddens DP, Zarins CK, Glagov S. PULSATILE FLOW AND ATHEROSCLEROSIS IN THE HUMAN CAROTID BIFURCATION - POSITIVE CORRELATION BETWEEN PLAQUE LOCATION AND LOW AND OSCILLATING SHEAR-STRESS. *Arteriosclerosis*. 1985;5(3):293-302.
31. Doran AC, Meller N, McNamara CA. Role of Smooth Muscle Cells in the Initiation and Early Progression of Atherosclerosis. *Arterioscler Thromb Vasc Biol*. 2008;28(5):812-9.
32. Libby P. Vascular biology of atherosclerosis: Overview and state of the art. *Am J Cardiol*. 2003;91(3):3A-6A.
33. Rudijanto A. The role of vascular smooth muscle cells on the pathogenesis of atherosclerosis. *Acta Med Indones*. 2007;39(2):86-93.
34. Ross R. THE PATHOGENESIS OF ATHEROSCLEROSIS - A PERSPECTIVE FOR THE 1990S. *Nature*. 1993;362(6423):801-9.
35. Napoli C, Lerman LO. Involvement of oxidation-sensitive mechanisms in the cardiovascular effects of hypercholesterolemia. *Mayo Clinic Proceedings*. 2001;76(6):619-31.
36. Maytin M, Leopold J, Loscalzo J. Oxidant stress in the vasculature. *Current atherosclerosis reports*. 1999;1(2):156-64.
37. Garcia-Touchard A, Henry TD, Sangiorgi G, Spagnoli LG, Maurillo A, Conover C, et al. Extracellular proteases in atherosclerosis and restenosis. *Arterioscler Thromb Vasc Biol*. 2005;25(6):1119-27.
38. Sukhova GK, Shi GP, Simon DI, Chapman HA, Libby P. Expression of the elastolytic cathepsins S and K in human atheroma and regulation of their production in smooth muscle cells. *Journal of Clinical Investigation*. 1998;102(3):576-83.

39. Liu J, Sukhova GK, Sun J-S, Xu W-H, Libby P, Shi G-P. Lysosomal Cysteine Proteases in Atherosclerosis. *Arteriosclerosis, Thrombosis, and Vascular Biology*. 2004;24(8):1359-66.
40. 2008 Report on the global AIDS epidemic: UNAIDS; 2008 Contract No.: Document Number|.
41. Levy JA. PATHOGENESIS OF HUMAN-IMMUNODEFICIENCY-VIRUS INFECTION. *Microbiol Rev*. 1993;57(1):183-289.
42. Frankel AD, Young JAT. HIV-1: Fifteen proteins and an RNA. *Annual Review of Biochemistry*. 1998;67:1-25.
43. Scourfield A, Waters L, Nelson M. Drug combinations for HIV: what's new? *Expert Rev Anti-Infect Ther*. 2011;9(11):1001-11.
44. Maltez F, Doroana M, Branco T, Valente C. Recent advances in antiretroviral treatment and prevention in HIV-infected patients. *Current opinion in HIV and AIDS*. 2011;6 Suppl 1:S21-30.
45. Guidelines for the Use of Antiretroviral Agents in HIV-1-Infected Adults and Adolescents: Panel on Antiretroviral Guidelines for Adults and Adolescents, Services DoHaH; 2009 December 1, 2009 Contract No.: Document Number|.
46. Warnke D, Barreto J, Temesgen Z. Antiretroviral drugs. *Journal of Clinical Pharmacology*. 2007;47(12):1570-9.
47. Hogg R, Lima V, Sterne JAC, Grabar S, Battegay M, Bonarek M, et al. Life expectancy of individuals on combination antiretroviral therapy in high-income countries: a collaborative analysis of 14 cohort studies. *Lancet*. 2008;372(9635):293-9.
48. Smit C, Geskus R, Walker S, Sabin C, Coutinho R, Porter K, et al. Effective therapy has altered the spectrum of cause-specific mortality following HIV seroconversion. *Aids*. 2006;20(5):741-9.
49. Llibre JM, Falco V, Tural C, Negredo E, Pineda JA, Munoz J, et al. The Changing Face of HIV/AIDS in Treated Patients. *Curr HIV Res*. 2009;7(4):365-77.
50. Marston B, Miller B. Tuberculosis: the elephant in the AIDS clinic? *Aids*. 2006;20(9):1323-5.
51. Elzi L, Schlegel M, Weber R, Hirschel B, Cavassini M, Schmid P, et al. Reducing tuberculosis incidence by tuberculin skin testing, preventive treatment, and antiretroviral therapy in an area of low tuberculosis transmission. *Clinical Infectious Diseases*. 2007;44(1):94-102.

52. Gatanaga H, Yasuoka A, Kikuchi Y, Tachikawa N, Oka S. Influence of prior HIV-1 infection on the development of chronic hepatitis B infection. *European Journal of Clinical Microbiology & Infectious Diseases*. 2000;19(3):237-9.
53. Shire NJ, Welge JA, Sherman KE. Response rates to pegylated interferon and ribavirin in HCV/HIV coinfection: a research synthesis. *Journal of Viral Hepatitis*. 2007;14(4):239-48.
54. Patel P, Hanson DL, Sullivan PS, Novak RM, Moorman AC, Tong TC, et al. Incidence of types of cancer among HIV-Infected persons compared with the general population in the United States, 1992-2003. *Annals of Internal Medicine*. 2008;148(10):728-U29.
55. Shelburne SA, III, Hamill RJ. The immune reconstitution inflammatory syndrome. *AIDS Reviews*. 2003;5(2):67-79.
56. French MA. Disorders of immune reconstitution in patients with HIV infection responding to antiretroviral therapy. *Current HIV/AIDS reports*. 2007;4(1):16-21.
57. Martinez JV, Mazziotti JV, Efron ED, Bonardo P, Jordan R, Sevlever G, et al. Immune reconstitution inflammatory syndrome associated with PML in AIDS: A treatable disorder. *Neurology*. 2006;67(9):1692-4.
58. Sacktor N, McDermott MP, Marder K, Schifitto G, Selnes OA, McArthur JC, et al. HIV-associated cognitive impairment before and after the advent of combination therapy. *Journal of Neurovirology*. 2002;8(2):136-42.
59. Ristig M, Drechsler H, Powderly WG. Hepatic steatosis and HIV infection. *Aids Patient Care and Stds*. 2005;19(6):356-65.
60. Brown TT, Qaqish RB. Antiretroviral therapy and the prevalence of osteopenia and osteoporosis: a meta-analytic review. *Aids*. 2006;20(17):2165-74.
61. Quimby D, Brito MO. Fanconi syndrome associated with use of tenofovir in HIV-infected patients: a case report and review of the literature. *The AIDS reader*. 2005;15(7):357-64.
62. Martinez E, Larrousse M, Gatell JM. Cardiovascular disease and HIV infection: host, virus, or drugs? *Current Opinion in Infectious Diseases*. 2009;22(1):28-34.
63. Masia M, Padilla S, Bernal E, Almenar MV, Molina J, Hernandez I, et al. Influence of antiretroviral therapy on oxidative stress and cardiovascular risk: A prospective cross-sectional study in HIV-Infected patients. *Clinical Therapeutics*. 2007;29(7):1448-55.
64. Currier J, Taylor A, Boyd F, Kawabata H, Maa J, Dezii C, et al. Coronary heart disease in HIV-infected individuals: associations with antiretroviral therapy. *Antiviral Therapy*. 2002;7(3):L37-L.

65. Mary-Krause M, Cotteb L, Simon A, Partisani M, Costagliola D, Clinical Epidemiology Grp French H. Increased risk of myocardial infarction with duration of protease inhibitor therapy in HIV-infected men. *Aids*. 2003;17(17):2479-86.
66. Friis-Møller N, Weber R, Reiss P, Thiébaud R, Kirk O, Monforte AdA, et al. Cardiovascular disease risk factors in HIV patients - association with antiretroviral therapy. Results from the DAD study. *Aids*. 2003;17(8):1179-93.
67. Maggi P, Lillo A, Perilli F, Maserati R, Chirianni A, Grp P. Colour-Doppler ultrasonography of carotid vessels in patients treated with antiretroviral therapy: a comparative study. *Aids*. 2004;18(7):1023-8.
68. Kaplan RC, Kingsley LA, Sharrett AR, Li XH, Lazar J, Tien PC, et al. Ten-year predicted coronary heart disease risk in HIV-infected men and women. *Clinical Infectious Diseases*. 2007;45(8):1074-81.
69. Meng QY, Lima JAC, Lai H, Vlahov D, Celentano DD, Strathdee SA, et al. Coronary artery calcification, atherogenic lipid changes, and increased erythrocyte volume in black injection drug users infected with human immunodeficiency virus-1 treated with protease inhibitors. *American Heart Journal*. 2002;144(4):642-8.
70. Lorenz MW, Stephan C, Harmjanz A, Staszewski S, Buehler A, Bickel M, et al. Both long-term HIV infection and highly active antiretroviral therapy are independent risk factors for early carotid atherosclerosis. *Atherosclerosis*. 2008;196(2):720-6.
71. Hsue PY, Deeks SG, Hunt PW. Immunologic Basis of Cardiovascular Disease in HIV-Infected Adults. *J Infect Dis*. 2012;205:S375-S82.
72. Hsue PY, Lo JC, Franklin A, Bolger AF, Martin JN, Deeks SG, et al. Progression of Atherosclerosis as Assessed by Carotid Intima-Media Thickness in Patients With HIV Infection. *Circulation*. 2004;109(13):1603-8.
73. Oliviero U, Bonadies G, Apuzzi V, Foggia M, Bosso G, Nappa S, et al. Human immunodeficiency virus per se exerts atherogenic effects. *Atherosclerosis*. 2009;204(2):586-9.
74. Mercie P, Thiebaut R, Aurillac-Lavignolle V, Pellegrin JL, Yvorra-Vives MC, Cipriano C, et al. Carotid intima-media thickness is slightly increased over time in HIV-1-infected patients. *Hiv Medicine*. 2005;6(6):380-7.
75. McComsey GA, O'Riordan M, Hazen SL, El-Bejjani D, Bhatt S, Brennan ML, et al. Increased carotid intima media thickness and cardiac biomarkers in HIV infected children. *Aids*. 2007;21(8):921-7.
76. Hsue PY, Hunt PW, Schnell A, Kalapus SC, Hoh R, Ganz P, et al. Role of viral replication, antiretroviral therapy, and immunodeficiency in HIV-associated atherosclerosis. *Aids*. 2009;23(9):1059-67.

77. van Vonderen MGA, Smulders YM, Stehouwer CDA, Danner SA, Gundy CM, Vos F, et al. Carotid Intima-Media Thickness and Arterial Stiffness in HIV-Infected Patients: The Role of HIV, Antiretroviral Therapy, and Lipodystrophy. *J Aids*. 2009;50(2):153-61.
78. Bonnet D, Aggoun Y, Szezepanski I, Bellal N, Blanche S. Arterial stiffness and endothelial dysfunction in HIV-infected children. *Aids*. 2004;18(7):1037-41.
79. Sevastianova K, Sutinen J, Westerbacka J, Ristola M, Yki-Jarvinen H. Arterial stiffness in HIV-infected patients receiving highly active antiretroviral therapy. *Antiviral Therapy*. 2005;10(8):925-35.
80. Rios Blanco JJ, Suarez Garcia I, Gomez Cerezo J, Jose Maria Pena Sanchez de R, Moreno Anaya P, Garcia Raya P, et al. Endothelial function in HIV-infected patients with low or mild cardiovascular risk. *Journal of Antimicrobial Chemotherapy*. 2006;58(1):133-9.
81. Kline ER, Sutliff RL. The roles of HIV-1 proteins and antiretroviral drug therapy in HIV-1-associated endothelial dysfunction. *J Invest Med*. 2008;56(5):752-69.
82. Blum A, Hadas V, Burke M, Yust I, Kessler A. Viral load of the human immunodeficiency virus could be an independent risk factor for endothelial dysfunction. *Clin Cardiol*. 2005;28(3):149-53.
83. Rios Blanco JJ, Suarez Garcia I, Gomez Cerezo J, Pena Sanchez de Rivera JM, Moreno Anaya P, Garcia Raya P, et al. Endothelial function in HIV-infected patients with low or mild cardiovascular risk. *Journal of Antimicrobial Chemotherapy*. 2006;58(1):133-9.
84. Paladugu R, Fu WP, Conklin BS, Lin PH, Lumsden AB, Yao QZ, et al. HIV Tat protein causes endothelial dysfunction in porcine coronary arteries. *Journal of Vascular Surgery*. 2003;38(3):549-55.
85. Park I-W, Wang J-F, Groopman JE. HIV-1 Tat promotes monocyte chemoattractant protein-1 secretion followed by transmigration of monocytes. *Blood*. 2001;97(2):352-8.
86. Matzen K, Dirx AEM, oude Egbrink MGA, Speth C, G€utte M, Ascherl G, et al. HIV-1 Tat increases the adhesion of monocytes and T-cells to the endothelium in vitro and in vivo: implications for AIDS-associated vasculopathy. *Virus Research*. 2004;104(2):145-55.
87. Lundgren JD, Neuhaus J, Babiker A, Cooper D, Duprez D, El-Sadr W, et al. Use of nucleoside reverse transcriptase inhibitors and risk of myocardial infarction in HIV-infected patients. *Aids*. 2008;22(14):F17-F24.
88. Worm SW, Sabin C, Weber R, Reiss P, El-Sadr W, Dabis F, et al. Risk of Myocardial Infarction in Patients with HIV Infection Exposed to Specific Individual

Antiretroviral Drugs from the 3 Major Drug Classes: The Data Collection on Adverse Events of Anti-HIV Drugs (D:A:D) Study. *J Infect Dis.* 2010;201(3):318-30.

89. Teixeira HNP, Mesquita ET, Ribeiro ML, Bazin AR, Mesquita CT, Teixeira MP, et al. Study of Vascular Reactivity in HIV Patients whether or not Receiving Protease Inhibitor. *Arquivos Brasileiros De Cardiologia.* 2009;93(4):367-73.

90. Calmy A, Gayet-Ageron A, Montecucco F, Nguyen A, Mach F, Burger F, et al. HIV increases markers of cardiovascular risk: results from a randomized, treatment interruption trial. *Aids.* 2009;23(8):929-39.

91. Shankar SS, Dube MP, Gorski JC, Klaunig JE, Steinberg HO. Indinavir impairs endothelial function in healthy HIV-negative men. *American Heart Journal.* 2005;150(5).

92. Hsue PY, Hunt PW, Wu Y, Schnell A, Ho JE, Hatano H, et al. Association of abacavir and impaired endothelial function in treated and suppressed HIV-infected patients. *Aids.* 2009;23(15):2021-7.

93. Grubb JR, Dejam A, Voell J, Blackwelder WC, Sklar PA, Kovacs JA, et al. Lopinavir-ritonavir: Effects on endothelial cell function in healthy subjects. *J Infect Dis.* 2006;193(11):1516-9.

94. Brinkman K, ter Hofstede HJM, Burger DM, Smeitink JAM, Koopmans PP. Adverse effects of reverse transcriptase inhibitors: mitochondrial toxicity as common pathway. *Aids.* 1998;12(14):1735-44.

95. Hebert V, Crenshaw B, Romanoff R, Ekshyyan V, Dugas T. Effects of HIV drug combinations on endothelin-1 and vascular cell proliferation. *Cardiovascular Toxicology.* 2004;4(2):117-31.

96. Sutliff RL, Dikalov S, Weiss D, Parker J, Raidel S, Racine AK, et al. Nucleoside reverse transcriptase inhibitors impair endothelium-dependent relaxation by increasing superoxide. *Am J Physiol-Heart Circul Physiol.* 2002;283(6):H2363-H70.

97. Mondal D, Pradhan L, Ali M, Agrawal K. HAART drugs induce oxidative stress in human endothelial cells and increase endothelial recruitment of mononuclear cells. *Cardiovascular Toxicology.* 2004;4(3):287-302.

98. Chen C, Lu X-H, Yan S, Chai H, Yao Q. HIV protease inhibitor ritonavir increases endothelial monolayer permeability. *Biochem Biophys Res Commun.* 2005;335(3):874-82.

99. Dressman J, Kincer J, Matveev SV, Guo L, Greenberg RN, Guerin T, et al. HIV protease inhibitors promote atherosclerotic lesion formation independent of dyslipidemia by increasing CD36-dependent cholesteryl ester accumulation in macrophages. *Journal of Clinical Investigation.* 2003;111(3):389-97.

100. Jamaluddin MS, Lin PH, Yao Q, Chen C. Non-nucleoside reverse transcriptase inhibitor efavirenz increases monolayer permeability of human coronary artery endothelial cells. *Atherosclerosis*.208(1):104-11.
101. Kamiya A, Togawa T. ADAPTIVE REGULATION OF WALL SHEAR-STRESS TO FLOW CHANGE IN THE CANINE CAROTID-ARTERY. *Am J Physiol*. 1980;239(1):H14-H21.
102. Clark JM, Glagov S. STRUCTURAL INTEGRATION OF THE ARTERIAL-WALL .1. RELATIONSHIPS AND ATTACHMENTS OF MEDIAL SMOOTH-MUSCLE CELLS IN NORMALLY DISTENDED AND HYPER-DISTENDED AORTAS. *Lab Invest*. 1979;40(5):587-602.
103. Jackson ZS, Gotlieb AI, Langille BL. Wall tissue remodeling regulates longitudinal tension in arteries. *CircRes*. 2002;90(8):918-25.
104. Matsumoto T, Hayashi K. Stress and strain distribution in hypertensive and normotensive rat aorta considering residual strain. *J Biomech Eng-Trans ASME*. 1996;118(1):62-73.
105. Roach MR, Burton AC. THE REASON FOR THE SHAPE OF THE DISTENSIBILITY CURVES OF ARTERIES. *Canadian Journal of Biochemistry and Physiology*. 1957;35(8):681-90.
106. Humphrey JD. An introduction to biomechanics : solids and fluids, analysis and design. Delange SL, editor. New York :: Springer; 2004.
107. Vonmaltzahn WW, Warriyar RG, Keitzer WF. EXPERIMENTAL MEASUREMENTS OF ELASTIC PROPERTIES OF MEDIA AND ADVENTITIA OF BOVINE CAROTID ARTERIES. *Journal of Biomechanics*. 1984;17(11):839-47.
108. Holzapfel GA, Weizsacker HW. Biomechanical behavior of the arterial wall and its numerical characterization. *Computers in Biology and Medicine*. 1998;28(4):377-92.
109. Wuyts FL, Vanhuyse VJ, Langewouters GJ, Decraemer WF, Raman ER, Buyle S. ELASTIC PROPERTIES OF HUMAN AORTAS IN RELATION TO AGE AND ATHEROSCLEROSIS - A STRUCTURAL MODEL. *Physics in Medicine and Biology*. 1995;40(10):1577-97.
110. Tozeren A. ELASTIC PROPERTIES OF ARTERIES AND THEIR INFLUENCE ON THE CARDIOVASCULAR-SYSTEM. *J Biomech Eng-Trans ASME*. 1984;106(2):182-5.
111. Baek S, Gleason RL, Rajagopal KR, Humphrey JD. Theory of small on large: Potential utility in computations of fluid-solid interactions in arteries. *Computer Methods in Applied Mechanics and Engineering*. 2007;196(31-32):3070-8.

112. Vonmaltzahn WW, Besdo D, Wiemer W. ELASTIC PROPERTIES OF ARTERIES - A NON-LINEAR 2-LAYER CYLINDRICAL MODEL. *Journal of Biomechanics*. 1981;14(6):389-97.
113. Demiray H, Vito RP. A LAYERED CYLINDRICAL-SHELL MODEL FOR AN AORTA. *International Journal of Engineering Science*. 1991;29(1):47-54.
114. Rachev A, Hayashi K. Theoretical Study of the Effects of Vascular Smooth Muscle Contraction on Strain and Stress Distributions in Arteries. *Annals of Biomedical Engineering*. 1999;27(4):459-68.
115. Zulliger MA, Rachev A, Stergiopoulos N. A constitutive formulation of arterial mechanics including vascular smooth muscle tone. *Am J Physiol Heart Circ Physiol*. 2004;287(3):H1335-43.
116. Brankov G, Rachev AI, Stoychev S, editors. A composite model of large blood vessels. *Mechanics of Biological Solid: Proceedings of the Euromech Colloquium; 1975; Varna, Bulgaria: Publishing House of the Bulgarian Academy of Sciences*.
117. Lanir Y. Constitutive equations for fibrous connective tissues. *J Biomech*. 1983;16:1-12.
118. Holzapfel GA, Gasser TC, Ogden RW. A new constitutive framework for arterial wall mechanics and a comparative study of material models. *J Elast*. 2000; 61:1-48.
119. Zulliger MA, Fridez P, Hayashi K, Stergiopoulos N. A strain energy function for arteries accounting for wall composition and structure. *J Biomech*. 2004;37:989-1000.
120. Gleason RL, Wilson E, Humphrey JD. Biaxial biomechanical adaptations of mouse carotid arteries cultured at altered axial extension. *J Biomech*. 2007;40:766-76.
121. Gleason RL, Taber LA, Humphrey JD. A 2-D model of flow-induced alterations in the geometry, structure, and properties of carotid arteries. *J Biomech Eng*. 2004;126:371-81.
122. Chuong CJ, Fung YC. On residual stress in arteries. *J Biomech Eng*. 1986;108:189-92.
123. Baek S, Gleason RL, Rajagopal KR, Humphrey JD. Theory of small on large in computations of fluid-solid interactions in arteries. *Comput Methods Applied Mech Eng*. 2007;196:3070-8.
124. Gleason RL, Wilson E, Humphrey JD. Biaxial biomechanical adaptations of mouse carotid arteries cultured at altered axial extension. *J Biomech*. 2007;40(4):766-76.
125. Humphrey JD. *Cardiovascular Solid Mechanics: Cells, Tissues, Organs*. New York: Springer-Verlag; 2002.

126. Spencer AJM. Constitutive theory for strongly anisotropic solids. In: Spencer AJM, editor. *Continuum Theory of the Mechanics of Fibre-Reinforced Composites*, CISM Courses and Lectures No 282, International Centre for Mechanical Sciences. Wien: Springer-Verlag; 1984. p. 1-32.
127. Roach M, Burton A. The reason for the shape of the distensibility curves of arteries. *Can J Biochem Physiol* 1957;35:681-90.
128. Azeloglu EU, Albro MB, Thimmappa VA, Ateshian GA, Costa KD. Heterogeneous transmural proteoglycan distribution provides a mechanism for regulating residual stresses in the aorta. *Am J Physiol: Heart Circ Physiol*. 2008;(in press, available on-line).
129. Martinez-Lemus LA, Hill MA, Bolz SS, Pohl U, Meininger GA. Acute mechanoadaptation of vascular smooth muscle cells in response to continuous arteriolar vasoconstriction: implications for functional remodeling. *Faseb Journal*. 2004;18(2):708-+.
130. Gleason RL, Humphrey JD. A 2-D constrained mixture model for arterial adaptations to large changes in flow, pressure, and axial stretch. *Math Med Biol*. 2005;22(4):347-69.
131. Gleason RL, Dye WW, Wilson E, Humphrey JD. Quantification of the mechanical behavior of carotid arteries from wild-type, dystrophin-deficient, and sarcoglycan-delta knockout mice. *J Biomech*. 2008;41(15):3213-8.
132. Gleason RL, Wan W. Theory and experiments for mechanically-induced remodeling of tissue engineered blood vessels. *Proceedings of the CIMTEC 2008 - 3rd International Conference "Smart Materials, Structures and Systems" 2008*:In press.
133. Wicker B, Hutchens H, Wu Q, Yeh A, Humphrey J. Normal basilar artery structure and biaxial mechanical behavior. *Computer Methods in Biomechanics and Biomedical Engineering*. 2008;11(5):539-51.
134. Zeinali-Davarani S, Choi J, Baek S. On parameter estimation for biaxial mechanical behavior of arteries. *J Biomech*. 2009;42(4):524-30.
135. Humphrey JD, Rajagopal KR. A constrained mixture model for growth and remodeling of soft tissues. *Math Models Meth Appl Sci*. 2002;12(3):407-30.
136. Gleason RL, Taber LA, Humphrey JD. A 2-D model of flow-induced alterations in the geometry, structure, and properties of carotid arteries. *J Biomech Eng*. 2004;126(3):371-81.

137. van Wijk JP, de Koning EJ, Cabezas MC, Joven J, op't Roodt J, Rabelink TJ, et al. Functional and structural markers of atherosclerosis in human immunodeficiency virus-infected patients. *J Am Coll Cardiol.* 2006;47(6):1117-23.
138. Stein JH, Klein MA, Bellehumeur JL, McBride PE, Wiebe DA, Otvos JD, et al. Use of human immunodeficiency virus-1 protease inhibitors is associated with atherogenic lipoprotein changes and endothelial dysfunction. *Circulation.* 2001;104(3):257-62.
139. Shankar SS, Dube MP, Gorski JC, Klaunig JE, Steinberg HO. Indinavir impairs endothelial function in healthy HIV-negative men. *Am Heart J.* 2005;150(5):933.
140. Friis-Moller N, Weber R, Reiss P, Thiebaut R, Kirk O, d'Arminio Monforte A, et al. Cardiovascular disease risk factors in HIV patients--association with antiretroviral therapy. Results from the DAD study. *AIDS.* 2003;17(8):1179-93.
141. Grubb J, Dejam A, Voell J, Blackwelder W, Sklar P, Kovacs J, et al. Lopinavir-ritonavir: effects on endothelial cell function in healthy subjects. *J Infect Dis.* 2006;193(11):1516-9.
142. Choi AI, Vittinghoff E, Deeks SG, Weekley CC, Li Y, Shlipak MG. Cardiovascular risks associated with abacavir and tenofovir exposure in HIV-infected persons. *AIDS.* 2011;25(10):1289-98.
143. Worm SW, Sabin C, Weber R, Reiss P, El-Sadr W, Dabis F, et al. Risk of myocardial infarction in patients with HIV infection exposed to specific individual antiretroviral drugs from the 3 major drug classes: the data collection on adverse events of anti-HIV drugs (D:A:D) study. *The Journal of infectious diseases.* 2010;201(3):318-30.
144. Lundgren J, Neuhaus J, Babiker A, Cooper D, Duprez D, El-Sadr W, et al. Use of nucleoside reverse transcriptase inhibitors and risk of myocardial infarction in HIV-infected patients. *AIDS.* 2008;22(14):F17-24.
145. El-Sadr WM, Lundgren JD, Neaton JD, Gordin F, Abrams D, Arduino RC, et al. CD4+ count-guided interruption of antiretroviral treatment. *N Engl J Med.* 2006;355(22):2283-96.
146. Kopp JB, Klotman ME, Adler SH, Bruggeman LA, Dickie P, Marinos NJ, et al. PROGRESSIVE GLOMERULOSCLEROSIS AND ENHANCED RENAL ACCUMULATION OF BASEMENT-MEMBRANE COMPONENTS IN MICE TRANSGENIC FOR HUMAN-IMMUNODEFICIENCY-VIRUS TYPE-1 GENES. *Proc Natl Acad Sci U S A.* 1992;89(5):1577-81.
147. Sukhova GK SG, Simon DI, Chapman HA, Libby P. Expression of the elastolytic cathepsins S and K in human atheroma and regulation of their production in smooth muscle cells. *The Journal of Clinical Investigation.* 1998;102:576-83.

148. Lutgens E, Lutgens SP, Faber BC, Heeneman S, Gijbels MM, de Winther MP, et al. Disruption of the cathepsin K gene reduces atherosclerosis progression and induces plaque fibrosis but accelerates macrophage foam cell formation. *Circulation*. 2006;113(1):98-107.
149. Sukhova GK, Zhang Y, Pan JH, Wada Y, Yamamoto T, Naito M, et al. Deficiency of cathepsin S reduces atherosclerosis in LDL receptor-deficient mice. *J Clin Invest*. 2003;111(6):897-906.
150. Wan W, Yanagisawa H, Gleason R. Biomechanical and Microstructural Properties of Common Carotid Arteries from Fibulin-5 Null Mice. *Annals of Biomedical Engineering*. 2010;38(12):3605-17.
151. Chuong C, Fung Y. On residual stress in arteries. *J Biomech Eng*. 1986;108:189-92.
152. Wagenseil JE, Nerurkar NL, Knutsen RH, Okamoto RJ, Li DY, Mecham RP. Effects of elastin haploinsufficiency on the mechanical behavior of mouse arteries. *Am J Physiol Heart Circ Physiol*. 2005;289(3):H1209-17.
153. Zoumi A, Lu XA, Kassab GS, Tromberg BJ. Imaging coronary artery microstructure using second-harmonic and two-photon fluorescence microscopy. *Biophys J*. 2004;87(4):2778-86.
154. Ng CP, Hinz B, Swartz MA. Interstitial fluid flow induces myofibroblast differentiation and collagen alignment in vitro. *J Cell Sci*. 2005;118(20):4731-9.
155. Timmins LH, Wu QF, Yeh AT, Moore JE, Greenwald SE. Structural inhomogeneity and fiber orientation in the inner arterial media. *Am J Physiol-Heart Circ Physiol*. 2010;298(5):H1537-H45.
156. Wan W, Dixon JB, Gleason Rudolph L. Constitutive Modeling of Mouse Carotid Arteries Using Experimentally Measured Microstructural Parameters. *Biophys J*. 2012;102(12):2916-25.
157. Li WA, Barry ZT, Cohen JD, Wilder CL, Deeds RJ, Keegan PM, et al. Detection of femtomole quantities of mature cathepsin K with zymography. *Analytical Biochemistry*. 2010;401(1):91-8.
158. Wilder CL, Platt MO. Manipulating substrate and pH in zymography protocols selectively identifies cathepsins K, L, S, and V activity in cells and tissues. In Review. 2011.
159. Kaplan RC, Sinclair E, Landay AL, Lurain N, Sharrett AR, Gange SJ, et al. T cell activation predicts carotid artery stiffness among HIV-infected women. *Atherosclerosis*. 2011.

160. Seaberg EC, Benning L, Sharrett AR, Lazar JM, Hodis HN, Mack WJ, et al. Association between human immunodeficiency virus infection and stiffness of the common carotid artery. *Stroke*. 2010;41(10):2163-70.
161. Sevastianova K, Sutinen J, Westerbacka J, Ristola M, Yki-Jarvinen H. Arterial stiffness in HIV-infected patients receiving highly active antiretroviral therapy. *Antivir Ther*. 2005;10(8):925-35.
162. Lorenz M, Stephan C, Harmjanz A, Staszewski S, Buehler A, Bickel M, et al. Both long-term HIV infection and highly active antiretroviral therapy are independent risk factors for early carotid atherosclerosis. *Atherosclerosis*. 2008;196(2):720-6.
163. Lorenz MW, Stephan C, Harmjanz A, Staszewski S, Buehler A, Bickel M, et al. Both long-term HIV infection and highly active antiretroviral therapy are independent risk factors for early carotid atherosclerosis. *Atherosclerosis*. 2007.
164. Arnet D, Evans G, Riley W. Arterial stiffness: a new cardiovascular risk factor? *Am J Epidemiol*. 1994;140:669-82.
165. KÃ¼r A, Glasz T. Development of atherosclerosis and plaque biology. *Cardiovascular Surgery*. 2001;9(2):109-21.
166. Fernandez-Moure JS, Vykoukal D, Davies MG. Biology of aortic aneurysms and dissections. *Methodist DeBakey cardiovascular journal*. 2011;7(3):2-7.
167. Lee H-Y, Oh B-H. Aging and arterial stiffness. *Circulation journal : official journal of the Japanese Circulation Society*. 2010;74(11):2257-62.
168. Platt MO, Ankeny RF, Shi GP, Weiss D, Vega JD, Taylor WR, et al. Expression of cathepsin K is regulated by shear stress in cultured endothelial cells and is increased in endothelium in human atherosclerosis. *Am J Physiol-Heart Circul Physiol*. 2007;292(3):H1479-H86.
169. Holmberg SD, Moorman AC, Williamson JM, Tong TC, Ward DJ, Wood KC, et al. Protease inhibitors and cardiovascular outcomes in patients with HIV-1. *Lancet*. 2002;360(9347):1747-8.
170. Spieker LE, Karadag B, Binggeli C, Corti R. Rapid progression of atherosclerotic coronary artery disease in patients with human immunodeficiency virus infection. *Heart and Vessels*. 2005;20(4):171-4.
171. Ross AC, Storer N, O'Riordan M, Dogra V, El-Bejjani D, Bhatt S, et al. Carotid intima-media thickness (cIMT) improves over time in HIV-infected children. *Antiviral Therapy*. 2008;13(8):A18-A9.
172. El-Sadr WM, Lundgren JD, Neaton JD, Gordin F, Abrams D, Arduino RC, et al. CD4+count-guided interruption of antiretroviral treatment. *New England Journal of Medicine*. 2006;355(22):2283-96.

173. Wang XW, Chai H, Yao QZ, Chen CY. Molecular mechanisms of HIV protease inhibitor-induced endothelial dysfunction. *J AIDS*. 2007;44(5):493-9.
174. Fisher SD, Miller TL, Lipshultz SE. Impact of HIV and highly active antiretroviral therapy on leukocyte adhesion molecules, arterial inflammation, dyslipidemia, and atherosclerosis. *Atherosclerosis*. 2006;185(1):1-11.
175. Charakida M, Loukogeorgakis SP, Okorie MI, Masi S, Halcox JP, Deanfield JE, et al. Increased arterial stiffness in HIV-infected children: risk factors and antiretroviral therapy. *Antiviral Therapy*. 2009;14(8):1075-9.
176. Gleason RL, Wilson E, Humphrey JD. Biaxial biomechanical adaptations of mouse carotid arteries cultured at altered axial extension. *Journal of Biomechanics*. 2007;40(4):766-76.
177. Humphrey JD, Eberth JF, Dye WW, Gleason RL. Fundamental role of axial stress in compensatory adaptations by arteries. *Journal of Biomechanics*. 2009;42(1):1-8.
178. Bruggeman LA, Dikman S, Meng C, Quaggin SE, Coffman TM, Klotman PE. Nephropathy in human immunodeficiency virus-1 transgenic mice is due to renal transgene expression. *Journal of Clinical Investigation*. 1997;100(1):84-92.
179. Lafrenie RM, Wahl LM, Epstein JS, Hewlett IK, Yamada KM, Dhawan S. HIV-1-Tat protein promotes chemotaxis and invasive behavior by monocytes. *Journal of Immunology*. 1996;157(3):974-7.
180. Tan XL, Boudinot FD. Simultaneous determination of zidovudine and its monophosphate in mouse plasma and peripheral red blood cells by high-performance liquid chromatography. *Journal of Chromatography B*. 2000;740(2):281-7.
181. Lewis W, Grupp IL, Grupp G, Hoit B, Morris R, Samarel AM, et al. Cardiac dysfunction occurs in the HIV-1 transgenic mouse treated with zidovudine. *Lab Invest*. 2000;80(2):187-97.
182. Zhang SH, Reddick RL, Piedrahita JA, Maeda N. SPONTANEOUS HYPERCHOLESTEROLEMIA AND ARTERIAL LESIONS IN MICE LACKING APOLIPOPROTEIN-E. *Science*. 1992;258(5081):468-71.